

Estimating Navigable Areas in Scarce Data River Environments

A Chindwin case study

F.S. Laurens

Technische Universiteit Delft

Estimating Navigable Areas in Scarce Data River Environments

A Chindwin case study

by

F.S. Laurens

to obtain the degree of Master of Science
at the Delft University of Technology,

Student number:	4237315	
Project duration:	February 4, 2019 – May 13, 2020	
Thesis committee:	Prof. dr. ir. M. van Koningsveld,	TU Delft, chair
	Dr. ir. C. Sloff,	TU Delft
	Ir. A.J. Lansen,	TU Delft
	Dr. ir. M. Yossef,	Deltares
	Ir. BJ van der Spek	CDR International

An electronic version of this thesis is available at <http://repository.tudelft.nl/>.

Preface

This research was conducted as the final stage of the master Civil Engineering at the faculty of Civil Engineering and Geosciences of the Delft University of Technology. I was engaged in this research from February 2019 to May 2020.

Performing this research has known its difficulties. The support from my graduation committee in those periods was very meaningful. Many routes were explored before a definitive one was chosen. The knowledge acquired from those routes however, undoubtedly added to the value of the final result.

I would like to thank CDR International for granting me the opportunity to work in their company as their first ever TU Delft graduation student. The time I had in Amersfoort was great. A special thanks to the colleagues there for their assistance and making me feel welcome like you did. I will especially remember all the spontaneous drinks we had at the rooftop bar! Moreover I wish to thank Deltares for providing me with expert support and offering me a place in their office as well.

My daily supervisor, Bart-Jan van der Spek, I wish to thank for his valuable support in the development of this thesis and for showing his support in my approach throughout. I would like to thank Kees Sloff for adding to this research by shedding a light on the mysterious world of river morphology as well as by sharing his ever captivating stories and knowledge of Myanmar. To Mark van Koningsveld I wish to extend my gratitude for really taking his time to understand my work and all the improvements that has led to. To Mohamed Yossef I say thanks for helping me find back the right track to a thesis subject last summer as well as for his sharp suggestions for research and model improvements. Finally I wish to extend my gratitude to Joost Lanssen for his willingness to join the committee at a late notice and for assisting with the overall structure of the report. Enjoy reading!

*Florian Laurens
Rotterdam, May 2020*

Abstract

The seasonal Chindwin river in the poor north-western part of Myanmar forms the central artery for business and transport in the region. Unfortunately, a combination of low water levels during the dry period, the dynamic morphology, archaic boat equipment and limited monitoring, yearly results in large numbers of grounding ships. Every year this causes many injuries and deaths as well as economic losses. A pilot project was initiated in the beginning of 2019 to benefit safer navigation on the Chindwin. The pilot project involves equipping a limited number of commercial ships sailing on the Chindwin with CoVadem technology. Supported by state of the art Big Data technology, CoVadem charts the most up to date water depths by collecting under keel clearance measurements from the commercial fleet. The pilot project aims to increase safety on the Chindwin through sharing information about safe routes and forecasted water depths with captains sailing the river.

The added value of using CoVadem technology, however, is vulnerable to the number of participating vessels. A combination of morphological changes and the typical spatial spread (with limited cross-sectional coverage) of CoVadem data limits the extent of the navigation channel that can be derived from the data. With only a small part of the navigation channel known, the full potential of CoVadem technology for navigational safety and efficiency is not reached: it is unclear where passing of other vessels is possible, where speeds should be adjusted due to e.g., bottlenecks and where shorter routes are present.

The objective of this research is to provide more information about the navigable area around CoVadem ship track data in order to assist captains with navigation. During this research, two physics-based models have been developed that are independently able to carry out this task. The first model, named the *soil-model*, combines CoVadem data with the maximum slope that can be expected in the river bed (given known properties of the bed material). The second model, the *axi-symmetric model*, calculates the bed slope around CoVadem data to determine navigable areas. The bed slope is calculated with the axi-symmetric solution, a known analytical solution to estimate the cross-section scale bathymetry for meandering rivers. In addition to this, assumptions about the presence (and location) of river banks and sand dunes are included in the *axi-symmetric model*.

The *axi-symmetric model* is not suitable for every part of the Chindwin. Two *reliability indicators* have been developed to indicate where the *axi-symmetric model* can be safely used (and where not). The first reliability indicator is named the channel *stability score*, a measure for how stable the low discharge channel alignment is. The score is calculated based on multiple years of satellite imagery, acquired during months with low discharge. Water masks are detected and combined with those of other years. The *stability score* is calculated from the variability in the water masks. It was hypothesised that the *axi-symmetric model* is more reliable for parts of the river with a more stable channel alignment. The second reliability indicator is the *curvature ratio* of the river: it was hypothesised that the *axi-symmetric model* is more reliable for curved parts of the river.

The performance of the physics-based models and the hypotheses about the reliability indicators have been tested and evaluated for four study cases located along the Chindwin river. The models estimate a navigable area. To judge the quality of a navigable area estimate, two dimensionless performance indicators have been developed: the *safety score* and the *channel coverage score*. The first performance indicator is related to the reliability of a navigable area estimate, the latter to the width of the estimate.

The results are promising. It follows from this research that navigation channel estimates around scarce CoVadem ship track data can substantially benefit from application of a physics-based model. The *soil-model* is very reliable, but boasts only a small improvement in the width of the navigable area estimate. The *axi-symmetric model* increases the navigable width estimate from a single CoVadem trackline significantly $O(100\text{ m})$. However, the model is not 100% reliable: around 2% of the estimated navigable area was wrong. The reliability of the *axi-symmetric model* can be substantially improved when it is only applied to areas where the *reliability indicators* (channel stability score and/or channel curvature) mark the *axi-symmetric model* as reliable. Hence both the hypotheses about the reliability indicators are supported by the results.

This research combines Big Data, physics-based models and remote sensing in a not early demonstrated way: with models tailored for navigable area estimates and with measured data as the starting point. The correlation between axi-symmetric model reliability and remote sensing/curvature is, moreover, something that has not been demonstrated before. Finally, the two developed performance indicators show great promise for the evaluation of navigable area estimates. As such, this research adds to current advancements in (open-access) cross-platform data accumulation and utilisation.

Table of Contents

Abstract	v
1 Introduction	1
1.1 Problem Statement	2
1.2 Research question	2
1.3 Thesis outline	3
2 Background research	5
2.1 Challenges for navigable area estimates when using CoVadem ship track data	5
2.1.1 Initial UKC data processing	6
2.1.2 Hydrodynamics	6
2.1.3 Morphodynamics	7
2.1.4 Spatial data scarcity	7
2.1.5 Discussion of uncertainties	8
2.2 Morphology information from physics-based models.	9
2.2.1 River bed characteristics	9
2.2.2 Axi-symmetric solution	10
2.2.3 Computational Fluid Dynamics (CFD) model	13
2.3 Morphology information from remote sensing	13
2.3.1 Surface water detection methods	14
2.3.2 The 'water-line' method	14
2.3.3 Inverse-depth estimated from multispectral optical satellite imagery	15
2.4 Selection of models and methods	15
3 Methodology	17
3.1 Overview of the proposed models and reliability indicators.	17
3.2 Study case selection.	19
3.3 River discretisation	19
3.4 Processing data	19
3.4.1 Available data	19
3.4.2 Ground Truth bathymetry	19
3.4.3 CoVadem datasets	20
3.5 Reliability indicators	21
3.5.1 Data selection, retrieval and cleaning	21
3.5.2 Water detection	21
3.5.3 Water occurrence	22
3.5.4 Channel stability score.	22
3.5.5 Curvature ratio.	24
3.6 The soil-model	26
3.7 The axi-symmetric model.	28
3.7.1 Axi-symmetric solution	28
3.7.2 Inclusion of river banks	31
3.7.3 Inclusion of sand dunes	32
3.8 Validation approach	32
3.8.1 Model validation method	32
3.8.2 Validation datasets.	33
3.8.3 Axi-symmetric model reliability indicators.	35
4 Results and evaluation	39
4.1 Study cases	39
4.1.1 Study case - Htamanthi	40

4.1.2	Study case - Kalewa	42
4.1.3	Study case - Monywa.	45
4.2	Results: curvature, channel stability and model performance.	45
4.2.1	Qualitative analysis	45
4.2.2	Quantitative analysis.	47
4.3	Summary of the results	50
4.4	Utilisation example	50
5	Discussion	53
5.1	Related studies	53
5.2	Study limitations	54
6	Conclusions & Recommendations	55
6.1	Conclusions.	55
6.2	Recommendations	57
6.2.1	Recommendations for model use	57
6.2.2	Recommendations for model improvement/implementation	58
6.2.3	Recommendations for future work.	59
	Bibliography	61
A	Appendix Background Research	65
A.1	Remote sensing	65
A.2	Classification of bed forms	67
B	Appendix Methodology	71
B.1	River discretisation	71
B.2	Data formatting, cleaning and georeferencing	72
B.3	Data interpolation	73
B.4	Water occurrence time-window.	73
B.5	Calibrating the axi-symmetric model	76
C	Appendix Results	79
C.1	Results Khamtee	79
C.2	Performance indicators all study cases	81
C.3	Simultaneous application of two reliability thresholds	82
C.4	Sensitivity analysis	83

Nomenclature

α	internal angle of friction [°]
Δ	relative density of sediment [-]
κ	von Karman constant [-]
ν	kinematic viscosity [m^2/s]
\bar{u}	mean flow velocity [m/s]
ρ_s	density of sand [kg^3/m]
ρ_w	density of water [kg^3/m]
θ	Shields parameter [-]
ζ	water level [$m + datum$]
A	coefficient related to the influence of helical flow [-]
a	calibration coefficient related to the influence of helical flow [-]
B	width of river cross-section [m]
C	Chézy roughness coefficient [$m^{1/2}/s$]
d_{50}	median bed particle (50% passing by weight) [m]
D_{extra}	water depth available on top of D_{nav} [m]
D_{nav}	water depth required for navigation [m]
g	gravitational acceleration [m/s^2]
h_0	equilibrium water depth [m]
h_{dune}	dune height [m]
i_s	longitudinal river slope [m/m]
l_{dune}	dune length [m]
m, n	grid nodes [-]
Q	total discharge [m^3/s]
R_c	radius of curvature [m]
u, v	flow velocity in streamwise and transverse direction [m/s]
u'_*	$\bar{u}\sqrt{g}/C$, grain shear velocity [m/s]
u_{*c}	critical grain shear velocity [m/s]
W_{nav}	width determined as safe for navigation [m]
z	bed level [$m + datum$]
z_{bank}	river bank level [$m + datum$]

List of Abbreviations

AWEI Automated Water Extraction Index. 14

CFD Computational Fluid Dynamics. 13, 16, 59

CRS Coordinate Reference System. 72

D-RATIN Deltares-Rapid Assessment Tool for Inland Navigation. 10, 12, 18, 19, 53, 71

DWIR Directorate of Water Resources and Improvement of River Systems. 7, 19

EO Electro-optical (remote sensing). 14, 65

EPSG European Petroleum Survey Group. 72

MAE Mean Absolute Error. 12

MNDWI Modified Normalised Difference Water Index. 14, 21, 22

NDWI Normalised Difference Water Index. 14

NIR Near Infrared. 14

QUICKIN Tool for generation and manipulation of grid-related parameters such as bathymetry, initial conditions and roughness. 73

SAR Synthetic-aperture radar (remote sensing). 65, 67

SRTM Shuttle Radar Topography Mission. 39

SWIR Shortwave Infrared. 14

UKC Under Keel Clearance. 5, 6, 55

Introduction

Inland waterway transport is one of the most important transport modes in Myanmar, responsible for a third of total transport volume [Nam and Win, 2014]. For the poor Chindwin region, where road infrastructure is generally bad, these numbers are even higher. Hundreds of thousands of people depend for their livelihoods and culture on the unique and biodiverse river ecosystem [KWHRO, 2011].

In December 2018 a pilot project led by CDR International together with Deltares and CoVadem was initiated. The project proposes to use a Navigation with Nature approach to counter navigability issues with help of the application of CoVadem technology [Project description, 2019]. The technology comprises equipping cargo and passenger transport ships with echo sounders that constantly collect water depth measurements and share this data with the cloud.

Figure 1.1 shows the Chindwin river, originating in the Hugawng valley in Kachin State, Myanmar. Its course leads through a diverse landscape of initially mountain ranges and further down its stream more gentle landscapes. The river ends in the confluence with the huge Ayeyarwady river [van der Velden, 2015].



Figure 1.1: Overview of the main rivers in Myanmar. The Chindwin river, the largest tributary to the Ayeyarwady and main subject of this thesis is highlighted (from Google Earth, modified)

The highly seasonal river experiences huge yearly discharge fluctuations: during the wet season the Chindwin can discharge over $15.000 \text{ m}^3/\text{s}$ [van der Velden, 2015]. After the monsoon period, discharges gradually decline and near the end of the dry period discharges are on average around $1000 \text{ m}^3/\text{s}$ [DWIR, 2014].

The high monsoon discharges cause massive sediment transport and consecutively the river shows significant morphodynamic activity [Ligthart, 2017, van der Velden, 2015]. Over the monsoon period the location

of a navigation channel can shift in its entirety. More than 96% of annual sediment transport takes place from June through October [DWIR, 2014].

For the duration of the dry season, from December until May, water levels are low resulting in significantly hampered navigation due to limited depth [DWIR, 2014]. During this period ships can often only sail with a limited amount of cargo and sometimes not at all at certain bottlenecks in the system [ADB, 2016].

1.1. Problem Statement

Ideally, navigation can be adjusted to accurately forecasted and spatially fully covered water depths. Loading and routing of the ships is perfectly optimised. Based on the forecasted available draft for navigation, ship loading can be maximised. A clearly and reliably marked navigation channel moreover offers captains the opportunity for optimal routing as well as the possibility to e.g. adjust their speed near bottlenecks and safe passing with opposing ships.

For the Chindwin river the opposite holds: hardly any information about the navigation channel is available. Mainly due to the fact that the river changes rapidly [Attema and Hendriks, 2014, Ligthart, 2017, van der Velden, 2015] and also due to relatively old boat equipment (measuring poles, no echosounders) [Vellinga, 2019]. As a result, captains sailing the Chindwin often have to limit their speed during the dry season. This is a necessary precaution in order for them to carefully find their way through the many shallow parts of the river. If captains fail to do so, ships can ground causing injuries and deaths [DWIR, 2014] as well as economic damage [ADB, 2016]. During droughts ships also have to limit the amount of cargo they carry to decrease their draft and make it past river bottlenecks [ADB, 2016, Aung, 2019]. This leads to economic damage due to unnecessary amounts of vessel lightering (when the forecasted depth is unknown) and unsafe/slower navigation when the navigation channel is unknown (from expert consultation with Dr. ir. C. Sloff).

The Navigation with Nature pilot project aims to counter the above mentioned challenges by providing better water depth estimates and forecasts [Project description, 2019]. The pilot project utilises CoVadem technology (www.covadem.org) in combination with hydrodynamic modelling to provide guidance for safer navigation. The envisioned benefits of the pilot project to navigation are twofold:

1. Sailing can become safer by providing additional information about navigable areas.
2. Ship loading can be optimised based on the forecasted minimum water depth (along some trajectory)

This research aims to help improve on the first point. However, a rather large amount of CoVadem ship tracks is necessary to have an 'acceptable' estimate of the bathymetry for navigation: Peters et al. [2015] suggested a (subjective) minimum of 33. For the pilot project such numbers can not be expected. The stretch of the Chindwin that is investigated is over 400 km long and around a kilometre wide [Project description, 2019]. The total number of participating, with CoVadem technology equipped ships is limited to at maximum 10 for now [Vellinga, 2019]. Additionally the river has a dynamic morphology limiting the time window from which data can be used [Ligthart, 2017, van Duijn, 2018]. The spatial spread of CoVadem data is moreover not ideal: data is acquired below ship tracks that generally sail up and down the river, leaving most of the river width unmeasured [Peters et al., 2015]. The huge extent of the pilot project area, the dynamic morphology, the limited amount of participating ships and the non-homogeneous spread of the data result in only a small and scattered part of the navigable area of the river that is known from the data.

It is hypothesised that the same data, if combined with additional knowledge of the morphology, can provide more information about the navigable area around it. With more information about navigable areas, navigational safety on the Chindwin increases, aiding the hundreds of thousands depending on the river for their livelihoods.

1.2. Research question

Considering the problem statement, the main research question is formulated as follows:

"How can additional knowledge of river morphology improve the navigable area estimate around CoVadem ship track data in scarce data environments?"

Sub questions

1. *"What are the challenges for navigable area estimates when using CoVadem ship track data?"*
2. Information about navigable areas can potentially come from other sources than just CoVadem data. Physics-based modelling and remote sensing have been investigated as possibilities. The following two research questions were formulated:
 - 2.a) *"How can a physics-based model provide more information about navigable areas?"*
 - 2.b) *"How can remote sensing provide more information about navigable areas?"*
3. It is the aim of this research to develop some method that can estimate a navigable area around CoVadem ship track data. In order to know how good the developed method works, its performance should be measured, leading up to the following two research questions:
 - 3.a) *"How can the performance of a navigable area estimate be measured objectively?"*
 - 3.b) *"What is the performance of the developed method in terms of answering the main research question?"*

1.3. Thesis outline

A brief summary of all remaining chapters and their content:

Chapter 2 commences with answering sub research question 1, the identification of challenges for navigable area estimates from CoVadem ship track data (§2.1). Consecutively a number of alternatives that can provide knowledge about the morphology are discussed and a selection is made. Based on the selection, a method is proposed that uses additional knowledge of the morphology to improve the navigable area estimate around CoVadem ship track data.

Chapter 3 discusses the *proposed method* more in depth. The approach for practical application of the *proposed method* on four study cases is elaborated on (§3.2 to §3.7). Moreover the validation approach to investigate how well the *proposed method* performs is covered.

Chapter 4 contains a selection and the evaluation of the results

Chapter 5 comprises the discussion. The study results are compared with related studies, moreover are the limitations of the research discussed.

Chapter 6 covers the conclusions and recommendations for the use and improvement of the *proposed method* as well as recommendations for future work.

2

Background research

2.1. Challenges for navigable area estimates when using CoVadem ship track data

Ships equipped with CoVadem technology share *Under Keel Clearance* (UKC) data from their trips with the cloud. This data is transformed into information about navigable areas via a series of transformations. Each transformation turns the data into more valuable information. However, every transformation also requires dealing with additional challenges and inclusion of more uncertainties.

The water depth is the difference between the water level and the bed level (see Figure 2.1). Navigable areas are those areas where the water depth is larger than what is needed for navigation. For the pilot project, the water depth at $t = t_1$ in a point, measured by CoVadem at $t = t_0$, is estimated with Equation (2.1) [B.J. van der Spek, personal communication, October, 2019]. The components of the equation form the guideline for this section. Moreover, in order to estimate the navigability of an *area* the point data needs to be expanded in space.

$$D_{t=t_1} = \underbrace{D_{t=t_0}}_{\S 2.1.1} + \underbrace{\Delta\zeta}_{\S 2.1.2} - \underbrace{\Delta z_{bed}}_{\S 2.1.3} \quad (2.1)$$

where:

- $D_{t=t_1}$ = estimated water depth at $t = t_1$
- $D_{t=t_0}$ = water depth, measured at $t = t_0$
- $\Delta\zeta$ = water level change between $t = t_0$ and $t = t_1$
- Δz_{bed} = bed level change between $t = t_0$ and $t = t_1$

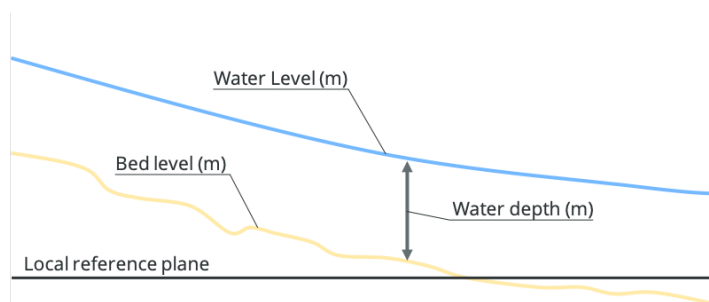


Figure 2.1: Definition sketch; note that both bed level and water level (and thus water depth) in rivers vary in time and space [van der Mark et al., 2015]



Figure 2.2: A CoVadem box, similar to the ones installed on the participating ships sailing the Chindwin river (courtesy Rolien van der Mark, modified)

2.1.1. Initial UKC data processing

The UKC data, the measured water column below the ship, is initially transformed to full water depths. In order to do this, the UKC is added to the relative position of the echo sounder to the water line. This subject is primarily the task of the company CoVadem and the topics are included here superficially for completeness only.

1. Internal measuring errors

The under keel clearance (UKC) is measured with echo sounders. The echo sounder utilises the elapsed time between sending a signal and receiving its backscatter to calculate depth. Two types of errors are important for UKC meters: systematic and random errors. Systematic errors (also called systematic bias) are consistent, repeatable errors that are usually caused by measuring instruments that are incorrectly calibrated [Gucma et al., 2017].

2. Relative position of the echo sounder

The relative position of the echo sounder compared to the water level should be added to the UKC (see Equation 2.2). The draught, squat and trim of the ship depend primarily on ship loading, flow velocities, sailing velocities and the shape of the ship [van der Mark et al., 2015].

3. GPS corrections

When echo sounder and GPS transmitter are not positioned in the same place, corrections must be made for the location of the CoVadem data. For the Chindwin pilot project, an *all-in-one* CoVadem box is installed where GPS transmitter and echo sounder are in the same module (see Figure 2.2).

This transformation requires a number of considerations (e.g., draft of the ship, intrinsic measurement errors).

$$D_{measurement}(x, y, t) = D_{keel\ clearance}(x, y, t) + D_{draught}(x, y, t) + D_{squat}(x, y, t) \quad (2.2)$$

$D_{keel\ clearance}$	=	under keel clearance
$D_{draught}$	=	draught of the ship
D_{squat}	=	depth due to squat and trim of the ship

2.1.2. Hydrodynamics

The previous section discussed the calculation of the water depth at the location (x, y) and at time (t) of measuring. However, in order to aid with navigation, the water depth must be examined at the time a ship passes the position of a measurement. Therefore hydrodynamics are included.

Estimated and/or forecasted water levels can be measured or modelled. Near gauging stations the water level can be read directly. Interpolation between gauging stations is also possible [van der Mark et al., 2015]. Further away from gauging stations, or in the case of water level forecasting, a model is necessary. The Navigation

Table 2.1: Dominant morphodynamic processes for braided rivers (from [Lighthart, 2017])

	Process	
System forcing processes	Hydrological variations	
	Sediment input in system	
	Availability erodible sediment	
	Bed roughness	
Internal flow and sediment transport influencing processes	Sediment transport primary flow	
	Sediment transport secondary flow	
	Turbulent flow	· Dunes
		· Confluence scour
		· Eddies
	Bed-slope effect	
	Bank erosion	

with Nature pilot project uses a regression model to determine the boundary conditions for a SOBEK model (from Bart-Jan van der Spek).

2.1.3. Morphodynamics

The water level is not the only thing that changes, the morphology changes with time as well. The dynamic interacting between the morphology and forcing of the water is called morphodynamics. Currently morphodynamics are not included in CoVadem. Therefore CoVadem measurements have an increasingly larger uncertainty with time. The uncertainty can be decreased in two ways:

1. Limiting the time a CoVadem measurement is used

Some (user defined) time window can be determined during which CoVadem measurements are deemed reliable. A shorter time window leads to a lower uncertainty from morphodynamics. It also leads however, to a decrease in utilisable data. van der Mark et al. [2015] used a time window of two weeks and found a MAE in the order of 20 cm (that includes the measurement and hydrodynamic uncertainty).

2. Inclusion of morphodynamic processes

When morphodynamic processes are included, the bottom data is no longer used statically but updated with expected changes in the morphology, reducing the uncertainty. A downside to this approach is the difficulty to include the vast number of morphodynamic processes correctly (see Table 2.1). If included incorrectly, inclusion of morphodynamic processes can lead to a false notion of safety.

More in general, the magnitude of the uncertainty due to morphodynamics is related to the sediment transport [de Vriend et al., 2011]. Sediment transport is related to the flow velocity to the power 4 to 5 [Engelund and Hansen, 1967]. Figure 2.3 shows two graphs displaying hydrographical data for the Chindwin. The left graph shows the 10-year averaged discharge and water levels near Monywa. The right graph shows (estimated) sediment transport rates near Kalewa. Data was provided by DWIR. Two apparent regimes can be distinguished. The first regime covers the monsoon-period during which massive amounts of sediments are transported. The second regime is the low-water regime during which only a very limited amount of sediment transport takes place and water levels are low. This latter regime is the regime that is relevant for the Navigation with Nature pilot project: it is during this period that navigation is hampered due to limited depth. The data suggests that the morphodynamic activity is also much lower during this period. It is unclear how the morphodynamic activity in the Chindwin relates to the morphodynamic activity present during the study of van der Mark et al. [2015].

2.1.4. Spatial data scarcity

CoVadem data is measured in points. Presenting a set of navigable points to captains is not a product, therefore these points are extended in space. Two different approaches are possible [Kleinhans and van den Berg, 2011]:

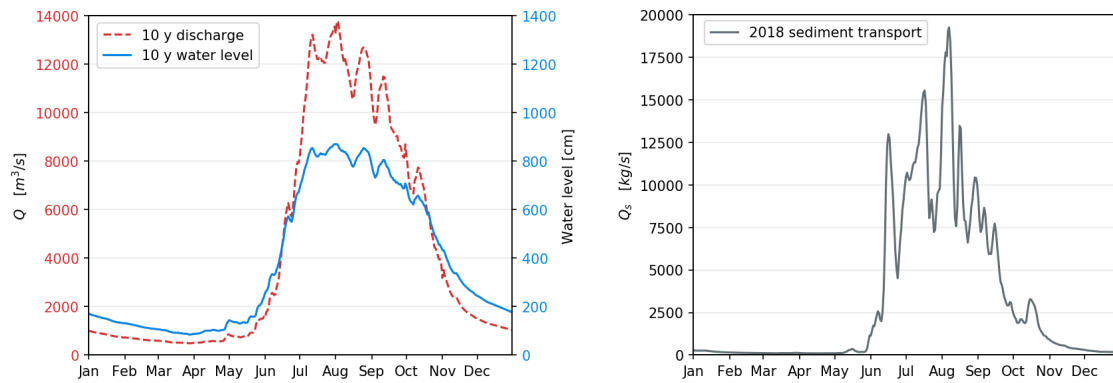


Figure 2.3: Two graphs displaying the large seasonality of the Chindwin. The left figure shows the 10 year averaged discharge and water level near Monywa. The right figure shows sediment transport for 2018 near Kalewa. Over 96% of sediment transport takes place from June through October. (Source DWIR, interpretation in Python)

1. Data-driven approach

On one hand of the spectrum is the data-driven approach. A good example is linear interpolation. Such an approach is preferred when data is abundant (e.g., along a trackline of data)

2. Physics-based approach

On the other hand of the spectrum is the physics-based approach, using knowledge of the morphology to determine the morphology around measured points.

When distances between measurements are in the order of a few meters, interpolation is acceptable. Along ship tracks of CoVadem data for example, the distances between measurements are in the order of 1 - 8 m and a data driven method is used [Peters et al., 2015].

For the pilot project, with 10 participating CoVadem ships sailing on a 1 km wide river on a > 400 km long river stretch, distances between ship tracks can presumably be up to a few hundred metres. In that case, interpolation between the data points will retrieve very large uncertainties and a physics-based approach can better be used.

2.1.5. Discussion of uncertainties

A case study for the Dutch Rhine river showed that the mean absolute error between CoVadem-derived and accurately measured bed levels was in the order of 20 cm [van der Mark et al., 2015]. For this study, CoVadem tracks were collected over a two week period. The benchmark bathymetry consisted of highly accurate dense multi-beam measurements collected at an unknown date sometime during the two weeks. The study case shows that the combined uncertainty of (1) the transformation from under keel clearance data to water depths, (2) the inclusion of water levels and (3) the influence of erosion/sedimentation is still relatively small (O 20 cm). It would be unrealistic to extrapolate the results from van der Mark et al. [2015] directly to the Chindwin:

1. van der Mark et al. [2015] used gauge stations to read the water levels. For the Chindwin a hydrodynamic model is used, that also forecasts the water levels. A higher uncertainty is expected there.
2. The study of van der Mark et al. [2015] was conducted with data collected between April and September. During these months the morphodynamic activity on the Rhine is very low [Kater et al., 2012]. The Chindwin pilot project is relevant during the low water period when navigation is hampered [Project description, 2019]. During this period the morphodynamic activity is also low. It is likely that the Chindwin is still more dynamic compared to the Rhine. Hence the uncertainty induced by the morphodynamics for the Chindwin is presumably higher, but this is not known for sure.

However, this research aims to estimate the navigable area *around* CoVadem data through inclusion of knowledge about the morphology. Around the data the morphology changes. Especially when distances become larger (e.g. 100 m) the bathymetry can change more in the order of metres than a few centimetres.

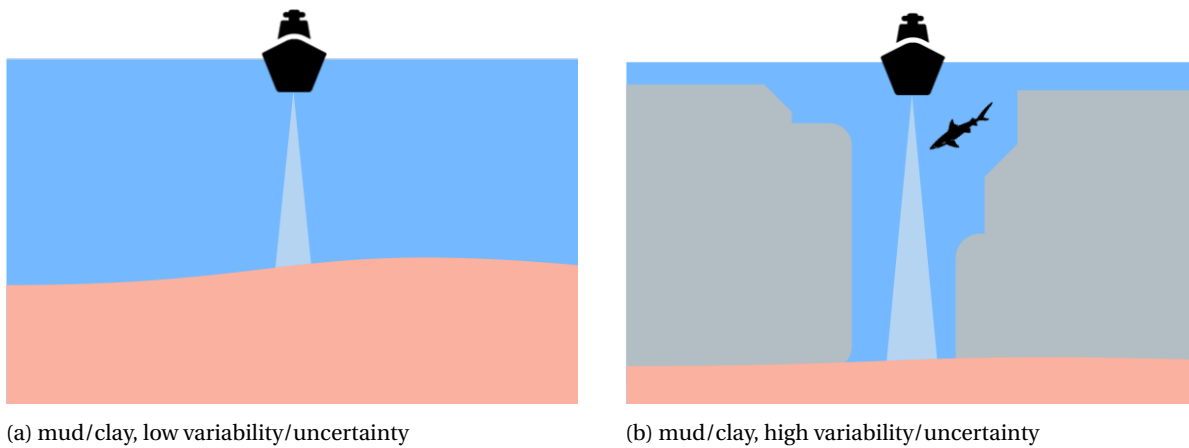


Figure 2.4: Knowledge about the river bed material can provide information about the variability/uncertainty of the morphology around measured data

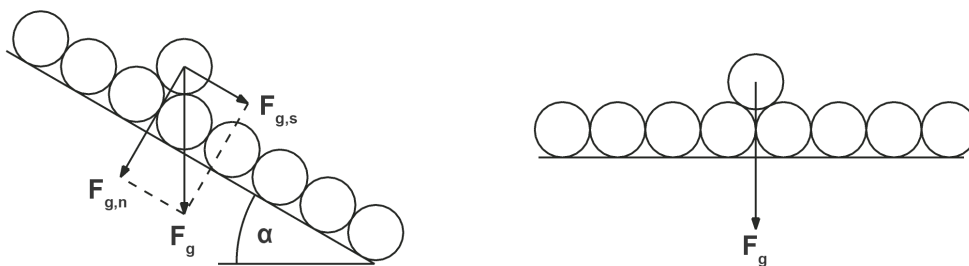


Figure 2.5: Forcing on a grain positioned on a sand bed for two different angles ($\alpha = 30^\circ$ and 0°)

2.2. Morphology information from physics-based models

River physics forms an extensive field of study. Knowledge from river physics can be used in a physics-based model to provide more information about the morphology. Three alternatives for physics-based models are discussed (in ascending order of complexity).

2.2.1. River bed characteristics

The type of river bed material contains information about the variability of the river bed. This information can be used in combination with CoVadem data. Some bed materials indicate a more gentle morphology (e.g., mud/clay, Figure 2.4a), while others indicate a more volatile morphology (e.g., when large rocks are present, Figure 2.4b).

The Chindwin river bed consists primarily of sand [van der Velden, 2015]. Figure 2.5 shows for two different slopes the direction of the forcing on a sand grain. The left figure shows the limit slope for incidence of motion for spherical, compacted grains. Based on this assumption the maximum angle α of 30° is determined. This angle represents the critical slope from which particles positioned on top of it will not slide off.

In reality sand grains are not perfectly spherical and can be compacted in such way that angles of internal friction of around 40° can be reached [Ghazavi et al., 2008, Terzaghi, 1934]. However, this 40° slope is reached under idealised conditions only and in reality a maximum angle of 30° is sufficient for larger scale slopes [Koloski et al., 1989].

Based on the previously made assumption of a sandy bed with maximum internal angle of friction of 30° a conservative estimate of a navigable area around CoVadem ship track data can be made. The concept behind this is visualised in Figure 2.6. The navigable width is based on the additional water depth, D_{extra} :

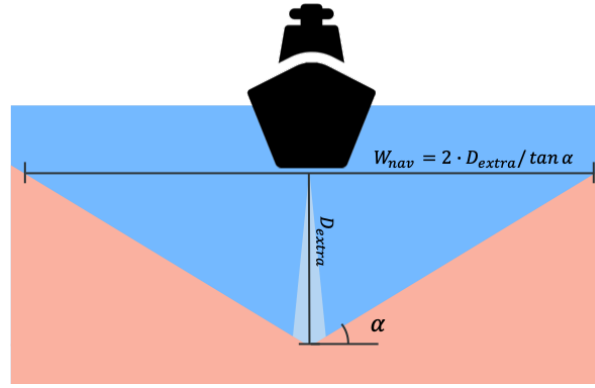
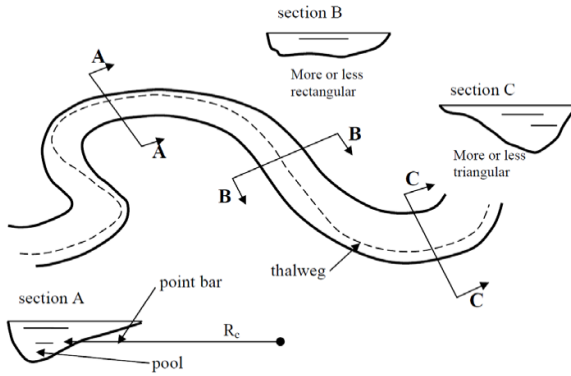
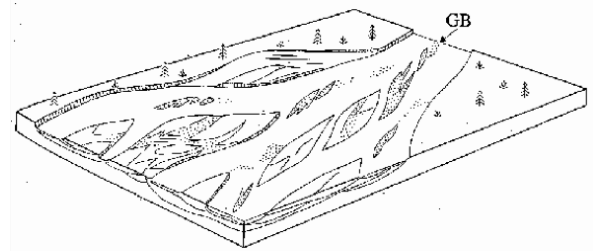


Figure 2.6: Minimum navigable width around a CoVadem trackline expressed as a function of the depth below the ship and the maximum soil slope.



(a) Meandering river [Crosato, 2008]



(b) Braided river [Miall, 1996]

$$D_{extra}(x, y, t) = D_{measurement}(x, y, t) - D_{navigation}(x, y, t) \quad (2.3)$$

$$W_{nav}(x, y, t) = 2 \cdot D_{extra}(x, y, t) / \tan \alpha \quad (2.4)$$

where:

$D_{measurement}$	= water depth derived from CoVadem measurements	[m]
$D_{navigation}$	= water depth required for navigation	[m]
α	= internal angle of friction	[°]
W_{nav}	= width determined as safe for navigation	[m]

The navigable 'width' in a point is in reality a circle around the point. Because data in longitudinal direction is very dense (up to a few meters maximum, [Peters et al., 2015]), the circles can be translated into a navigable width perpendicular to the trackline.

2.2.2. Axi-symmetric solution

The axi-symmetric solution, based on the work of Crosato [2008], provides an analytical method to couple physical aspects of a river directly with its cross-section scale bathymetry. The axi-symmetric solution can be used as an estimate for the bathymetry in alluvial, meandering rivers with mild curvature (see Figure 2.7a, [Crosato, 2008]). First the underlying formulas are discussed, followed by an analysis of the D-RATIN tool, a model based on the axi-symmetric solution.

Theory of the axi-symmetric solution

For friction dominated rivers (such as the Chindwin) the flow velocity can be estimated with the Chézy formula [Holland, 2006]:

$$u = C\sqrt{iR} \quad (2.5)$$

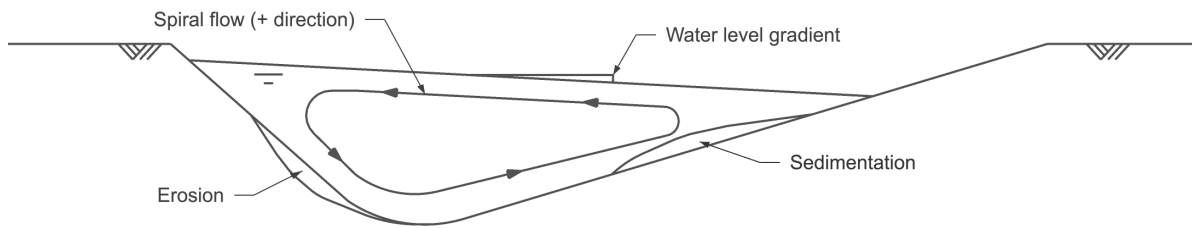


Figure 2.8: Cross-section in a river bend. The cross-sectional water level gradient is induced by the centrifugal force. Close to the surface the influence of the bottom friction to counter the centrifugal force is smaller than near the bottom. Therefore a net flow towards the outer bend will occur in the upper part of the water column. A return current evolves near the bed to close the mass balance.

The Chézy formula describes the mean flow velocity for steady, turbulent open channel flow [Allaby, 2008]. Steady flow refers to a state where fluid properties (e.g., temperature, pressure and velocity) do not change over time [de Vriend et al., 2011]. For rivers where the water depth is small compared to the river width ($h/B \ll 1$), the hydraulic radius (R) approaches the water depth h . Furthermore is the average flow velocity u equal to $Q/(Bh)$. Including the above in the Chézy formula, it can be rewritten into an expression for the mean water depth of a cross-section:

$$h_0 = \left(\frac{Q}{BC\sqrt{i}} \right)^{2/3} \quad (2.6)$$

where:

h_0	= zero-order water depth	[m]
Q	= total discharge	[m ³ /s]
B	= river width	[m]
C	= Chézy roughness coefficient	[m ^{1/2} /s]
i	= longitudinal river slope	[-]

Equation (2.6) describes the tendency of the average water depth in a channel [Crosato, 2008]. The formula however, does not take into account any secondary processes. The centrifugal force on the water in river bends is one of these processes. This forcing causes the presence of helical flow. The effect that helical flow has on the bathymetry is shown in Figure 2.8. The axi-symmetric solution includes helical flow in the formula. The full equation for the axi-symmetric solution holds:

$$h_{(n)} = h_0 e^{A f(\theta) n / R_c} \quad (2.7)$$

from Crosato [2008]

where:

A	= coefficient related to the influence of helical flow	[-]
$f(\theta)$	= function based on Shields	[-]
n	= coordinate orthogonal to the streamline	[m]
R_c	= radius of curvature	[m]

The required input values A and $f(\theta)$ are defined as:

$$A = \frac{2a}{\kappa^2} \left(1 - \frac{\sqrt{g}}{\kappa C} \right) \quad (2.8)$$

from Jansen et al. [1994]

$$f(\theta) = \frac{0.85}{E} \sqrt{\theta} \quad (2.9)$$

from Zimmerman and Kennedy [1978]

with θ and E :

$$\theta = \frac{u^2 + v^2}{C^2 \Delta D_{50}} \quad (2.10)$$

from Shields [1936]

$$E = 0.0944 \left(\frac{h}{D_{50}} \right)^{0.3} \quad (2.11)$$

from Talmon et al. [1995]

$$\Delta = \frac{\rho_s - \rho_w}{\rho_w}$$

where:

a	= calibration coefficient	[-]
κ	= von Karman constant (≈ 0.44)	[-]
g	= gravitational acceleration	[m/s^2]
C	= chézy roughness coefficient	[$m^{1/2}/s$]
θ	= shields parameter	[-]
u, v	= flow velocity in streamwise and transverse direction	[m/s]
D_{50}	= mean grain size diameter	[m]
Δ	= relative density sediment	[-]
ρ_s, ρ_w	= density of sediment and water respectively	[kg/m^3]

Model application of the axi-symmetric solution

The *Deltares - Rapid Assessment Tool for Inland Navigation* (D-RATIN) consists of a physics-based model that is constructed around the axi-symmetric solution. The tool is developed for scarce data environments where a quick analysis of the river properties is desired [Zervakis, 2015]. The tool boasts the advantage of simplicity and ease of (large scale) implementation [Beltman, 2016]. Due to its simplicity, however, also its performance can be limited when physical processes unaccounted for by the tool have an influence on the morphology. In the exploratory phase of this research, direct application of the D-RATIN tool to determine navigable areas has been investigated. The most important findings are:

1. Coarseness of the model

The estimate of the morphology with the axi-symmetric solution depends only on hydrographical parameters. Beltman [2016] and Zervakis [2015], applying the D-RATIN tool, both use the validation measurements to calibrate the tool. Such an approach is possible as long as validation measurements are available. This is not the case when the axi-symmetric solution is applied to a 'real' case where no validation measurements are present. Moreover, even when validation measurements *are* available, the estimate of the axi-symmetric solution is coarse. To illustrate this, the cross-sectional average water depth for a stretch of Chindwin river near Kalewa was calculated from measured data (Figure 2.9). Consecutively the equilibrium depth formula (2.6) was fitted through the measured data. Calibration took place by minimisation of the Mean Absolute Error (MAE), a commonly used evaluator [e.g., van der Mark et al., 2015]. The retrieved minimum MAE is a considerable 1.6 m. Note that this is the optimum value, without the ability to calibrate with validation measurements the MAE equal at best but presumably higher.

2. Inclusion of river banks

The axi-symmetric solution (Eq. (2.7)) calculates a very deep channel for the outer bends and a very shallow channel near the inner bends. River banks are not by the included, which are naturally present in reality. Zervakis [2015] dealt with this problem by indicating a part of the river as the river banks and including an upward slope for those areas. The study determined the width of the river banks based on available data from cross-sections. CoVadem data however, generally follows the deeper parts of the channel [van der Mark et al., 2015] and is collected predominantly along the flow instead of transverse to it. Therefore an estimate the location of the river banks is expected to be more difficult to make based on CoVadem data.

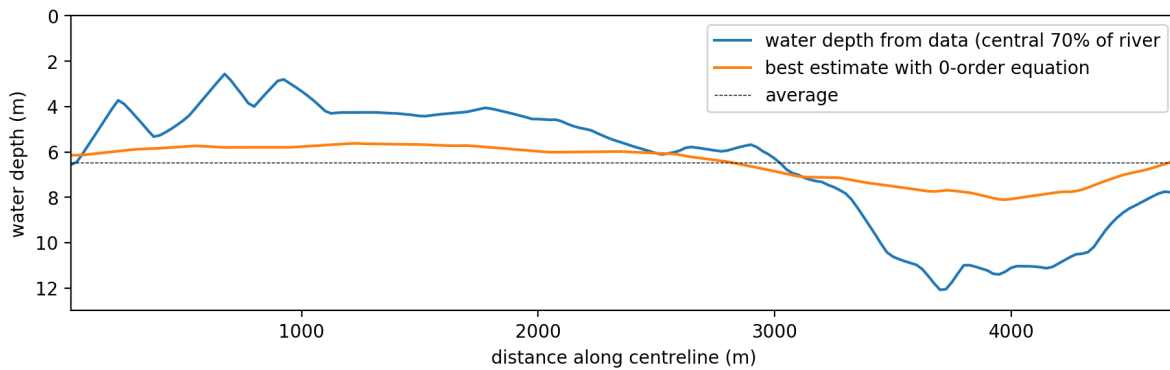


Figure 2.9: The cross-sectional averaged water depth (blue line) and the estimated cross-sectional averaged water depth with the equilibrium flow equation (2.6). Mean Absolute Error = 1.6 m

3. Applicability of the axi-symmetric solution to a seasonal river in a sediment rich environment

The axi-symmetric solution assumes a mildly curved, alluvial, meandering river. Areas in the Chindwin exist where the river does not meet these criteria (e.g., braided sections, Figure 2.7b). For those areas of the river, the assumptions of the axi-symmetric solution (e.g., helical flow as one of the dominant forcers for the cross-section shape) do not hold [de Vriend et al., 2011]. Exploration with satellite imagery resulted in the suggestion that:

- (a) Straight stretches of the river seem less applicable to the axi-symmetric solution.
- (b) Parts of the river with a more dynamic channel alignment seem more less applicable to the axi-symmetric solution.

2.2.3. Computational Fluid Dynamics (CFD) model

Computational Fluid Dynamics (CFD) models (e.g. MIKE21C, DELFT3D) aim to calculate physical processes on a numerical grid. CFDs can be used to model both hydrodynamic and morphodynamic processes. A CFD model uses a combination of boundary conditions, initial conditions such as planimetric forcing by fixed banks and physical processes in a river to estimate the morphology [Kleinhans, 2010, Schuurman et al., 2013]. A CFD model can potentially not only provide in more information about the current morphology, but also include morphological changes. A problem with a complex problem such as DELFT3D is that it is more difficult to alter the model internally. It is recommended to investigate using a CFD model.

2.3. Morphology information from remote sensing

Remote sensing offers effective ways to detect surface water from space [Campbell and Wynne., 2011]. Over the last decade, a rapid increase in data availability and data quality has provided the opportunity to study river geometry dynamics with an (ever) increasing frequency and resolution [Huang et al., 2018].

Possible applications for remote sensing to aid with river analysis are extensive. A grasp of the possibilities: river networks and widths can be identified [e.g., Allen and Pavelsky, 2018, Pavelsky and Smith, 2008, Shilpi et al., 2014, Thissen, 2019]. Surface water extent can serve as a proxy for discharges [e.g., Smith et al., 1995, Smith and Pavelsky, 2008] or water levels [e.g., Durand et al., 2010, Khan et al., 2011, Mersel et al., 2013, Pipitone et al., 2018]. Even flow velocities can be estimated with remote sensing [e.g., Chen and Mied, 2013].

Remote sensing can be subdivided in two major groups: active and passive remote sensing [Patel and Singh, 2013]. The differences have been analysed in Appendix A.1. For this research, two passive remote sensing methods, able to provide an estimate of the morphology, have been further analysed. The methods, generally used for coastal regions, are discussed in §2.3.2 and §2.3.3. Both methods, as a starter, require satellite data. The most commonly used available satellite missions can be found in Appendix A.1. Both methods also require to be able to distinguish between water and non-water surfaces. The topic of water detection from remote sensing imagery is therefore discussed first.

2.3.1. Surface water detection methods

Passive electro-optical (EO) sensors sense a wide variety of bands from the electromagnetic spectrum [Casasent et al., 1978]. The differences in absorption and reflection for certain bands can be used to detect water. Some examples of indices used for water detection are given in Table 2.2. The most widely used indices for surface water detection are the *Normalized Difference Water Index* (NDWI, McFeeters [1996]) and the *Modified Normalized Difference Water Index* (MNDWI, Xu [2006]). The indices essentially use the difference in detected radiance between two different spectral bands and normalises these such that a value between -1 and 1 is found. A high index refers to a high probability of presence of water.

Different water detection methods perform differently under different conditions. Under the influence of e.g. turbidity, temperature and light the reflectance in various bands can change. Dooren [2019] found both the NDWI and the MNDWI to be working well for the Chindwin. The MNDWI index however 'can enhance open water features while efficiently suppressing and even removing built-up land noise as well as vegetation and soil noise' better than the NDWI [Xu, 2006].

Table 2.2: Different formulae used for water detection from multispectral satellite imagery. Bandwidths Green: 0.525-0.600, NIR: 0.845-0.855, SWIR1: 1.560-1.660, SWIR2: 2.100-2.300 (all μm)

Name	Formula	Reference
NDWI*	$\frac{\rho_{nir} - \rho_{swir}}{\rho_{nir} + \rho_{swir}}$	[Gao, 1996]
NDWI**	$\frac{\rho_{green} - \rho_{nir}}{\rho_{green} + \rho_{nir}}$	[McFeeters, 1996]
MNDWI	$\frac{\rho_{green} - \rho_{swir1}}{\rho_{green} + \rho_{swir1}}$	[Xu, 2006]
AWEI	$4 \cdot (\rho_{green} - \rho_{swir1}) - (0.25 \cdot \rho_{nir} + 2.75 \cdot \rho_{swir2})$	[Feyisa et al., 2014]

*for water detection in vegetation ** for water detection in water bodies

2.3.2. The 'water-line' method

Morphology of inter-tidal zones can be constructed from remote sensing images with the 'water-line' method [e.g., Donchyts et al., 2019, Mason et al., 1995, 2010, Murray et al., 2012]. The water-line method assumes that higher lying points in the bathymetry are covered by water less often [Mason et al., 1995]. Water masks from multiple satellite images are linked with measured or modelled water levels to calculate the morphology. For river application, the water-line method can in theory provide an estimate of the bathymetry for those areas that are positioned between the low water level and the high water level (see Figure 2.10, right). To the best of the authors' knowledge, the water-line method has never been used before on non-tidal rivers.

Applicability of the water line method for river environments

Two aspects in the water-line method limit the potential added value for river applicability in general and to navigable area estimates in particular:

1. Temporal scale water cycle

In order for the water-line method to function, at least one high-low water cycle should be included in the satellite data [Mason et al., 2010]. For coastal regions, this is equal to the temporal scale of the tide (12-24 h) [Bosboom and Stive, 2013]. For seasonal rivers however, a cycle is in the order of a year [van der Velden, 2015]. This is important because the water-line method assumes a static morphology where the water level is the only variable [Mason et al., 1995]. For a short, tidal cycle, such an assumption is acceptable. However, when one cycle consists of a whole year, the morphology can change significantly during that period which will reduce the accuracy of the water-line method.

2. Water-line method only applicable to the higher lying parts of a river

When applied to coastal areas, the water-line method calculates the morphology of the inter-tidal area. For a seasonal river this translates to the area that becomes dry/wet between low and high water. To



Figure 2.10: False colour images near Kalewa Bridge. The left image is taken during the monsoon period, the middle shortly after and the right image is taken approaching the end of the dry period. The red line displays the area of the river where the 'water-line' method can provide information about the bathymetry

increase navigational safety, especially information of the morphology below the low water line is required.

Based on the above two points, direct application of the water line method to aid with navigation seems not promising. There are however, also parts in the water line method that *do* show potential to be used to aid with navigation in river environments:

1. **Use as an indicator for channel stability**

The water line method compares different water masks and assumes that the changes in the morphology are small compared to the changes in water level. However, this process can also be reversed. It is hypothesised that, when images with similar water levels are compared, the water line method can be used to study (changes in) the morphology.

2. **Water-line method can be used to determine a guaranteed water depth at specific locations**

Some areas of the river are, even when many years of satellite images are used, 'always' covered by water. These areas have been compared with local measurements. Some exploration with the data found that over 99% of the measurements had a bed level lower than the lowest water level in the foregoing year to the measurements. This information can be used to determine some guaranteed water depth at the areas that are 'always' covered by water:

$$\text{guaranteed water depth} = \text{current water level} - \text{lowest water level last year}$$

2.3.3. Inverse-depth estimated from multispectral optical satellite imagery

The second method to estimate morphology is inverse-depth estimated from multispectral optical satellite imagery. The method, introduced by Lyzenga [1978], uses the difference in water reflectance between shallow and deep water to estimate water depth. Applications can be found in e.g. Pacheco et al. [2015] and Kibele and Shears [2016]. The method was found unsatisfactory for the Chindwin because of the high (and fluctuating) turbidity levels. The high turbidity levels prevented a stable and usable relation between reflectance and water depth.

2.4. Selection of models and methods

In the previous sections alternatives that can provide information about the morphology have been discussed. A selection was made based on applicability, scalability and implementability.

Out of the two discussed remote sensing methods none were selected. Primarily the applicability to a seasonal river with high levels of turbidity hampers the applicability of both the methods. The flaws of the methods were already discussed in §2.3.2 and §2.3.3. However, an alternate form of the water line method will be used (introduced in §3.1, discussed in detail in §3.8.3).

Out of the discussed physics-based models, only application of a CFD model was *not* selected. From the alternatives, a CFD model presumably has the highest applicability because it can include more complex processes [Kleinhans and van den Berg, 2011] compared to the other two models. However, the scalability and implementability of such a model is presumably lower. The decision not to pick a CFD (read: DELFT3D) is slightly arbitrary.

The decision to use analytical models instead of a CFD model boasted the advantage to build the models from scratch and tailor them specifically for navigable area estimates in combination with CoVadem data. The demands for a navigable area estimate are different from those of a morphology estimate. For navigation, an overestimated navigable area (read: possible grounding ships) is more severe than an underestimated navigable area. For a navigable area estimate it is therefore better to use the unfavourable expected bed instead of the average expected bed. Both the analytical models can be easily tailored for such a purpose. DELFT3D, as standalone software would be more difficult to alter for this purpose.

3

Methodology

3.1. Overview of the proposed models and reliability indicators

In Sections 2.2 and 2.3 alternatives for additional knowledge of the morphology have been discussed. In §2.4 criteria for selection were determined and a selection was made. In this section, the findings are joined in the *proposed method*. This research revolves around proving if and how well the proposed method works.

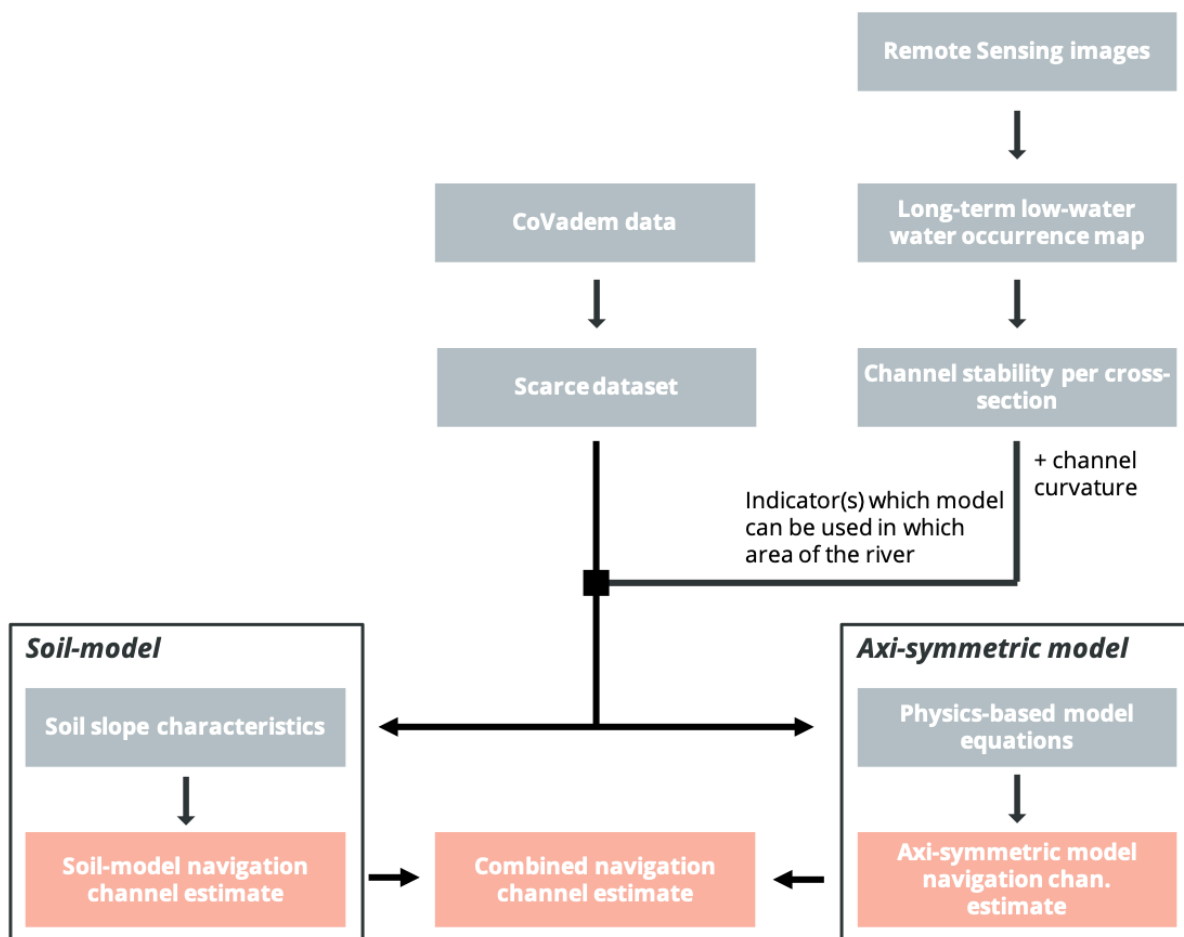


Figure 3.1: Proposed utilisation method

Overview proposed method

Figure 3.1 displays a flow chart of the proposed method. In order to estimate a navigable area around CoVadem ship track data, two physics-based models have been developed: the soil-model and the axi-symmetric model. When this thesis refers to 'the models', the soil-model and axi-symmetric model are meant. Both models use CoVadem data as the basis for calculation. The underlying assumptions of the axi-symmetric model presumably do not hold for every part of the investigated river type. It is proposed to use the stability of the low-water channel (determined with remote sensing) and the curvature of the river, to indicate where the axi-symmetric model can and cannot be safely applied. Channel stability and river curvature are together referred to as the 'reliability indicators'. The reliability indicators are only applicable to the reliability of the axi-symmetric model.

Soil-model

The first physics-based model is named the soil-model, based on §2.2.1. This model assumes knowledge of the type of bed material present at the investigated river. Based on the characteristics of the bed material, the maximum possible slope in the river is determined. In the case of sand this is around 30 degrees (§3.6). This 30 degrees (upward) slope is assumed around CoVadem data to determine a navigable area. This model is elaborated on in more detail in §3.6.

Axi-symmetric model

The second physics-based model is named the axi-symmetric model. Please note that the model is very different from the D-RATIN tool. This model also uses CoVadem data as the basis for calculations. The transverse slope of the river bed around the data is approximated with the axi-symmetric solution (§2.2.2). Moreover does the model make some assumptions about the presence of river banks and sand dunes. The entire model is discussed in detail in §3.7.

Reliability indicators

This thesis hypothesises that additional indicators related to the curvature and channel stability can indicate where the axi-symmetric model should and should not be used. It is suggested that the axi-symmetric model will not work everywhere for rivers like the Chindwin: when physical processes that are not included by the model play an important role, the ability of the model to estimate the navigation channel presumably goes down. Two proposed indicators for the reliability of the axi-symmetric model are:

1. Channel stability (remote sensing)

The axi-symmetric model does not account for higher order bathymetry artefacts such as river braids. Some exploration with remote sensing imagery suggests that areas where braiding is present, generally have a more dynamic alignment of the low-water channel. A remote sensing method is proposed to investigate how stable/dynamic the river is locally. It is hypothesised that the channel stability (the *stability score*, §3.5.4) is an indicator for the reliability (the *safety score*, §3.8.1) of the axi-symmetric model.

2. Curvature ratio

The axi-symmetric solution assumes that the influence of helical flow governs the shape of the river bed. For straight reaches of the river, a rectangular shape of the river bed is expected according to the axi-symmetric solution [Crosato, 2008]. The investigated river for this research is highly seasonal and located in a sediment rich environment [ADB, 2016]. Some exploration with satellite imagery and available local measurements suggests that the axi-symmetric solution seems more applicable for river bends compared to straight reaches. In straight reaches (more often) complex bed formations seem to occur. not accounted for by the axi-symmetric solution. The second hypothesis is therefore that the curvature of the channel (*curvature ratio*, §3.5.5) can serve as an indicator for axi-symmetric model reliability.

This research will go as far as to investigate if curvature and/or stability are promising indicators for the axi-symmetric model reliability. For application to a real case, some *threshold* values for one or for both indicators should be determined that determine when application of the axi-symmetric model is acceptable. This decision should be made by the end-user.

Reading guide

The lay-out for the remainder of this chapter is build up as follows:

1. preparing the prerequisites for the *proposed method* (datasets, curvilinear grid, etc., §3.2 to 3.4)

2. approach for utilisation/implementation of the *proposed method* (§3.5 to 3.7)
3. approach for validation of the *proposed method* (§3.8)

3.2. Study case selection

The proposed method is applied to, and validated for, four different study cases: Khamtee, Htamanthi, Kalewa and Monywa. All of the study cases are located along the Chindwin. Selection of the study cases was based solely on data availability.

3.3. River discretisation

A physical river cannot be used to perform calculations. Therefore the river must be discretised i.e., cast in a shape that a computer can process. First a river polygon, numerically representing the river boundaries was created. Afterwards a grid is created with the grid construction tool of the Deltares Rapid Assessment Tool for Inland Navigation (D-RATIN). The grid contains the nodes in which calculations take place.

The river polygon was drawn by hand around available measurements from the study cases, with help of the Deltares QUICKIN tool [QUICKIN, 2020]. The grid representation of the river is formulated in curvilinear coordinates. Mosselman [1991]: "This allows the use of a boundary-fitted computational grid, suited for rivers with a curved centre-line and a non-uniform width." A curvilinear model representation is very commonly applied for river representation [e.g., Crosato, 2008, Ligthart, 2017, Olsen, 2003, Zervakis, 2015].

Appendix B.1 describes in more detail all the steps (and considerations) carried out to create the curvilinear grid. The most important choice considering the grid was the grid cell sizing. Grid cell dimensions have been based on typical ship dimensions. A cell length of 25 m was picked. Curvilinear grids have varying cell widths depending on the river width. A total of 101 grid cells in transverse direction was picked, leading to an average cell width of about 6 m, approximately equal to the width of a CoVadem ship. This size was chosen on purpose: one navigable grid point now represents one ship size of navigable area.

3.4. Processing data

The axi-symmetric model and soil-model require a CoVadem dataset to work. No real CoVadem data was available for the duration of this research. Therefore synthetic CoVadem ship tracks have been created. The navigable area estimates of the axi-symmetric model and the soil-model are moreover compared with a ground truth. Creation of the ground truth bathymetry as well as creation of the synthetic CoVadem tracks is discussed in this section.

3.4.1. Available data

Local bathymetry measurements were collected by small boats equipped with single beam echosounders, sailing across the river numerous times. The data was provided in CAD files by DWIR. The collected data is not structured, but a general estimate of the spatial resolution yields 80 x 30 m (along flow x transverse) for all study cases. The available single beam data near the study case of Htamanthi is shown in Figure 3.2. Preferably the measurements for the ground truth show high density and high accuracy. The sample data from the various Chindwin sites is relatively coarse and nothing is known about the measurement uncertainty either. Since it is the best data available, it serves as the ground truth nevertheless. Additional in depth information about the applied procedure for data formatting, cleaning and georeferencing can be found in Appendix B.2.

3.4.2. Ground Truth bathymetry

In the previous sections the creation of the curvilinear grid and the manipulation of measured data have been discussed. However, grid points and sampled points do not naturally coincide. The measured data has been projected on the curvilinear grid with the QUICKIN triangulation tool. This tool uses Delaunay triangulation

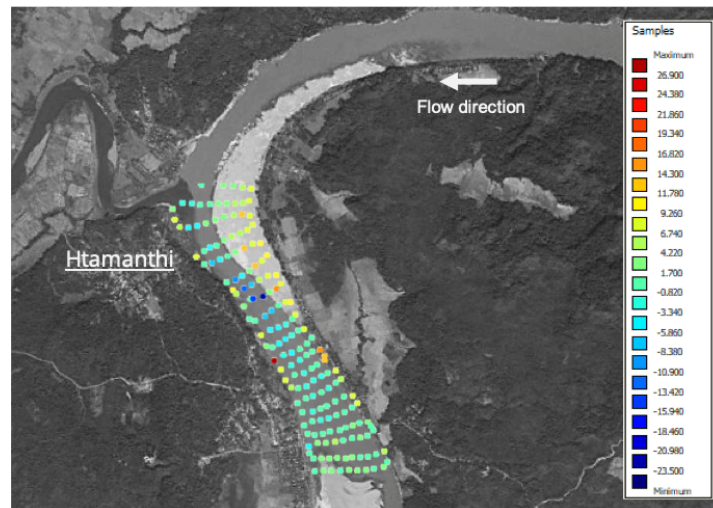


Figure 3.2: The available single beam measurements for the study case of Htamanathi

between the sampled points and Linear Barycentric Interpolation for the projection of the triangulated area on the grid nodes. This procedure is further explained in Appendix B.3. An example of the bathymetry near Kalewa after projection to the grid is given in Figure 3.3 (left).

3.4.3. CoVadem datasets

In the original setup of this thesis the CoVadem datasets were supposed to come from actual ships mounted with CoVadem technology. Technical issues/delays have caused for unavailability of that data for the duration of the research. Therefore a change was made and instead the CoVadem tracks are extracted from the ground truth bathymetry.

Ships generally tend to sail up and down the river. A CoVadem trajectory therefore looks like a set of data points roughly following the flow lines [Wirdum van et al., 2015]. Synthetic CoVadem tracks were created by selecting one measured point per cross-section from the Ground Truth bathymetry. The synthetic CoVadem tracks are some arbitrary example of the data that is presented to the physics-based models. An example of two extracted CoVadem tracks is given in Figure 3.3 (right).

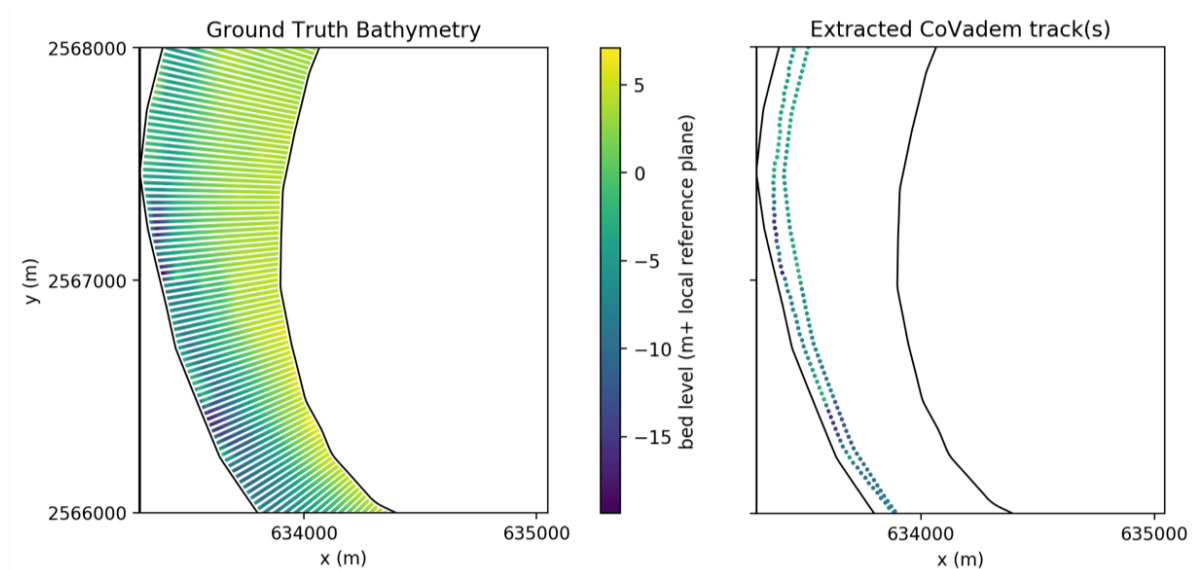


Figure 3.3: Left: ground truth bathymetry Kalewa study case. Right: two (arbitrary) CoVadem tracks, extracted from the ground truth



Figure 3.4: Rug plot of clean and obstructed satellite images near Kalewa. Satellite images are selected from Landsat 5, 7, 8 and Sentinel-2 missions. 10 years of data during March and April are selected. Red lines represent images that were discarded because of clouds. The green lines represent clean images, used for further analysis.

3.5. Reliability indicators

In §2.2.2 the axi-symmetric solution was discussed. It was stated that the axi-symmetric solution does not work for every (location of a) river. It was hypothesised in §3.1 that river curvature and/or the stability of the low-water channel can serve as indicators for the reliability of the axi-symmetric solution. This section explains how the *stability score* and *channel curvature ratio* are defined and calculated.

3.5.1. Data selection, retrieval and cleaning

The stability is investigated with help of remote sensing. Data is used from Electro-Optical remote sensing from Landsat 5, 7, 8 and Sentinel 2 missions. Calculations on the images were processed remotely on Google servers, managed through the Google Earth Engine environment [Gorelick et al., 2017]. Earth Engine uses parallel computing, which reduces calculation time [Gorelick et al., 2017].

Section 2.3 explained how differences in water surface can indicate changes in bathymetry. It also explained that a difference in bathymetry is best noted when water levels between images are equal. Based on these findings, the decision was made to compare satellite imagery taken during the months March and April only. During those two months water levels are lowest and varied the least [DWIR, 2014]. The decision for a 2 month period was based on data availability: a requirement was set that at least 1 (clear) satellite image per year had to be present for all sites (see Figure 3.4).

A time window for the satellite data of 10 years was chosen. The chosen period is a trade-off. When a shorter length is picked unstable areas can be flagged as stable when the channel is 'accidentally' in the same place as the previous year(s). When the investigated period is stretched far enough back however, any piece of the river will appear unstable. The maximum period is limited by the availability of satellite imagery. Time windows of 2, 5, 10 and 20 years were compared in §B.4. The 10 and 20 year time window performed best and did not show much difference. The 10 year window was selected, because it required less computational power.

Some of the selected images were obstructed by clouds. Those images were removed from the selection. Cloud detection was based on the work of Zhu and Woodcock [2012, 2014]. Implementation of the theory through the *getMostlyCleanImages* Earth Engine script by Genna Donchyts. A *Cloud Frequency Delta* of 0 was used, similar to e.g., Dooren [2019], Thissen [2019]. The results with this method looked fine after visual inspection: almost all images with clouds were effectively removed. It is not within the scope nor nature of this thesis to dive further into the subject of cloud detection.

3.5.2. Water detection

The previous section discussed the selection of satellite images, water detection is the next step. The *Mean Normalised Difference Water Index* (MNDWI) is used to detect water. The reflectance in every pixel in ev-

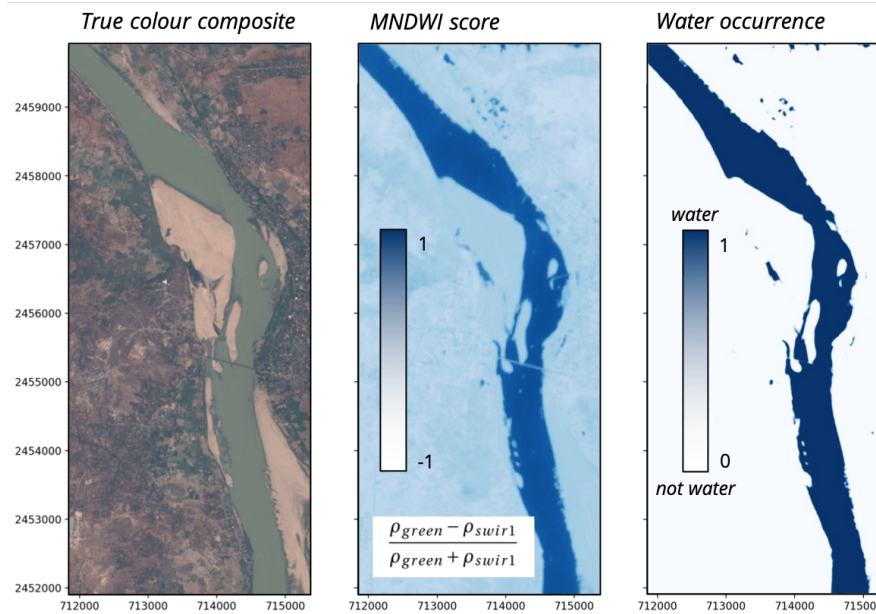


Figure 3.5: Left image shows the true colour composite. The center image shows the same location after calculation of the MNDWI value in every pixel. The right image shows the likelihood that a pixel is covered by water

ery remote sensing image is sensed by multiple spectral bands. The MNDWI uses the *green* and *short wave infrared* bands and *normalises* them (explained in §2.3.1).

In Figure 3.5 three images are shown. The left image displays the *true colour composite*, similar to how our eyes see the world. The middle images shows the calculated MNDWI for every pixel. Here the extent of the river is much more clear. The MNDWI gives a value between -1 and +1 for every pixel. A dynamic threshold between -0.1 and 0.3 was used (see 2.3.1. A threshold must be determined to decide when a pixel is actually water or not. The threshold is not exactly the same for every location and every image [Donchyts et al., 2016]. Donchyts et al. [2016] suggests a dynamic threshold ranging from -0.1 to 0.3. This threshold is applied in the right image. Every value lower than -0.1 becomes zero in the right image (white). All MNDWI values 0.3 or above become 1 (dark blue). Values in between are stretched to unit scale (0 to 1).

3.5.3. Water occurrence

The way the images are selected and how water is detected have been discussed. The next step is to combine multiple images and investigate how much the river changes through the years. Figure 3.6 displays 10 years of images where water has been detected.

The images are, after the steps in §3.5.2, piled and averaged. Figure 3.7 displays the combined so-called *water occurrence* map on the right side. The images that were used to construct this image are shown in the *rug plot*. Areas where the low water channel shows more variability can be (qualitatively) determined from the image. The upper and lower part of the river in the image seem more stable, with more dark blue areas. The centre area however shows that the channel at this location changes a lot during the years. The channel stability is quantified in the next step.

3.5.4. Channel stability score

With the steps from the previous paragraphs finished, it is now possible to create maps that qualitatively show stable and unstable areas of a river. In order to use this information quantitatively, the *channel stability score* was developed. The stability score is a measure to indicate how stable the low-water channel is locally. The stability score is calculated based on what part of the channel width is considered stable:

1. The rasterised data from the *water occurrence* map is projected on the curvilinear grid (see Figure 3.8)

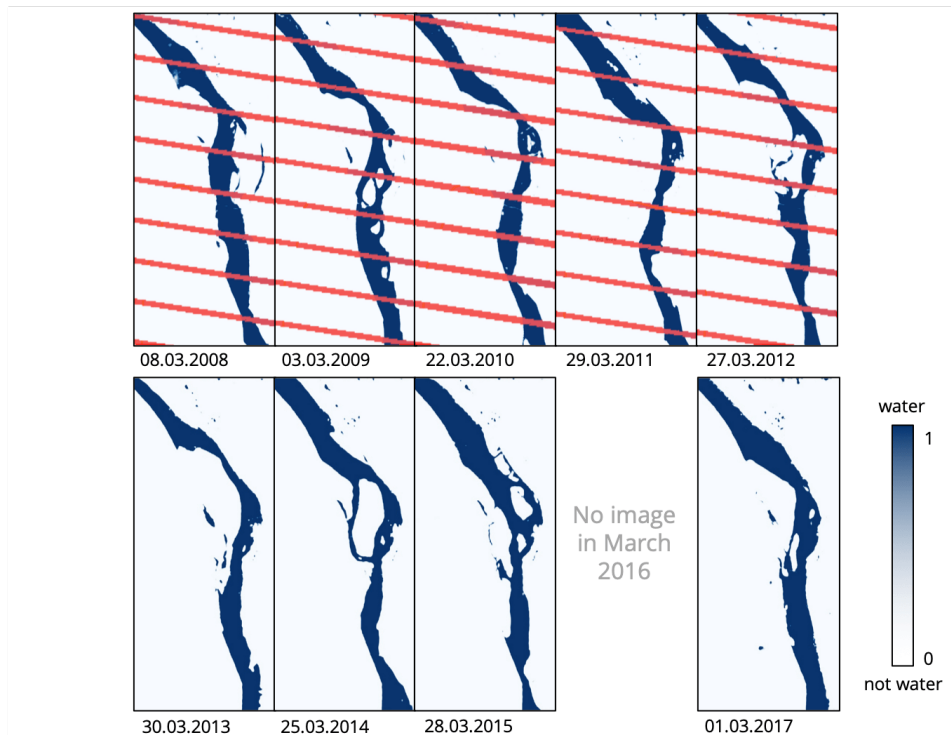


Figure 3.6: *Water occurrence* calculated for 10 images taken in March from 2007 to 2017. The data gaps (red areas) from 2008 to 2012 are due to a sensor issue with Landsat 7

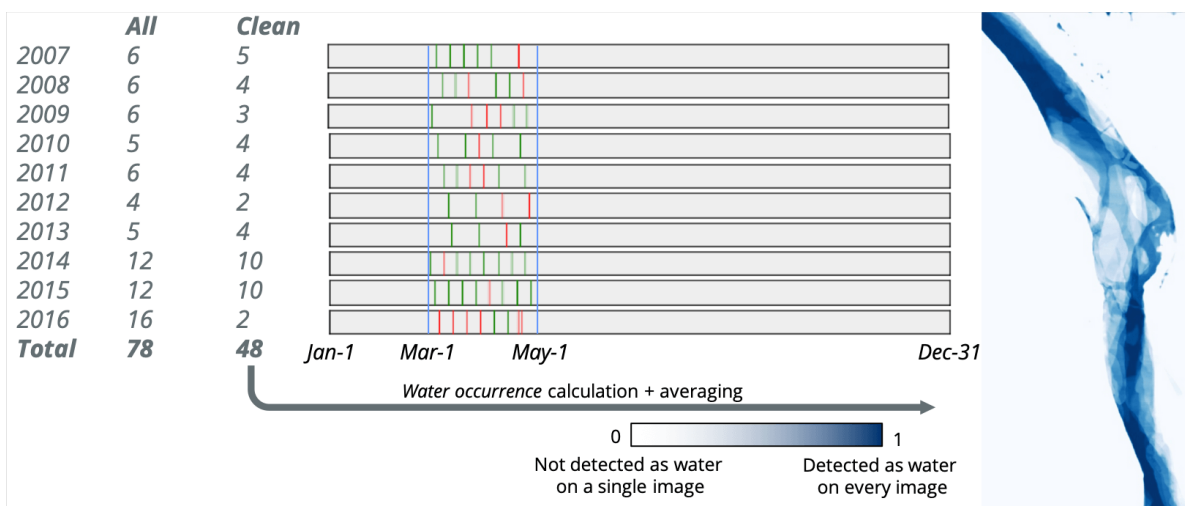


Figure 3.7: *Water occurrence* map calculated by detecting water and averaging over 48 satellite images near Monywa, Myanmar

2. A threshold *water occurrence* value is used to classify every node in the grid as either stable or unstable
3. The fraction of stable nodes in a cross-section determines the *stability score* of that cross-section

$$\textit{stability score} = \frac{\text{stable nodes in cross-section}}{\text{all nodes in cross-section}} = \frac{\text{stable width}}{\text{total width}}$$

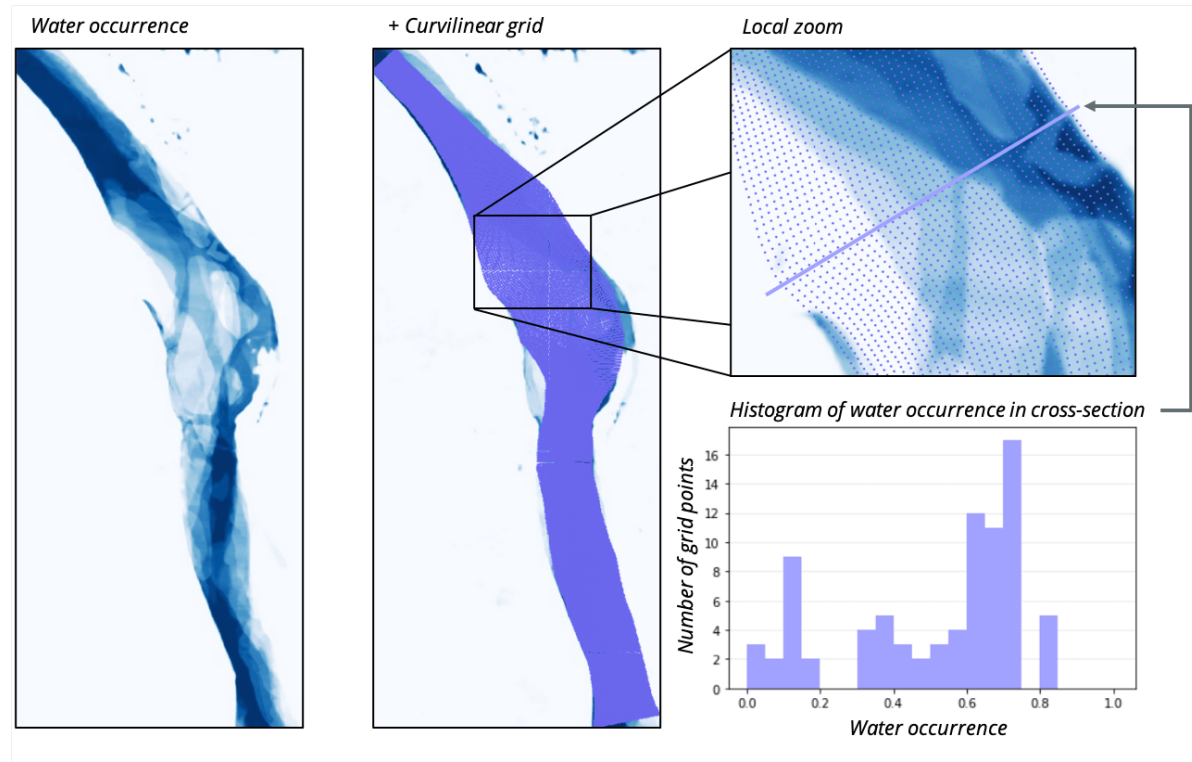


Figure 3.8: *Water occurrence* information is combined with a curvilinear grid. This enables the possibility to evaluate the *water occurrence* per cross-section. The histogram shows the distribution of the *water occurrence* values in the purple cross-section (see *Local zoom*).

In Figure 3.9 an example is given where the stability score is calculated for two cross-sections. The respective cross-sections are indicated by the purple lines in the *water occurrence* maps. The histograms display the *water occurrence* values for all the nodes in the cross-section. In order to indicate which nodes are determined as stable, a threshold must be determined. A node is considered stable when it either most of the time is, or most of the time not is part of the low-water channel.

In Figure 3.10 the stability score along the river for Monywa is plotted for different thresholds (that determine when a node is 'stable'). A threshold of 0.15 and 0.85 means that a node is considered stable when the *water occurrence* value in that node is either below 0.15 (stable dry) or above 0.85 (stable wet). When the requirements of what a stable node is are loosened, the stability scores increase. The green and grey line appear to make better use of the whole zero to one spectrum of the stability score. Therefore it is suggested that those can be better used as indicators for the reliability of the axi-symmetric model. One of the aims of this research is to prove that the stability score can be used as an indicator the axi-symmetric model reliability. The 0.15 and 0.85 threshold (green line) was picked and used for the remainder of this research.

3.5.5. Curvature ratio

The second indicator for axi-symmetric model reliability that is investigated is the river curvature ratio. In order to determine the curvature the dimensionless curvature ratio (γ) was used that is calculated by dividing the river width (B) by the radius or curvature of the river (R_c).

$$\textit{curvature ratio} = \frac{\text{river width}}{\text{radius of curvature}}$$

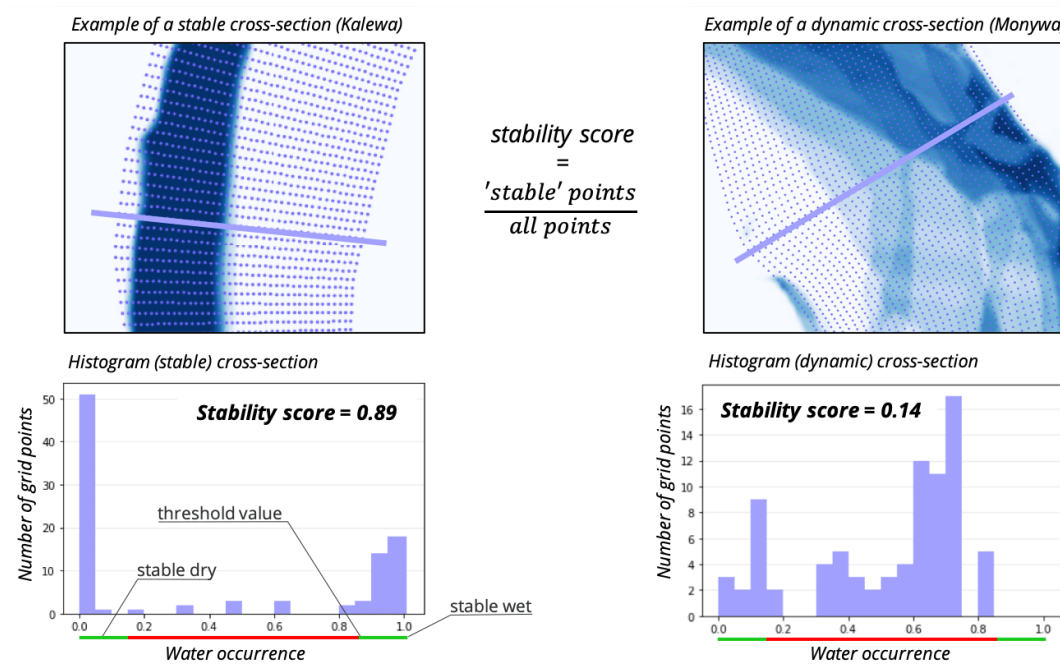


Figure 3.9: Stability score for two cross-sections.

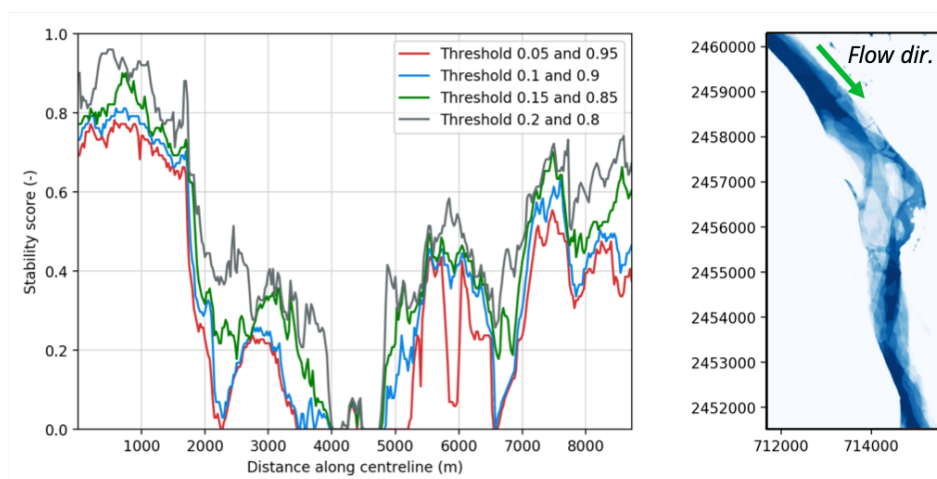


Figure 3.10: Stability score calculated along an 8.5 km river stretch near Monywa. The score is high for cross-sections where the channel location does not change much over the years. A threshold value is necessary to distinguish between stable and unstable point. The decision for the *threshold* value influences the stability score.

The radius of curvature is calculated along the centreline of the grid. To do so, the Menger curvature is calculated. In mathematics, the Menger curvature of a triple of points is the inverse of the radius of the unique circle that passes through those 3 points [Léger, 1999]:

$$c(p_0, p_1, p_2) = \frac{1}{R_c} = \frac{2 \sin \angle p_0 p_1 p_2}{|p_0 - p_2|} \quad (3.1)$$

where:

- p_0, p_1, p_2 = coordinates (x, y) of points to deduct radius of curvature from [m]
- $\angle p_0 p_1 p_2$ = the angle made by a line from p_0 to p_1 to p_2
- R_c = radius of curvature for p_1 [m]

The radius of curvature for application on a grid is depicted in Figure 3.11. Three points along an n -grid line are considered for determination of the R_c in the middle point. However, the grid representation of the center line is discrete. Therefore we observe strong variability in the calculated radii of curvature along the grid. In Figure 3.12a this is depicted in the values of the inverse radius of curvature along the centreline near Kalewa. For this reason smoothing was applied to diminish steep (unrealistic) changes in curvature. A *rolling mean window* and a *Gaussian smoothing window* were tested (Figure 3.12b). Gaussian smoothing was selected because the results were smoother and seemed to follow general contours of the river better, similar to Zervakis [2015].

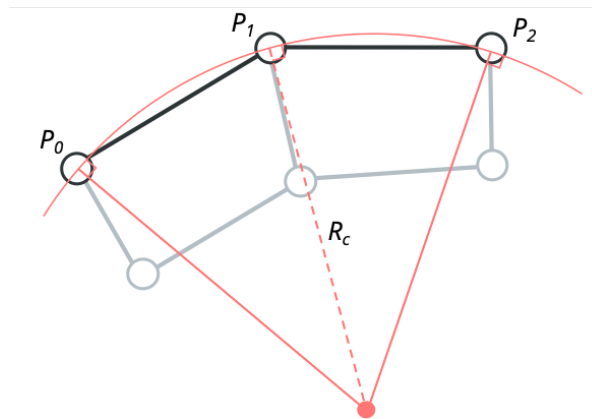


Figure 3.11: Explanation of how the radius of curvature is determined for point P_1

A smoothing window that is in the order of the width of the channel generally resulted in acceptable result. The smoothing window should be chosen large enough to smoothen unrealistic radii of curvature resulting from the discreteness of the grid. On the other hand it should be chosen small enough to not smoothen out physical changes in radius of curvature too much.

3.6. The soil-model

This soil-model is a physics based model, used to estimate a navigable area around CoVadem data. First the theory is briefly explained. After that the implementation in the model is displayed.

Based on a sampled point, P_0 , the range of possible bed levels in point P_1 at distance d away can be calculated based on the maximum possible slope in the soil. The principle is illustrated in Figure 3.13. The corresponding range is depicted on the right. The exact elevation in P_1 remains unknown. However, if the most conservative value for P_1 is used, this provides an estimate for a guaranteed least available depth. This knowledge is used in the soil-model to calculate an estimate of the navigable area around CoVadem data. The main assumption for the model to work is that the maximum slope in the bed is known. The maximum bed slope is related to the bed material. For a sandy river such as the Chindwin, the maximum slope is around 30 degrees.

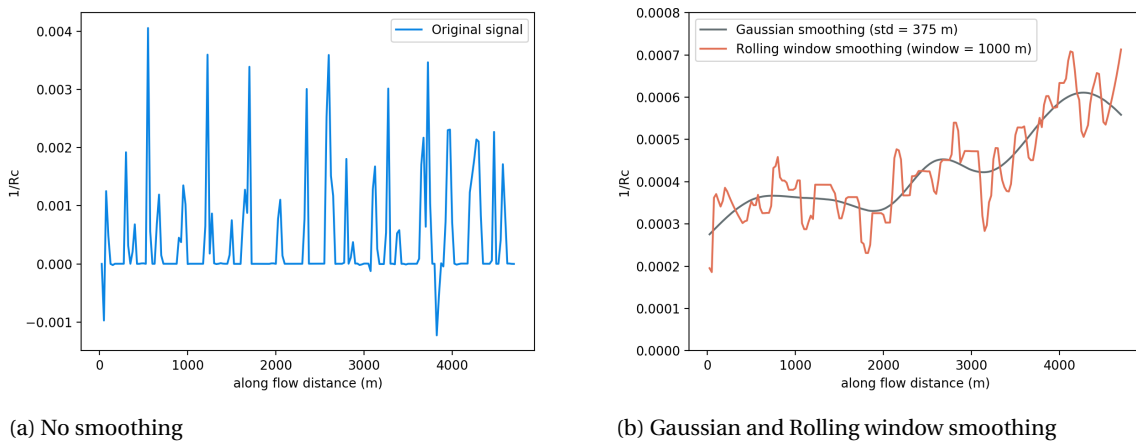


Figure 3.12: The inverse of the radius of curvature ($1/R_c$) along the center line near Kalewa. The left figure shows the original signal, notice the variability. The right figure shows the signal after Gaussian and Rolling window smoothing. Gaussian window smoothing was used by the remainder of this thesis

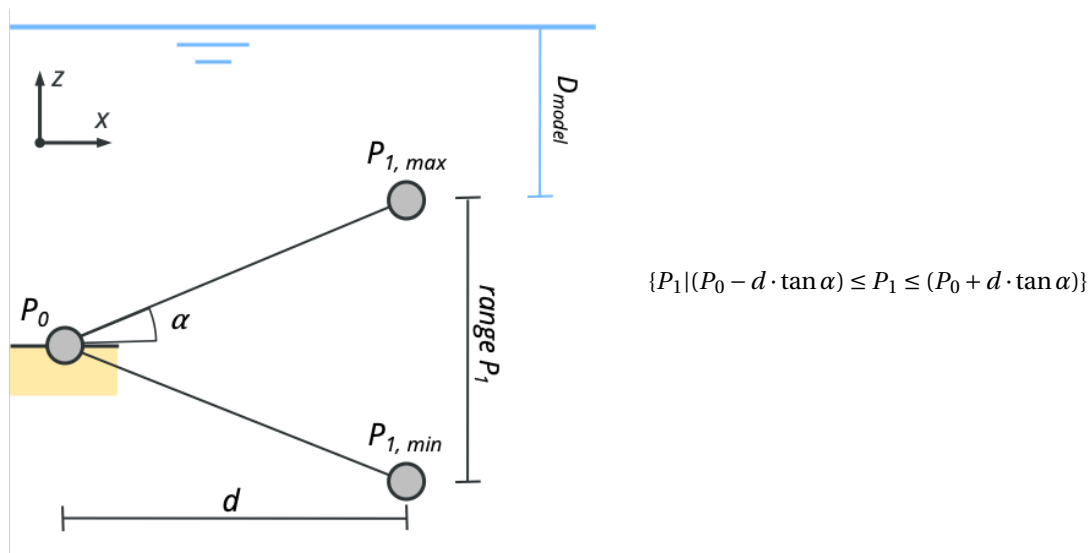


Figure 3.13: Range for the bed level of unknown point P_1 as a function of measured point P_0 , the distance (d) and maximum soil slope (α). The soil model assumes $P_{1,max}$, the most unfavourable possibility for navigation. This assumption is very conservative.

In Figure 3.14 the way the model works is explained. Data scarcity with CoVadem data is especially relevant in the direction perpendicular to the flow (§2.1.4). Therefore calculation takes place cross-section by cross-section (1D).

3.7. The axi-symmetric model

The second physics based model is named the axi-symmetric model. The model is based on the axi-symmetric solution but is approached differently compared to the work of Zervakis [2015]. An overview of how the model is implemented for a cross-section is given in Figure 3.15. The difference with the model of Zervakis [2015] lies in three aspects:

1. The calculated cross-sections from the axi-symmetric solution are fitted *through* measured data instead of calculated completely based on theory (Figure 3.15, step 5)
2. The location where the banks of the river start is unknown and therefore a conservative assumption of the location of the river banks is included (Figure 3.15, steps 3 & 4)
3. The model also includes potential presence of sand-dunes (Figure 3.15, step 6).

In the remainder of this section the motivation behind the differences as well as the implementation of the model are discussed.

3.7.1. Axi-symmetric solution

For ease of reading the governing formulae for the axi-symmetric solution are presented here again:

$$h_0 = \left(\frac{Q}{BC\sqrt{i}} \right)^{2/3} \quad (3.2)$$

$$h_{(n)} = h_0 e^{A f(\theta) n / R_c} \quad (3.3)$$

As stated above, only the transverse slope of the axi-symmetric solution is used and fitted through CoVadem data. The decision to choose for this approach was based on the following three observations:

1. Zervakis [2015] found that the RMSE in the bathymetry estimate was highly sensitive to the calibration of the model parameters. The study derived the optimum calibration through 10,000 Monte Carlo simulations and evaluating the results each time with ground truth data. The approach from Zervakis [2015] would be possible for this study as well: validation data is available to optimise the parameters. However, when applied to a real case, such validation data is not available and will likely result in a less reliable model estimate. Fitting the axi-symmetric solution through the measured data in a way calibrates the model on every cross-section.
2. The axi-symmetric formula calculates cross-sections. CoVadem boasts the advantage that even with a single track of data, at least one measurement per cross-section is present. This provides the possibility to fit the axi-symmetric solution in the cross-section plane.
3. The (mean) water depths along the Chindwin show rather large deviations even within study cases. These deviations are not included in the axi-symmetric solution.

The concept of fitting the axi-symmetric solution through the data is displayed in Figure 3.16. In order to fit this line through a measured point, the assumption that the equilibrium depth h_0 (Equation (3.2)) was calculated correctly has been dropped. When the axi-symmetric solution is fitted through a measured point the slope in that point reduces to (3.4). Below, relevant aspects of the calculation of the components from (3.4) are discussed.

$$\frac{dz}{dn} = Ah_{point} f(\theta) / R_c \quad (3.4)$$

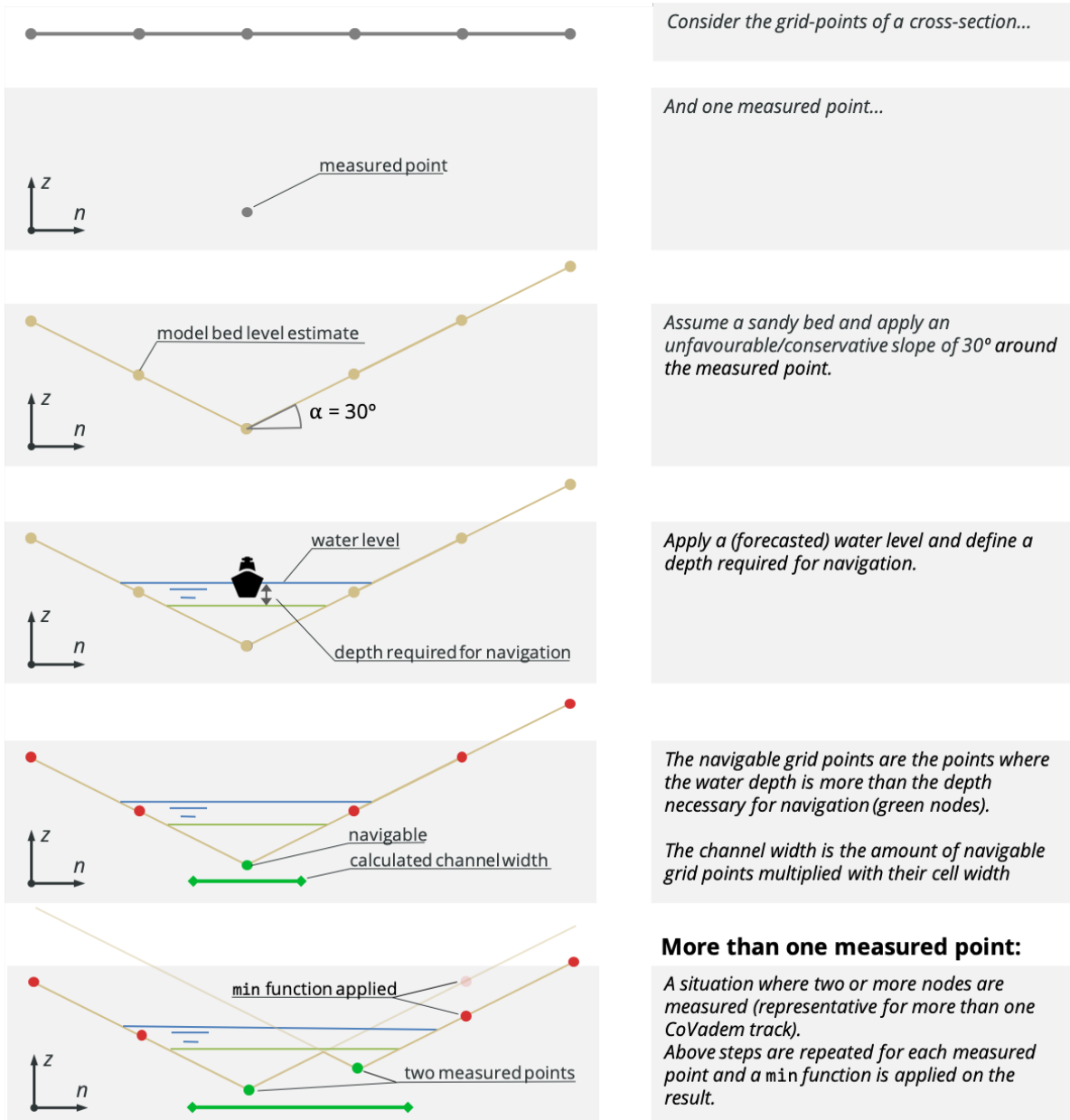


Figure 3.14: The steps for application of the soil-model

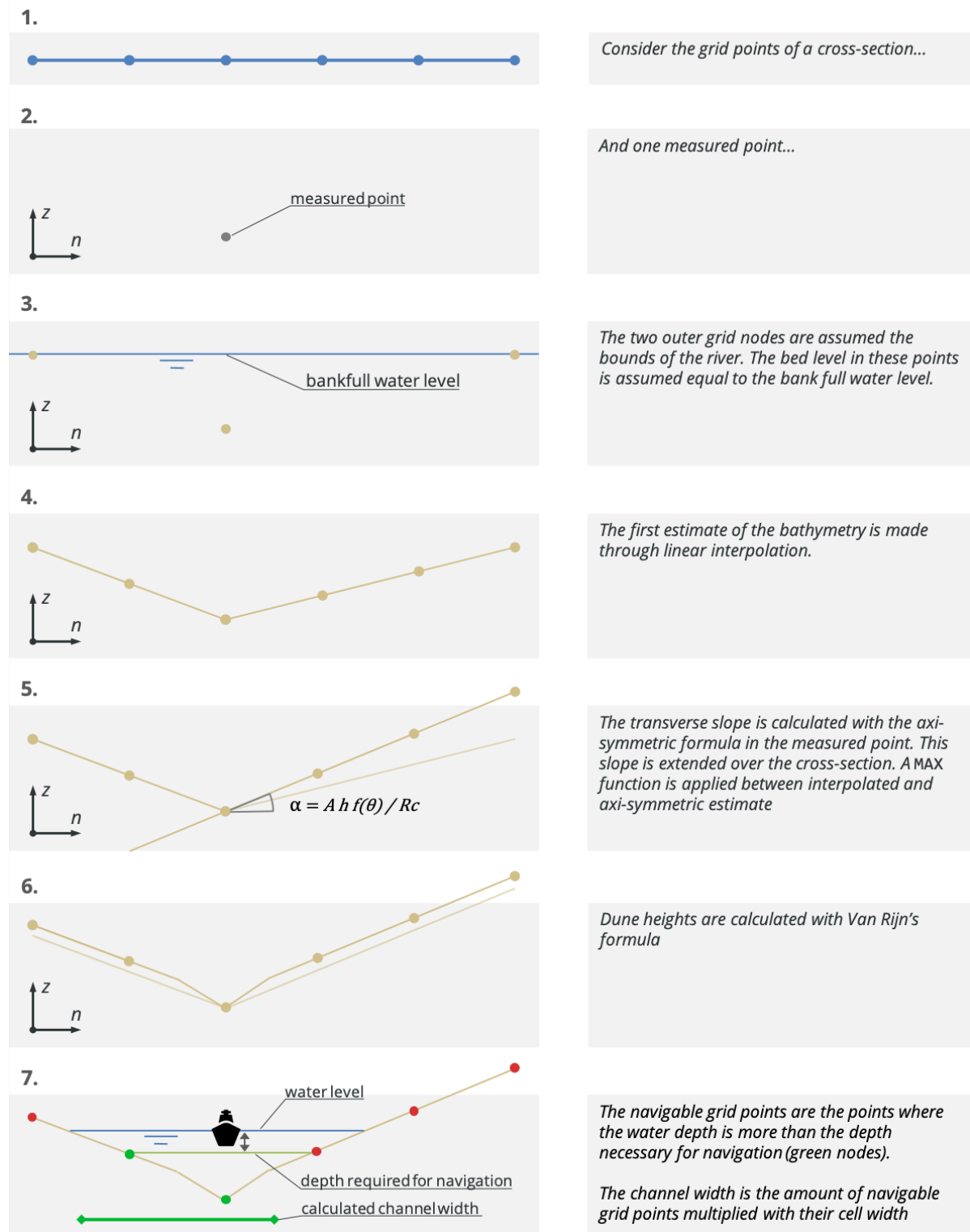


Figure 3.15: The steps for application of the axi-symmetric model

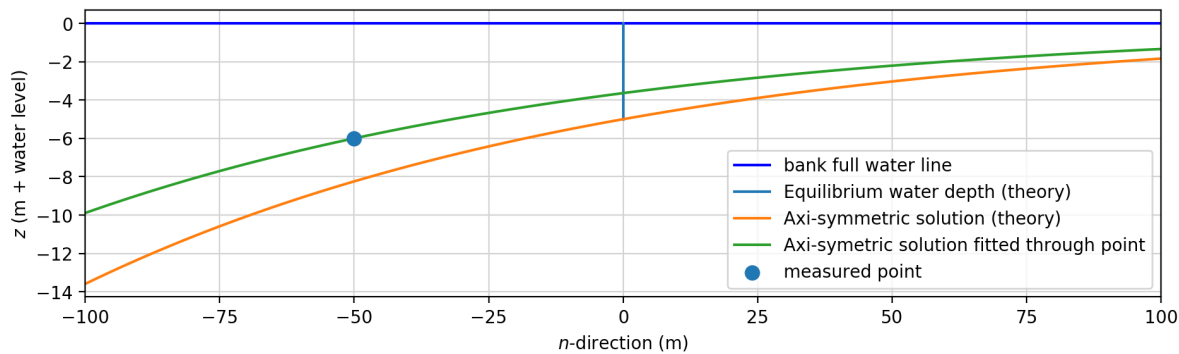


Figure 3.16: The axi-symmetric solution is applied by first calculating the equilibrium water depth (red line) (3.2) before calculating the full cross-section (orange line). This research fits the axi-symmetric solution directly through the measured data (green line)

Coefficient weighing the influence of helical flow A

The decision for the influence of the transverse bed-slope remains arbitrary but is rather important for the development of the bed [Schoorman et al., 2013]. The influence of helical flow has the highest uncertainty of the axi-symmetric solution and is often calibrated with data [Crosato, 2008]. The calibration coefficient a was calibrated iteratively by testing different values and evaluating the results. The method as described in the validation approach (§3.8) was used for this.

The water depth in measured point h_{point}

The water depth is the difference between the bed level (m + datum) and the water level (m + datum). The bank full water level is used instead of the water level encountered during measurements. This is in line with Crosato [2008] and Zervakis [2015]. This is under the assumption that the bank full river conditions are governing in determining the bathymetry. The assumption seems probable for the study cases where data is collected during high water or shortly thereafter. However, the bathymetry changes when water levels drop (with some lag). Maintaining the high bank full water level to determine the transverse slope is conservative. It might be better to use a lower water level under low water conditions. This should be investigated with measured data collected during low-water conditions and was not possible for this research.

Weighing function for the influence of the shields parameter $f(\theta)$

The shields parameter was calculated globally per study case. Zervakis [2015] assumed a global flow u velocity of 1 m/s and a negligible transverse flow v . In the available data from this research some (surface) flow velocity measurements were available. These were multiplied by 0.85 to get a rough estimate of the mean flow (0.85 based on expert consultation) and averaged in order to get an estimate of the shields parameter per study case.

Radius of curvature R_c

The radius of curvature is calculated in the same way as in §3.5.5.

3.7.2. Inclusion of river banks

CoVadem data is expected to generally follow the deeper parts of the channel (as discussed in §2.2.2). Hence no information is present of where the river bank begins exactly. To counter this, the axi-symmetric model in this thesis simply assumes that the river bank begins directly next to the measured data. The outer grid points are assumed to be the river banks. The elevation at the river banks was set equal to the bank full water level.

The bank full water level is difficult to determine for highly seasonal rivers, during the monsoon the water level can be much higher than bank full. For this reason instead the water level corresponding with the dominant discharge was used (also used in [Crosato, 2008]). The dominant discharge is a representative discharge that, when applied for a year, has the same total sediment transport as the combined sediment transport of all the observed discharges [de Vriend et al., 2011].

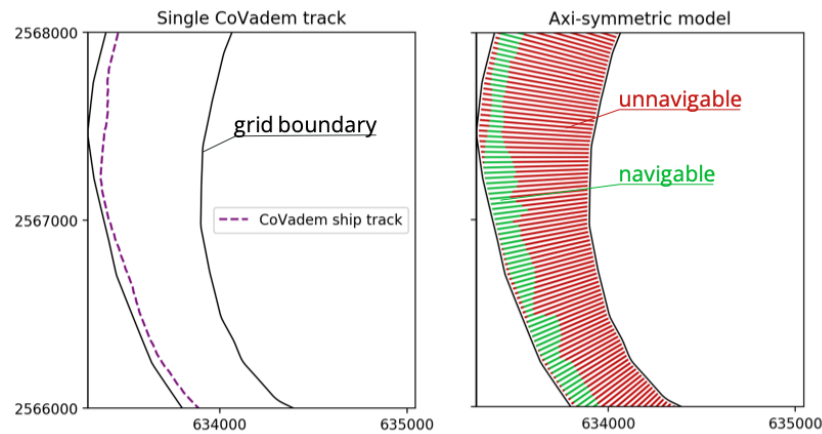


Figure 3.17: An example of how the axi-model estimates a navigable area near Kalewa.

3.7.3. Inclusion of sand dunes

The axi-symmetric solution estimates the large scale bathymetry of the river. In reality smaller scale river features play a role as well. The axi-symmetric model in this thesis therefore includes an estimate for the presence of sand dunes. The dune heights have been calculated according to the van Rijn dune classification. This is further explained in Appendix A.2. The dunes are included in such a way in the model as if the CoVadem measured point is located exactly in between two dunes (Figure 3.15, step 6).

3.8. Validation approach

Validation is the action of checking or proving the validity or accuracy of something. Validation was more-over used throughout this thesis in a constant feedback loop to improve the proposed method. This section discusses how the validity and accuracy of the proposed method is measured.

The first part of the validation approach describes the way how the performance of the physics-based model is evaluated. Two model performance indicators were developed. The first indicator is related to how safe the model is (*safety score*). The second indicator is related to how well the size of the real navigation channel is approached (*channel coverage score*). The second part of the validation approach revolves around the approach to check the hypothesis that channel curvature and/or stability (3.8.1) can serve as indicators for axi-symmetric model reliability.

3.8.1. Model validation method

A good model increases the navigable area around CoVadem data by as much as possible. At the same time should the model not give wrong channel estimates. When the model calculates an area as navigable while it is too shallow for navigation in reality, this will lead to dangerous situations.

In Figure 3.18 a model navigation channel estimate and the real navigation channel are shown (left and centre). The model estimates the navigation channel based on a CoVadem ship track. The ground truth shows the true navigation channel. The model estimate is superimposed on the ground truth navigation channel to retrieve the image on the right side. Four different types of zones are distinguished:

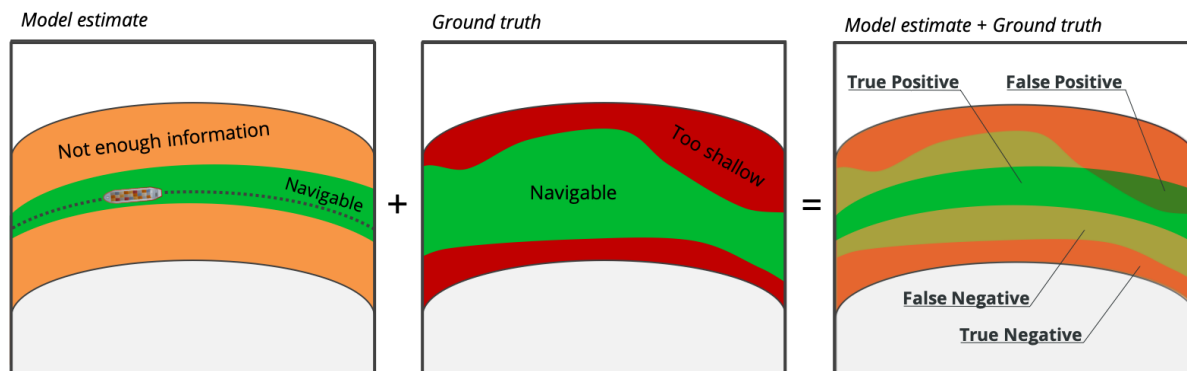


Figure 3.18: Comparison between calculated navigation channel and the ground truth navigation channel. Based on the calculated navigation channel a navigation advice is given to captains.

True Positive (TP) Correct estimate. Those areas where the model and ground truth have the same **positive** estimate of the navigability.

True Negative (TN) Correct estimate. Those areas where the model and ground truth have the same **negative** estimate of the navigability.

False Positive (FP) Incorrect estimate. Those areas that are calculated as being part of the navigable by the model while they are too shallow in reality. These areas are dangerous and can cause grounding ships.

False Negative (FN) Incorrect estimate. Those areas that are navigable in reality but calculated as navigable by the model. False Negative areas are unwanted, however their presence is not as critical as the False Positive areas. There is added value for captains in knowing more of the extent of the navigation channel (e.g., for passing other ships, adjusting speeds near bottlenecks, picking shortest routes).

The information from a map such as Figure 3.18 is used both for qualitative and quantitative analysis. The qualitative analysis critically tries to explain what is observed in the results. Questions are answered such as: When is the calculated navigation channel narrow/wide? When does the model fail? Is there a likely explanation for failure?

In the quantitative analysis only the model results are used. Two dimensionless scores were developed. The scores are used to assess how well the models approach reality:

$$safety\ score = \frac{\text{True Positive}}{\text{True Positive} + \text{False Positive}} \quad (3.5)$$

$$channel\ coverage\ score = \frac{\text{True Positive}}{\text{True Positive} + \text{False Negative}} \quad (3.6)$$

The *safety score* is an estimate for the fraction of correct calculations and therewith an indicator for the model reliability. The *channel coverage score* gives an estimate for the fraction of the real navigation that is calculated by the model. The latter score is an indicator for the added value for *smooth* navigation (easy passing of ships, shorter routing, faster sailing, etc.).

The scores can be calculated for cross-sections or areas (a river reach). When the score is calculated per cross-section a value for the *safety score* and *channel coverage score* is retrieved for every investigated cross-section separately. If an entire area is investigated, global scores are found for that area. Both scores always have a value between 0 and 1. If both scores are 1, this means that the model exactly approached the ground truth navigation channel.

3.8.2. Validation datasets

The previous section discussed the performance indicators. In order to calculate the performance indicators, the model navigation channel is compared with the ground truth navigation channel.

Ground truth navigation channel

The ground truth *bathymetry* was discussed in §3.4.2. The ground truth bathymetry is coupled with a water

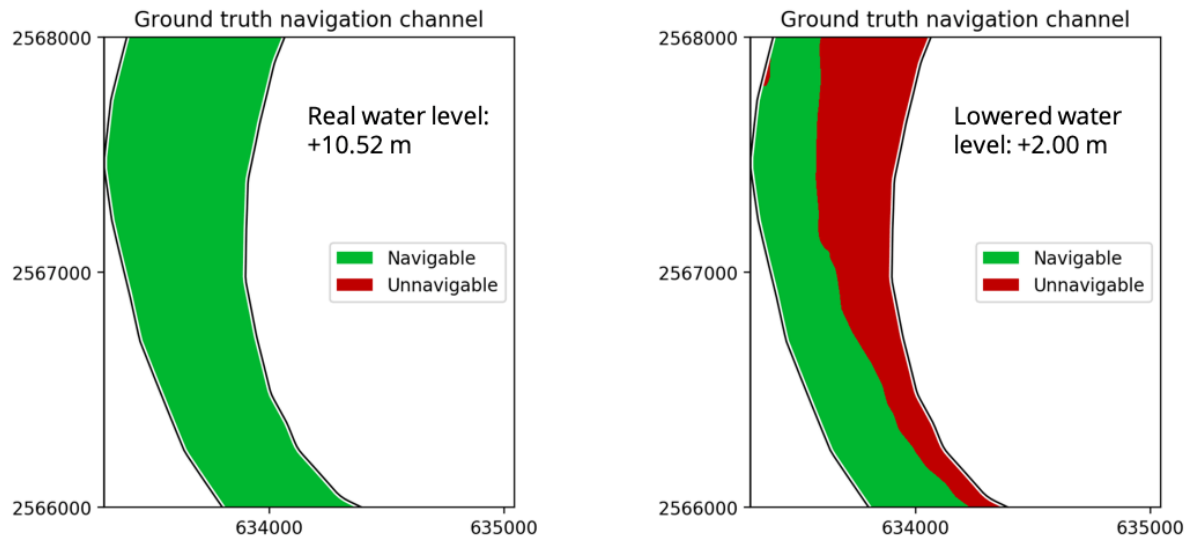


Figure 3.19: Zoom near Kalewa of the ground truth navigation channel. The left image shows the navigation channel of the river during the time that the measurements were collected (September 2016). The water level was +10.52 in the local reference plane and ships can navigate on the entire river. The image on the right shows the same location, but this time the water level is artificially lowered to represent a low water situation

level and a depth required for navigation to create the *ground truth navigation channel*. For three out of the four study cases the measurements were carried out during the monsoon period. During the monsoon the water levels are so high that the entire (measured) extent of the river is navigable (Figure 3.19, left). The water level is therefore lowered artificially to create a low water situation (Figure 3.19, right). The chosen water levels are based on the annual low water level per case study.

Model navigation channel

The physics based models use scarce data to estimate the navigable area around it. The width and alignment of the calculated navigable area depend on:

1. The arbitrarily selected 'CoVadem' data. Figure 3.20 shows the channel width and alignment calculated from two different CoVadem tracks, note the differences.
2. The model parameter calibration (only for the axi-symmetric model).

Since no real CoVadem data was available, synthetic CoVadem ship tracks were selected from the ground truth bathymetry (3.4). However, this raises the problem that the size and alignment of the navigation channel is depending on the arbitrary selection of the track line. This is not acceptable for unbiased calculation of the performance indicators. A method was developed to eliminate the bias of user-defined CoVadem track selection by calculating *all* possible CoVadem tracks. The concept of this method is visualised and explained in Figure 3.21.

Moreover is the size and alignment of the model navigation channel influenced by the model parameter configuration. This is only relevant for the axi-symmetric model. Especially one parameter, the calibration coefficient for the influence of helical flow a is known to be highly uncertain. The coefficient has been calibrated for one of the study cases, but nevertheless a sensitivity analysis will be performed to check the influence of calibration coefficient a on the performance indicators.

Understanding of Figure 3.21 is critical for understanding of how the performance indicators are calculated. Therefore some additional remarks have been added:

- The model calculates the navigation channel independently for every cross-section in the grid. Therefore the process can be explained from a single cross-section.
- Every model run one measured point per cross-section is considered. This measurement represents the location where a CoVadem ship sailed through the cross-section. Every model run provides an estimate for the navigation channel of the whole cross-section. This is the process as was explained in

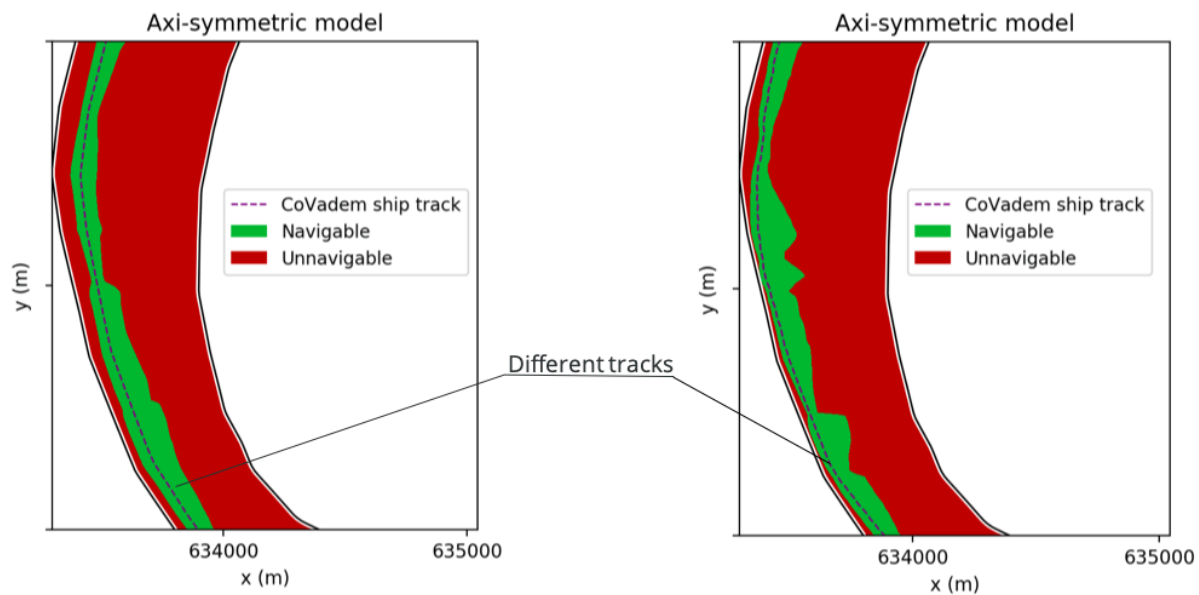


Figure 3.20: Axi-symmetric model channel estimate for two different synthetic CoVadem tracks (dotted lines) near Kalewa. Clear differences in the location and width of the channel can be observed, influencing the performance indicators. A method is developed that can diminish the effect of the arbitrary track selection on the model performance scores.

§3.6 (soil-model) and §3.7 (axi-symmetric model).

- The navigation channel location is calculated as many times as there are cross-section grid nodes. Every time the 'measured point' is altered until every possibility is calculated once.
- Some areas of the river are too shallow. No ship can sail there, so no measurement can be expected from that location. Where a ship can and cannot sail is determined by the ground truth navigation channel. The model runs that are based on 'impossible' CoVadem tracks are removed (the red crosses).
- The remaining runs are compared with the ground truth. All grid points of all remaining runs are indicated as one of the following: True Positive, True Negative, False Positive or False Negative (§3.8.1)
- The indicators are summed and the *channel coverage score* and *safety score* are calculated per cross-section. In the case that the performance indicators are calculated for multiple cross-sections at once a similar approach is used: all the False Positives, True Positives and False Negatives from all the cross-sections are summed to calculate the performance scores.

The conceptual model (Figure 3.21) shows a grid with 6 nodes. The grid used in reality is much finer. For the finest grid, 101 nodes per cross-section are present. The result is that the navigability in every node is calculated 101 times. Every calculation is stored in a separate column in Python. For the largest grid (study case Monywa) this resulted in a *DataFrame* with well over 4 million entries. This data is stored and loaded in Excel .xlsx files of over 70 MB. This was a limitation for the minimum grid cell size. More efficient ways of storing the data are present (e.g., storing in .csv files), but have not been investigated. Excel files boast the advantage of user friendly access to the data outside of the Python environment.

In Figure 3.22 an example is given of how the performance indicators have been calculated near the study case of Kalewa.

3.8.3. Axi-symmetric model reliability indicators

It was hypothesised that the axi-symmetric model works not as good for areas where the channel stability and/or curvature is low. This hypothesis has to be checked. In this section the approach to do this is covered.

When the axi-symmetric model (partly) fails, this is expressed by a calculated *safety score* lower than one. The safety score has been calculated for every cross-section. Every cross-section also a value for the river *stability*

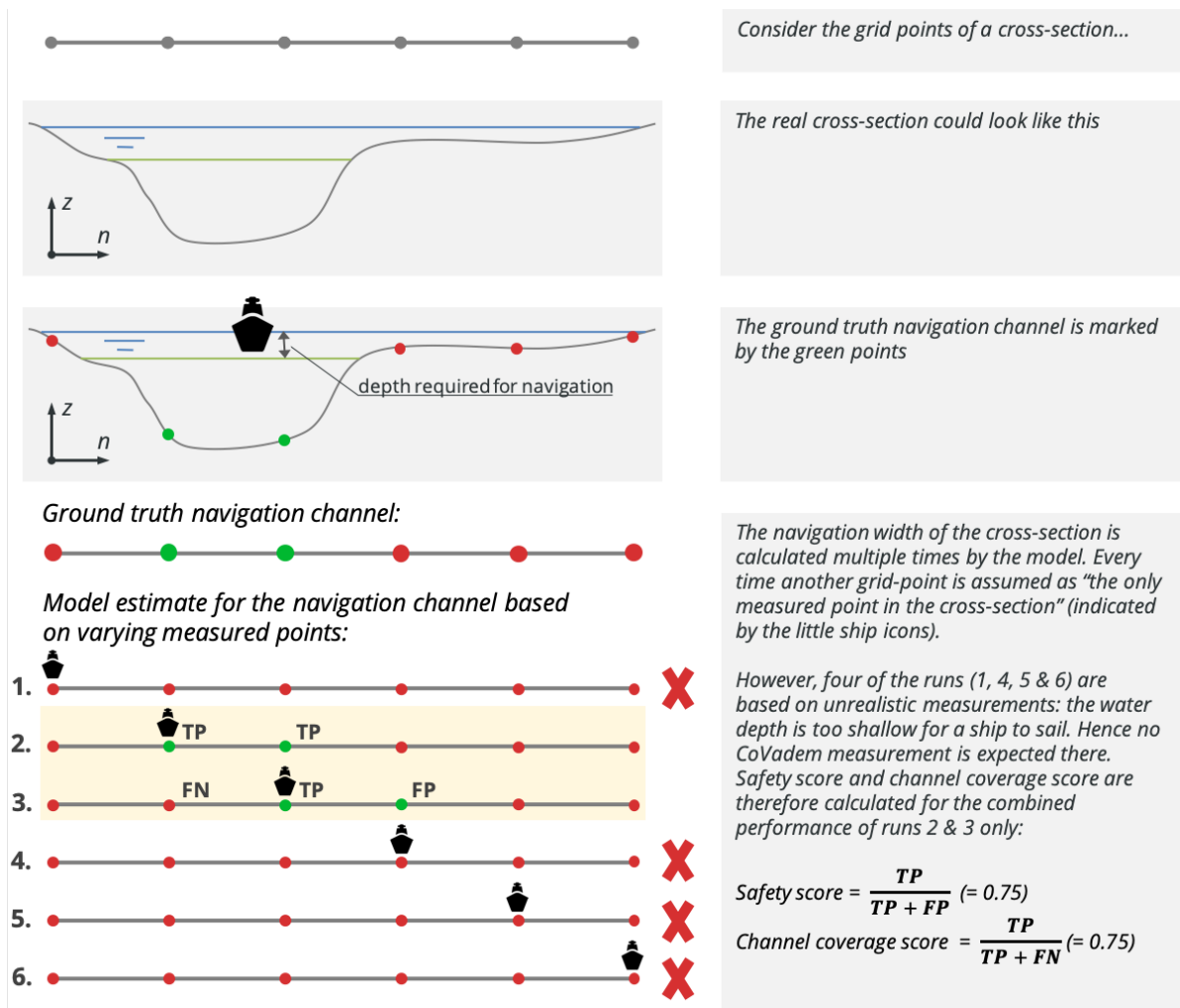


Figure 3.21: Method to calculate the weighted performance score for different measured point locations. TP, FP and FN are short for True Positive, False Positive and False Negative respectively



Figure 3.22: Performance indicators for a stretch of the river near Kalewa. Calibration factor $a = 5$, bank full water level = +8.0 m.

score (§3.5.4) and the river *curvature ratio* (§3.5.5) was calculated.

Approach qualitative validation

The qualitative analysis aims to answer the question for what types of axi-symmetric model failure the indicators are suitable. In order to do this, the areas where the axi-symmetric model fails are discussed including the presumed reason for failure. This information is analytically compared with the curvature and channel stability.

Approach quantitative validation

The intention of the *proposed method* is to only apply the axi-symmetric solution for cross-sections that satisfy with some minimum threshold values for the curvature and/or channel stability. In the quantitative analysis the influence from using thresholds before the axi-symmetric model is applied is investigated.

A good indicator for model reliability has a positive effect on the reliability. This is the first criterion on which the indicators are evaluated: how well is the indicator able to improve the axi-symmetric model reliability (the **safety score**). A more reliable model means more reliable information about the navigable area.

A good indicator for areas where the axi-symmetric fails is preferably also specific. Ideally it *only* indicates areas where the model fails. This the other criterion on which the indicators are evaluated: what percentage of the cross-sections satisfy with the threshold (the **applicability**). If the threshold is very strict, only a small fraction of the cross-sections remain where the axi-symmetric solution can benefit for navigation.

In the quantitative analysis varying thresholds are investigated. They are evaluated on their effect on the model reliability (safety score) and on the applicability.

4

Results and evaluation

The previous two chapters discussed the overall methodology and the implementation. In this chapter the earlier discussed steps are applied on study cases. The soil-model and axi-symmetric model are evaluated based on the performance indicators: *safety score*, *channel coverage score* and calculated channel width. The performance indicators are defined and calculated as described in the validation approach (§3.8). The estimated navigation channels are also qualitatively compared with the ground truth navigation channel.

Four study cases along the Chindwin were selected based on data availability. A grid was constructed based on typical ship dimensions. Such a grid is approximately equal to the grids used by CoVadem which makes further integration easy. All data is presented in meters related to a local reference height.

Section 4.1 discusses and interprets the results of the study cases separately. In the following section (§4.2) the validity of using either the channel *curvature ratio* and/or the *channel stability score* as indicators for the reliability of the axi-symmetric model is checked. A summary of the results is given in §4.3. The chapter ends with a demonstration of how the two models can be utilised in combination with a stability score threshold.

4.1. Study cases

This section shows the results of the model performance for the study cases. For conciseness only three out of the four study cases are discussed in this chapter. The site specific results of the fourth, *Khamtee*, were moved to Appendix C.1. The results of the Khamtee study case were in line with the findings in the other cases. In the analysis of all data (§4.2 and §4.3) the results from *Khamtee* are included.

For the first study case (Htamanthi, §4.1.1) the axes of the graphs are explained a bit more extensively. After this section, what is plotted is deemed known to the reader and only the results are discussed.

The axi-symmetric model has one highly uncertain parameter, the calibration coefficient for the influence of helical flow a . This parameter influences the steepness of the slope in the transverse direction. The Kalewa study case was used to calibrate it (Appendix B.5) and a value of $a=5$ was selected and applied to all study cases. Choice for a was found to be a trade-off: more conservative parameters resulted in a smaller calculated channel width but a more reliable model. The selection is motivated but still rather arbitrary. Therefore a small sensitivity analysis took place to investigate the influence of the choice for calibration coefficient a on the model results (Appendix C.4).

In Table 4.1 the governing hydrographical parameters used by the axi-symmetric model are displayed. The Chézy roughness was estimated based on Dooren [2019]. The longitudinal slope is derived from SRTM data. The mean sediment grain size was selected based on expert consultation with Dr. ir. C. Sloff. The bank full water level was set equal to the water level during dominant discharge. Dune height and dune length calculation were based on the van Rijn classification (A.2, [van Rijn, 1984a]).

Table 4.1: Hydrographical parameters

	Variable	Unit	Khamtee	Htamanthi	Kalewa	Monywa
Chézy roughness	C	$[m^{1/2}/s]$	56	56	56	56
Longitudinal slope	i	$[m/m]$	1E-4	1E-4	1E-4	1E-4
Mean sediment size	D_{50}	$[m]$	450E-6	450E-6	450E-6	450E-6
Calibration coefficient	a	$[-]$	5	5	5	5
Bank full water level	z_{bank}	$[m]$	6.5	9.5	8.0	6.5
Dune height	h_{dune}	$[m]$	0.49	0.34	0.82	0.38
Dune length	l_{dune}	$[m]$	51	103	73	24
Mean flow velocity	\bar{u}	$[m/s]$	1.4	1.9	1.3	1.2

4.1.1. Study case - Htamanthi

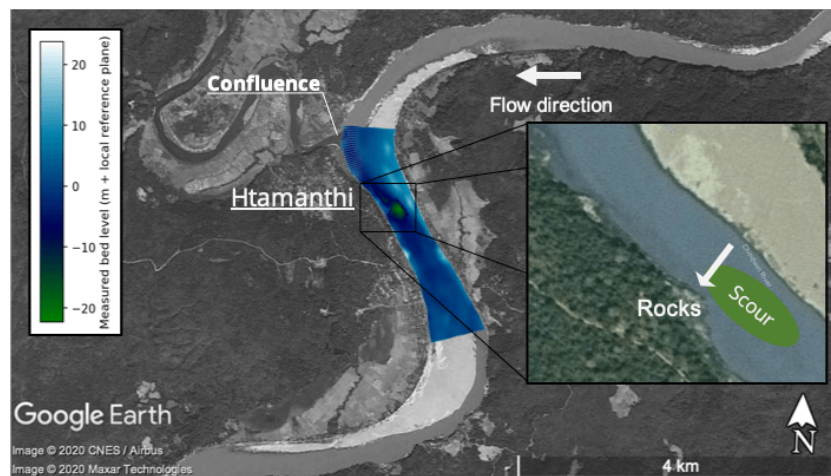


Figure 4.1: Overview of the Chindwin river near Htamanthi, including the bathymetry. In the data a deep scour hole can be observed, this is presumably due to forcing of the flow by rocks (zoom)

The study case of Htamanthi is positioned as the second most upstream of the four. Although the river has a mostly sandy bed, there is some natural hard forcing on the river. An overview of the river near Htamanthi, including the ground truth bathymetry is shown in Figure 4.1. A stretch of around 3 km was measured with single beam echosounders around June 28th 2016. Near the north a confluence is visible. How much the confluence influences the bathymetry is difficult to investigate because it takes place right at the start of the measured data. Around the center of the data, a large scour hole is visible (green tints). This scour hole is presumably due to forcing from the outer bend, where some rock formations are located (Figure 4.1, zoom). The rocks force the water inward, increasing flow velocities and causing scour.

The performance indicators were calculated in the way described in §3.8.2. In Figure 4.4 the *safety score* of the axi-symmetric model is plotted. The results for the other scores can be found in Appendix C.2. To illustrate the working of the model, a synthetic CoVadem ship track with the estimated navigable area is shown in Figure 4.2. The left image shows the available measured data, used by the models. The centre and right image display the calculated navigation channels (area within blue line). On the background also the true/ground truth navigation channel was plotted in order to compare the model estimate with reality.

The performance indicator were also calculated for the entire study case at once. For the soil-model a safety score of 1 (always safe) was found. The channel coverage score was 0.0533 (i.e., the calculated width is 5% of the real width of the channel). The calculated channel width in absolute numbers is 14.66 m. The channel coverage score and calculated channel width strongly depend on how deep the channel is. Around the scour hole, the estimated widths strongly increase (Figure 4.2, centre).

The axi-symmetric solution has a much wider calculated channel width (97.90 m) and channel coverage score

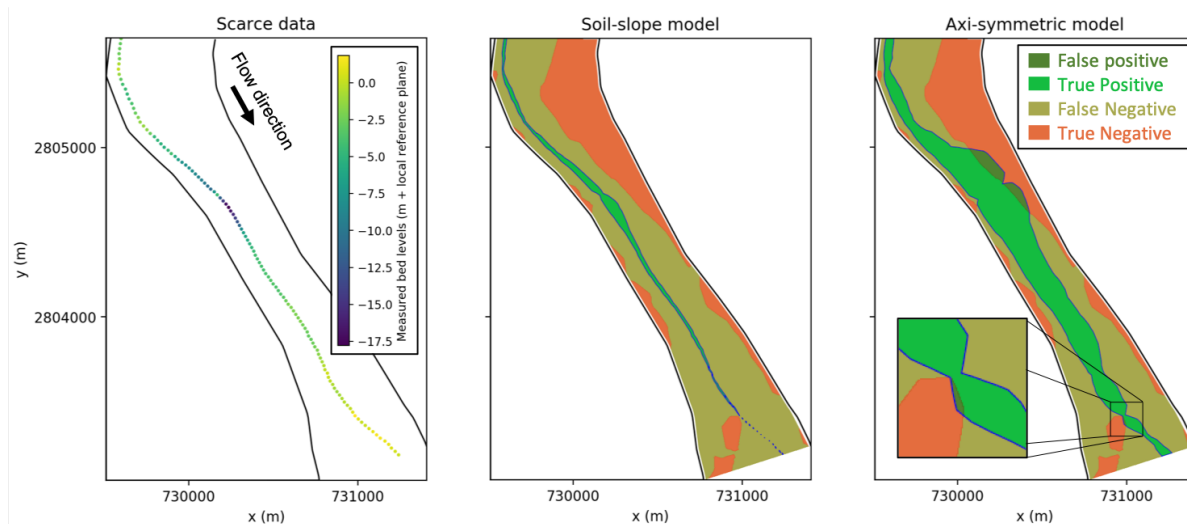


Figure 4.2: A scarce dataset forms the basis for the calculation (left). The centre image displays the navigable area estimate for the soil-model, the right image for the axi-symmetric model. The model estimate is the area within the blue line. On the background the ground truth navigation channel is plotted for comparison

(0.32). The axi-symmetric model fails near two areas (safety score < 1). In Figure 4.4 this is noted by the blue line that is lower than 1 from around 750 m - 1250 m and 2600 m - end. In Figure 4.2 (right) it is observed that the model estimate for the example track also fails near those areas (False Positives are generated). The first area is around the scour hole, the second near the southern end of the stretch. Near the scour hole the model fails presumably for two reasons:

1. The scarce available measurements near the scour hole show a very low-lying river bed (large water depth). The axi-symmetric model calculates the channel with a.o. based on the water depth. The large water depths around the scour hole result in a very wide calculated channel.
2. The inside/transverse slope is calculated based on the channel curvature. A larger curvature means a steeper slope. The channel curvature is low around the scour hole, therefore a relatively flat transverse slope is calculated while in reality the transverse slope is steep.

Near the southern end of the stretch we see another area where the model (sometimes) fails. Here we observe some braiding in the navigation channel. Apparently, higher order morphological processes have a larger influence on the shape of the bathymetry there. The axi-symmetric solution does not include these processes and hence it fails. The model however only appears to fail when the trackline is close to the sand banks (see Figure C.2, right, zoom).

The 10 year low-water water occurrence map for Htamanthi is displayed in Figure 4.3 (left). The channel stability score was calculated from this map, and is visualised in Figure 4.3 (right). A small dip in stability can be seen in the north. This is presumably under influence of the variable sediment input from the confluence with the small river there. Near the south also a decrease in the channel stability score is observed.

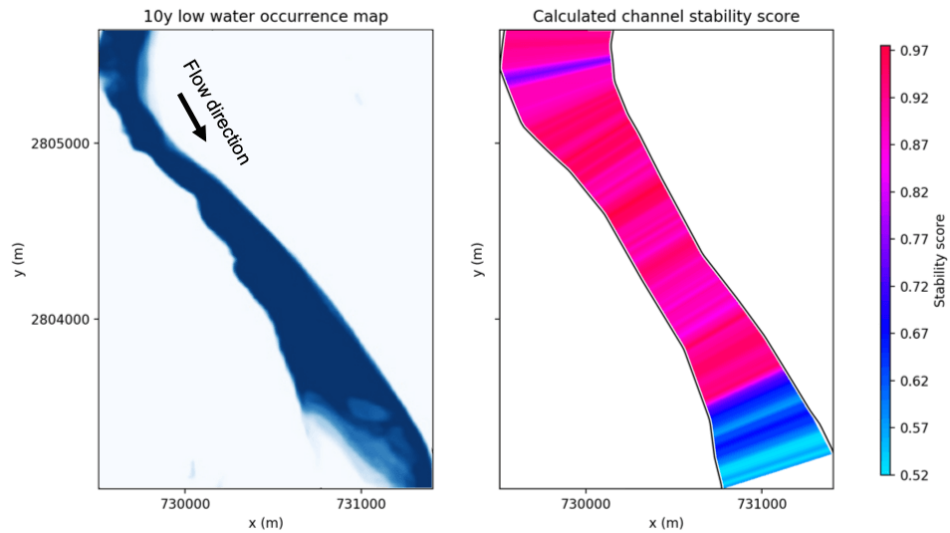


Figure 4.3: Left: the 10 year low-water water occurrence map. Right: the calculated stability score, measure for how stable the channel is locally (Htamanthi study case)

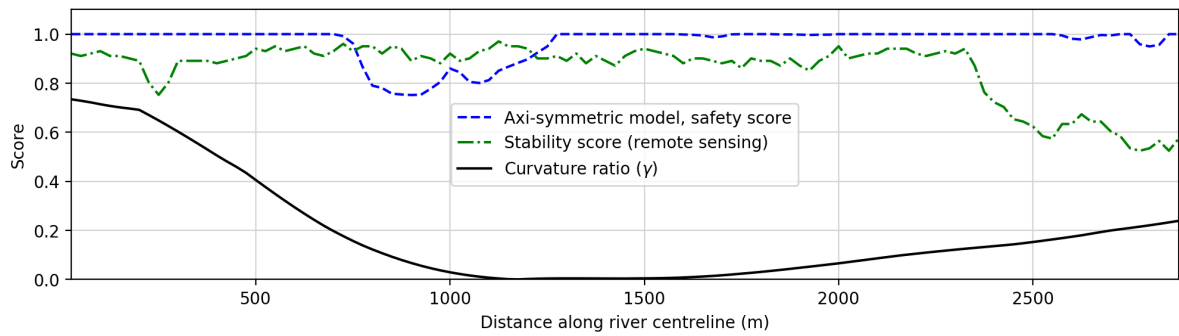


Figure 4.4: The safety score of the axi-symmetric model, measure for the reliability of the model, along the centreline of the Htamanthi study case. Moreover the channel stability score (remote sensing) and the curvature ratio are plotted

4.1.2. Study case - Kalewa

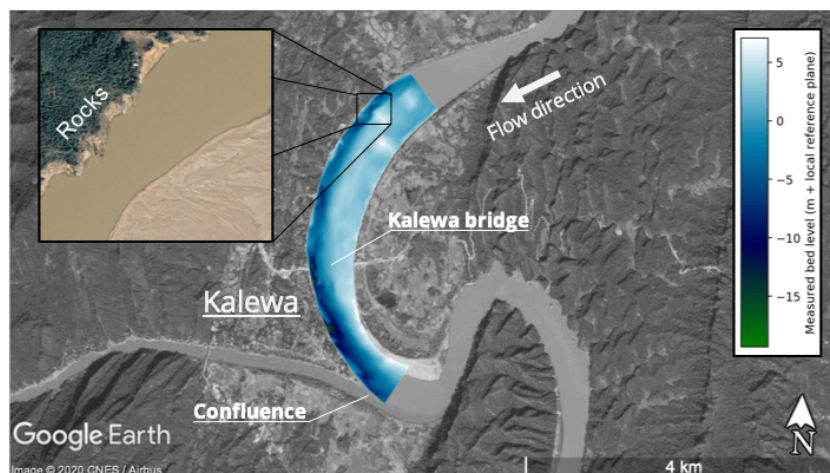


Figure 4.5: Overview of the Chindwin river near Kalewa, including the ground truth bathymetry

Figure 4.5 shows an overview of the Kalewa study case. The available data covers a bend in the Chindwin. The bathymetry appears to roughly follow the shape one would expect with the axi-symmetric formula: a deeper outer bend a more shallow inner bend. Near the south a confluence with a smaller river can be observed. The large scale contours of the river near Kalewa are more or less fixed in place by mountain ranges. Finally we can also observe some scour near the Kalewa bridge induced by the bridge pillars.

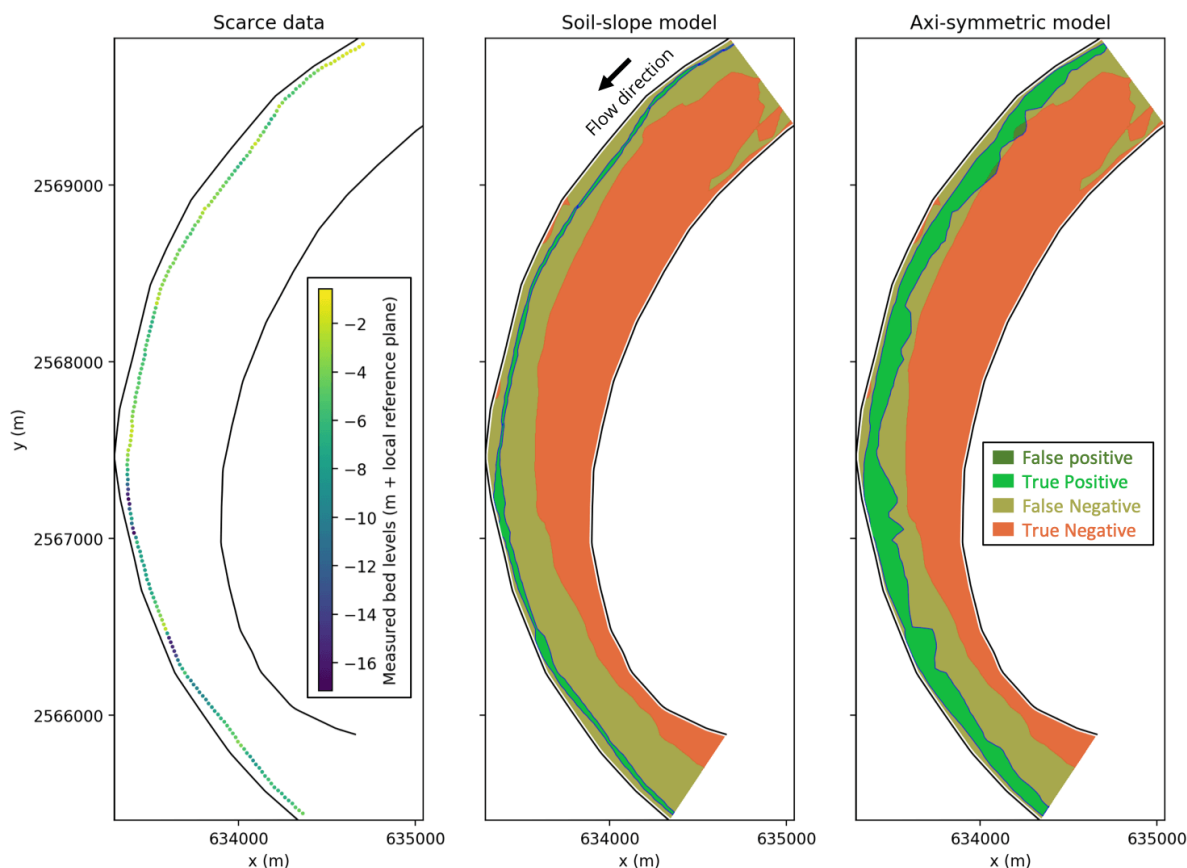


Figure 4.6: A scarce dataset forms the basis for the calculation (left). The centre image displays the estimated navigable area for the soil-model, the right image for the axi-symmetric model. The model estimate is the area within the blue line. On the background the ground truth navigation channel is plotted for comparison

In Figure 4.7 (left) the 10 year low-water water occurrence map is displayed. The water occurrence map shows a very stable low water channel. This is presumably due to the limited freedom of the river locally; The river path is fixed between mountains, and the curvature in the channel forces the river bathymetry in an (approximate) shape. The stability score for the Kalewa study case is the most constant from all the study cases. This is plotted visually in Figure 4.7 (right) and along the centreline in Figure 4.8 (green line).

The *safety score*, and *channel coverage score* for the two models have been calculated according to the validation method. The safety score for the axi-symmetric model is plotted in Figure 4.8 (blue), for the remaining scores refer to Appendix C.2. The soil-model showed results similar to the other study cases: it doesn't fail anywhere but it is very conservative.

The axi-symmetric model only shows one area near the beginning where the safety score is not 1 and where the model sometimes fails. This failure is also observed for the example track (Figure 4.6, right, False Positive area). What we observe around the area where the model fails is that a significant narrowing ($> 10\%$) of the river takes place due to some rock formations (see Figure 4.5, zoom). These rocks cause scour in their proximity, however not as severe as the Htamanthi scour hole.

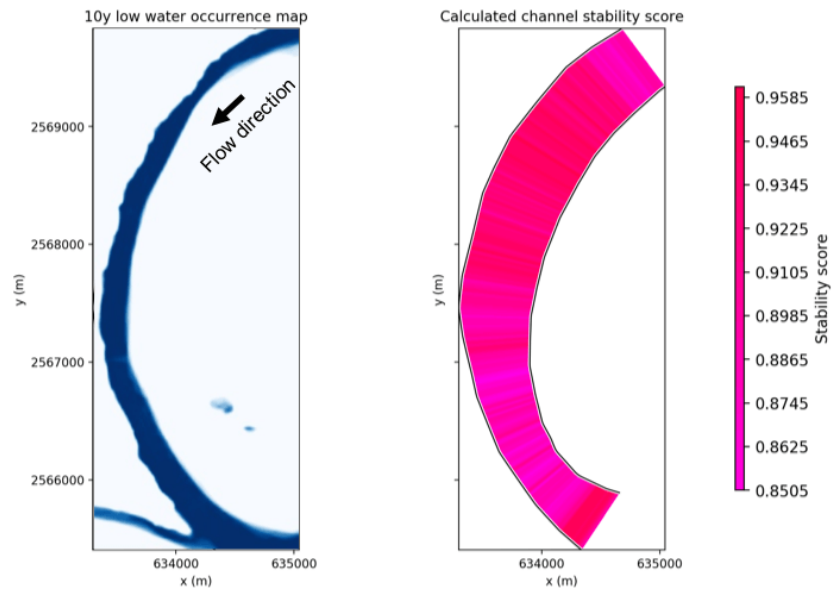


Figure 4.7: Left: the 10 year low-water water occurrence map. Right: the calculated stability score, measure for how stable the channel is locally (Kalewa study case)

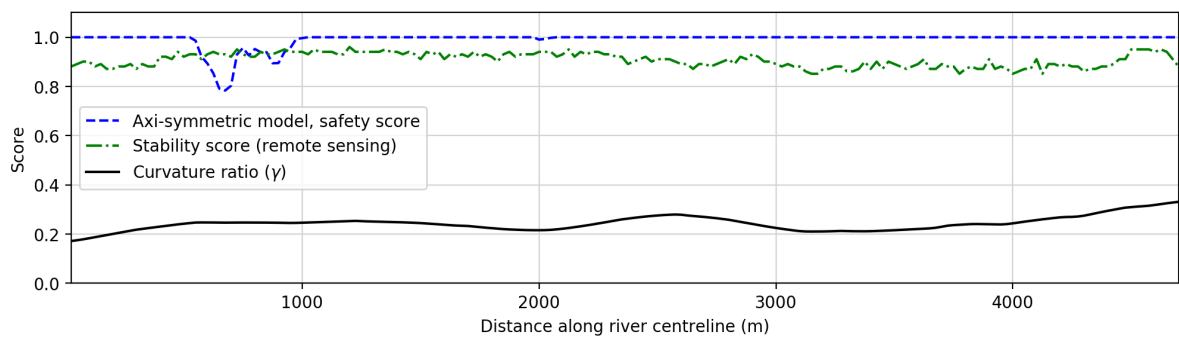


Figure 4.8: The safety score of the axi-symmetric model, measure for the reliability of the model, along the centreline of the Kalewa study case. Moreover the channel stability score (remote sensing) and the curvature ratio are plotted

4.1.3. Study case - Monywa

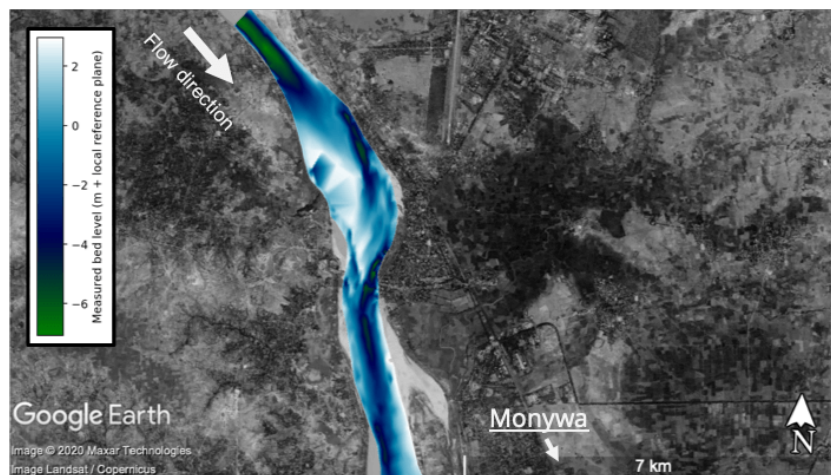


Figure 4.9: Overview of the Chindwin river near Monywa. The measured data is plotted in blue tints.

The most downstream study case is located close to the city of Monywa. At this location the river width is largest (> 1 km). An overview of the area and the ground truth bathymetry is given in Figure 4.9. The data shows a more or less single channel bathymetry near the north and south. Around the centre however the bathymetry is much more complex. Data was collected around November 21st 2016.

For the soil-model the results are the same as for the other study cases: conservative but reliable (see the summary of the results in Table 4.3. For the detailed graphs of the other performance scores, see Appendix C.2.

The axi-symmetric model performs well near the north and south of the study case. Around the centre however, sometimes the model fails. In Figure 4.12 this is indicated by the areas where the safety score drops below 1. The estimated navigable areas for an example CoVadem track are depicted in Figure 4.10. Note the dark green areas, representing False Positives. Every location where the model fails shows a combination of the following two problems:

1. Presence of river braids. Braids are not included in the axi-symmetric model.
2. Calculated channel curvature small or opposing observed direction. The axi-symmetric model performs reasonably well for single channels, as long as the curvature corresponds with what is observed in reality. Much of the models' reliability comes from a relatively conservative calculation for the inner slope (slope calibration factor (a) = 5.0). The inner slope is however also a function of the curvature. When the curvature approaches zero, so does the calculated transverse slope.

4.2. Results: curvature, channel stability and model performance

In this section we investigate whether the curvature ratio and/or the channel stability score can be used as an indicator for axi-symmetric model performance. Especially areas where the axi-symmetric model malfunctions (safety score < 1) are of interest. This section consists of a qualitative analysis and a quantitative analysis.

4.2.1. Qualitative analysis

In Table 4.2 the locations where the axi-symmetric model can fail (safety score < 1) are listed. For every location the presumed cause of failure is mentioned. *Braided* is mentioned as the presumed cause of failure when a location has navigable areas split off from each other by unnavigable ones. Low/wrong curvature is noted when the transverse slope that is observed in the validation data is significantly different from the calculated slope by the model. Per location an indication is given if the river curvature and channel stability

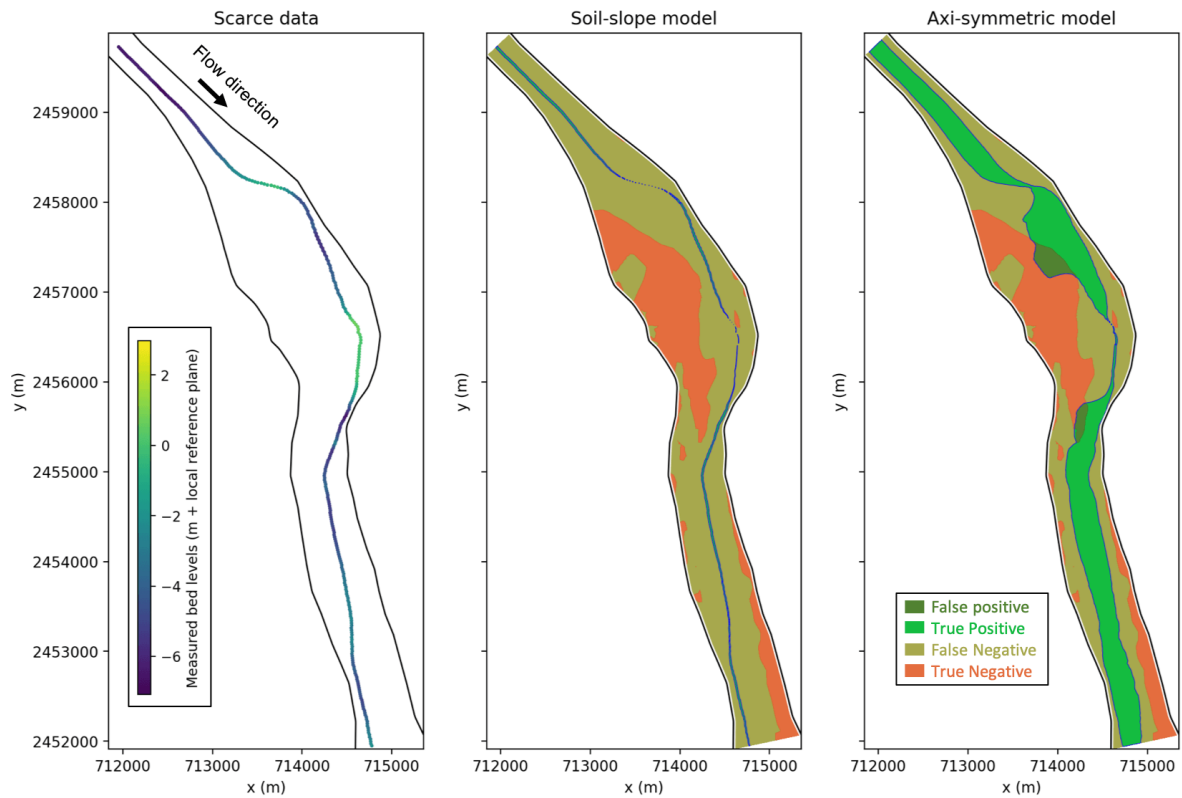


Figure 4.10: A scarce dataset forms the basis for the calculation (left). The centre image displays the navigable area estimate for the soil-model, the right image for the axi-symmetric model. The model estimate is the area within the blue line. On the background the ground truth navigation channel is plotted for comparison.

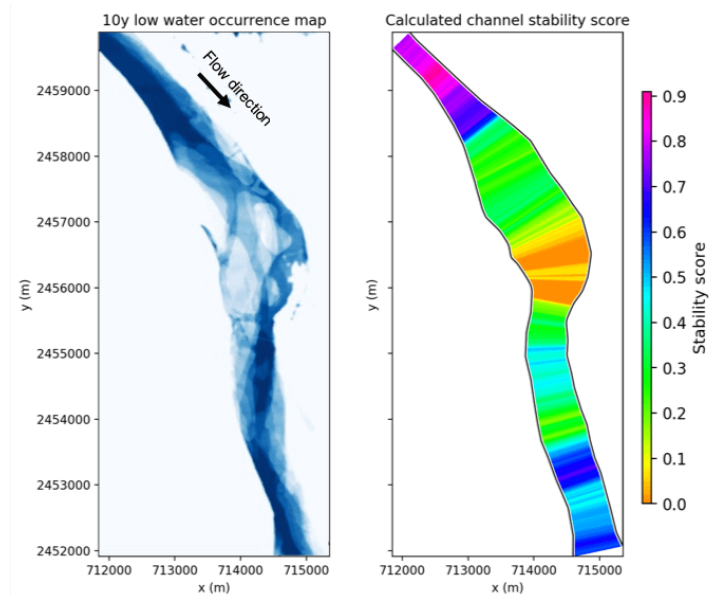


Figure 4.11: Left: the 10 year low-water water occurrence map. Right: the calculated stability score, measure for how stable the channel is locally (Monywa study case)

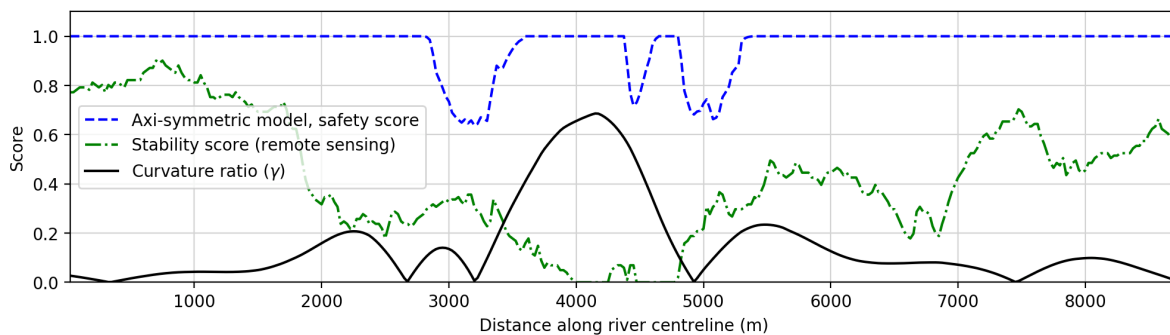


Figure 4.12: The safety score of the axi-symmetric model, measure for the reliability of the model, along the centreline of the Kalewa study case. Moreover the channel stability score (remote sensing) and the curvature ratio are plotted

are low. Curvature is considered low when the curvature ratio (γ) is smaller than around 0.15. The stability score is considered low when it is below around 0.60. For now the the values of 0.15 and 0.60 are just used as very rough indicators of whether or not we see a low channel curvature or stability. In the quantitative analysis these values are investigated. For some locations the failure of the axi-model appeared more often and was more sincere than for others. The relative contribution of each location to the total error (all study cases combined) is listed in the rightmost column.

Table 4.2: Summary of locations where the axi-symmetric model gave false navigation channel estimates (safety score < 1).

Location	Primary cause of model failure	Curvature ratio low? ($\gamma < 0.15$)	Stability score low? (< 0.60)	Relative contribution (total = 100%)
Khamtee #1	braided + low/wrong curvature	yes	yes	3.7%
Htamanthi #1	hard structure	partially	no	18.7%
Htamanthi #2	braided	no	yes	1.3%
Kalewa #1	hard structure	no	no	8.9%
Monywa #1	braided + low/wrong curvature	yes	yes	33.8%
Monywa #2	braided + low/wrong curvature	partially	yes	33.6%

Table 4.2 shows that for the four locations where braiding plays a role, this is also indicated with a low stability score. For three out of the four locations where braiding plays a role, river curvature is low as well. This suggests that braiding, a low curvature and a low channel stability score are correlated. Two locations where the model fails, *Htamanthi #1* and *Kalewa #1*, do not coincide with a low channel stability score. In both cases model failure is presumably due to natural hard structures. An explanation for this could be the following: The hard structures force the bathymetry in a different shape compared to what the axi-symmetric model calculates. Because of this, the axi-symmetric model gives wrong estimates. However, because the forcing from the hard structures is very constant, this is not reflected in a dynamic channel. Hence the channel appears stable and has a high stability score.

4.2.2. Quantitative analysis

In this section the ability of the channel curvature and/or channel stability to indicate areas where the axi-symmetric model fails is investigated quantitatively. For the quantitative analysis all data from all the study cases was piled and investigated as one.

This paragraph is vital for understanding all plots in this section. The quantitative analysis revolves all around usage of **thresholds**. Thresholds are requirements that must be met (per cross-section) before the axi-symmetric model is applied there. A very high threshold for example, will result in a small percentage of cross-sections that satisfy with this threshold. The percentage of cross-sections that satisfy with a threshold is called the *applicability*. A lower *applicability* means that for a smaller percentage of the river stretch the axi-symmetric model can be used. Finally there is the *safety score*. The *safety score* in this section refers to the safety score

calculated over all cross-sections that satisfy with the threshold. To highlight that these specific terms are referenced, *applicability* and *safety score* are printed in italics in this section.

In Figure 4.13 (upper left) the stability score threshold is plotted against the *safety score*. In Figure 4.13 (upper right) the stability score threshold is plotted against the *applicability*. A threshold of 0 corresponds with no threshold (i.e., all cross-sections qualify, *applicability* is 100%). The graph shows that application of a stability score threshold is initially beneficial (*safety score* goes up). However, near the right hand side of the graph the line plummets. This is almost completely attributed to the scour hole (Htamanthi #1) where the model fails, but where the channel stability score is actually among the highest of all study cases. The reason the line drops can be explained as follows:

1. An increase in stability score threshold decreases the amount of cross-sections over which the *safety score* is calculated.
2. The stability score near the Htamanthi scour hole is very high. Therefore, despite the fact that the stability score threshold increases, all the cross-sections near that area still meet the threshold.
3. The amount of cross-sections over which the *safety score* is calculated decreases, while the amount of cross-section where the model fails stay the same. Hence the portion where the model is correct decreases and the calculated *safety score* goes down.

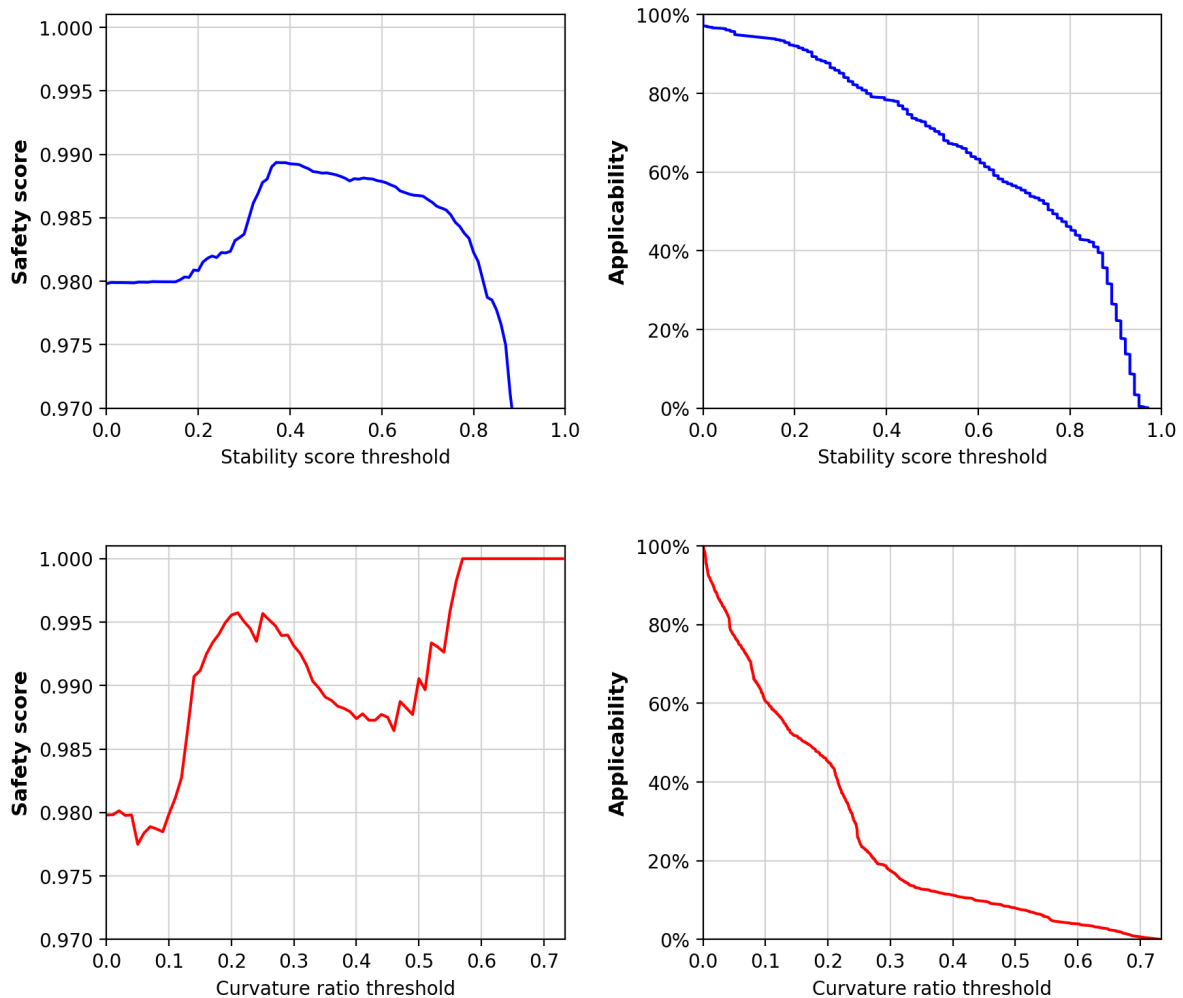


Figure 4.13: Usage of a **stability score threshold** plotted against the *safety score* (upper left) and *applicability* (upper right). The bottom figures display the same for a **curvature ratio threshold**

The bottom graphs in Figure 4.13 show the relation of applying a curvature ratio against the effect it has on

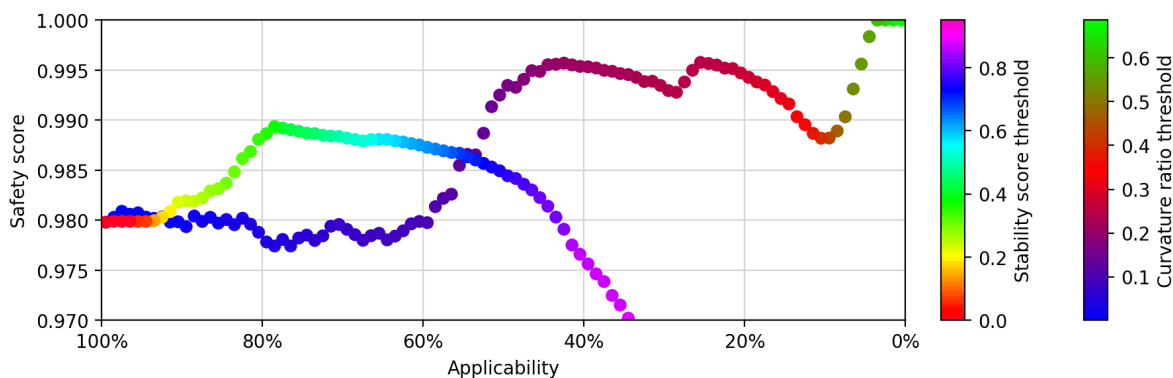


Figure 4.14: The *safety score* and *applicability* plotted as a function of the stability score threshold (rainbow colours) and curvature ratio threshold.

the *safety score* and *applicability* respectively. The results show that application of almost any curvature ratio threshold is beneficial to the axi-symmetric model *safety score*. However, the *applicability* graph shows a steep decline. If e.g., a curvature threshold of $\gamma = 0.2$ is picked, the *applicability* already drops below 50%.

In Figure 4.14 all the information from Figure 4.13 is combined in a single plot. For this plot both *applicability* and *safety score* are plotted as a function of the stability score threshold (rainbow colours) and curvature ratio threshold. The graph shows that initially the stability score threshold is much more efficient in increasing the *safety score*. For the study cases it is observed that with an *applicability* of still 80%, the amount of False Positives is almost cut in half (*safety score* goes from .98 to around .99). For the study cases, application of a curvature ratio threshold initially has a limited effect on the *safety score*. This is noted by the more or less horizontal line. However, when a curvature ratio threshold of around .2 is used, application of a curvature threshold outperforms the stability score threshold.

The axi-symmetric model can fail for various causes. Some causes show a correlation with a low channel stability score, and some not. Especially when the model fails due to forcing by hard structures this is not indicated by a low stability score. In Figure 4.15 the same is plotted as Figure 4.14, but this time the cross-sections near the Htamanthi scour hole have been removed. In this adjusted graph, application of a stability score threshold can improve model performance significantly. The stability score threshold outperforms the curvature threshold for almost any threshold.

It should be noted that removing locations where the model fails is somewhat ambiguous: removal of the data is carried out with hindsight of the model performance. However, methods can be thought of that can identify areas like the Htamanthi scour hole. It is highly recommended to further investigate possibilities to do so. A few options are discussed in the recommendations (§6.2.2).

One should note the following when interpreting the results: In total just over 20 km of river has been investigated. From the 20 km, 6 locations were found where the axi-symmetric model fails. The ability of the channel curvature and stability score as indicators for axi-symmetric model failure is entirely (!) based on their ability to locate those 6 locations. Therefore the found 'optimum' values for the stability and/or curvature threshold should be treated with great care. However, the results do indeed support the hypothesis that curvature and channel stability can serve as indicators for axi-symmetric model reliability.

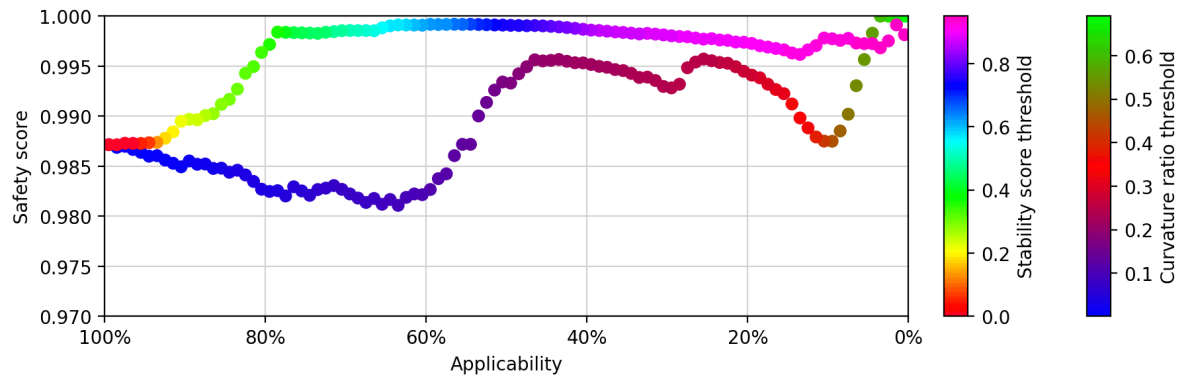


Figure 4.15: Similar to Figure 4.14. However, this time some cross-sections near the Htamanthi scour hole have been removed.

4.3. Summary of the results

Table 4.3: Summary of the performance indicators

		All sites	Khamtee	Htamanthi	Kalewa	Monywa
Cross-sections	[-]	812	160	115	188	349
Length along centreline	[m]	20,300	4,000	2,875	4,700	8,725
Soil-model, channel width	[m]	12.36	9.73	14.66	15.02	11.39
Axi-symmetric model, channel width	[m]	96.25	63.79	97.90	68.49	125.54
Soil-model, channel coverage score	[-]	0.0375	0.0355	0.0533	0.0602	0.0235
Axi-model, channel coverage score	[-]	0.2865	0.2285	0.3194	0.2741	0.2426
Soil-model, safety score	[-]	1.0000	1.0000	1.0000	1.0000	1.0000
Axi-symmetric model, safety score	[-]	0.9809	0.9959	0.9673	0.9911	0.9663

Table 4.3 shows the performance indicators from all sites combined.

The soil-model is found to be very robust. In the data no situations occur where the model gives wrong channel estimates (False Positives). The calculated channel width is on average 12.36 m. The calculated width is a function of the water depth. With a larger water depth the calculated channel width increases linearly. If no model were to be used, every CoVadem ship calculates a navigation channel as thick as the width of the ship. The grid was sized based on ship dimensions, the average width is 6.02 meter. From that perspective, the soil-model adds on average approximately one extra ship width (or one grid cell) to the calculated channel.

The axi-symmetric model is much less conservative compared to the soil-model. For the available study cases, the average calculated channel width was around 96 m. Around 98% (safety score = 0.98) of the calculated navigable area was calculated correctly. The axi-symmetric model requires some calibration which took place for the Kalewa study case. Calibration is found to be a trade-off between calculated channel width and model reliability (see §B.5).

Both channel curvature ratio and channel stability score appear to be correlated with the safety score of the axi-symmetric model. Application of a stability score threshold appears to be more efficient than a curvature threshold for detecting most types of areas where the model fails. However, the axi-symmetric model can fail for various reasons. When model failure is due to forcing by hard structures, no correlation with a low channel stability score is observed.

4.4. Utilisation example

In this section an example is given of how the *proposed method* (§3.1) can be utilised on a real case. Consider the river near Khamtee (Figure 4.16, left). Assume that there is one CoVadem ship track with bed level data (Figure 4.16, right). If multiple tracks are present the procedure for one track can be repeated.

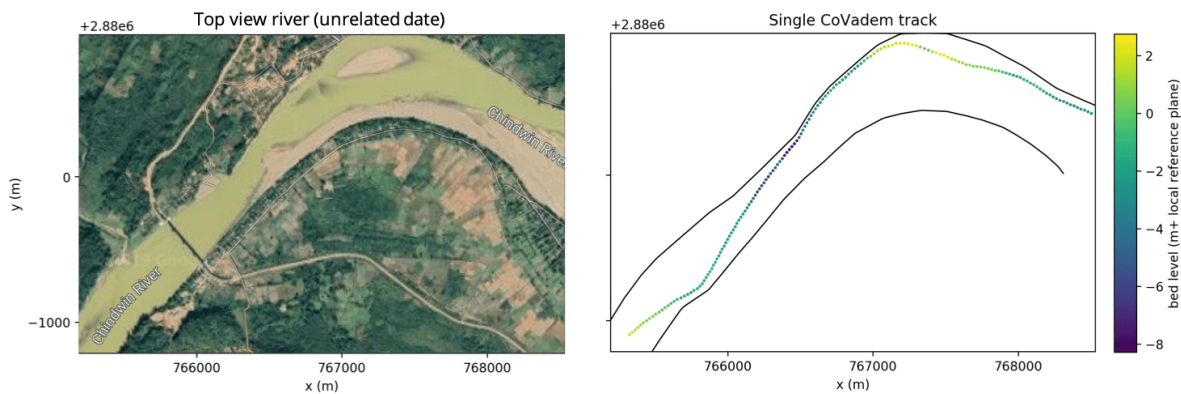


Figure 4.16: Left: true colour image near Khantee (taken at an unrelated date to sampling date). Right: an arbitrary CoVadem track containing scarce data

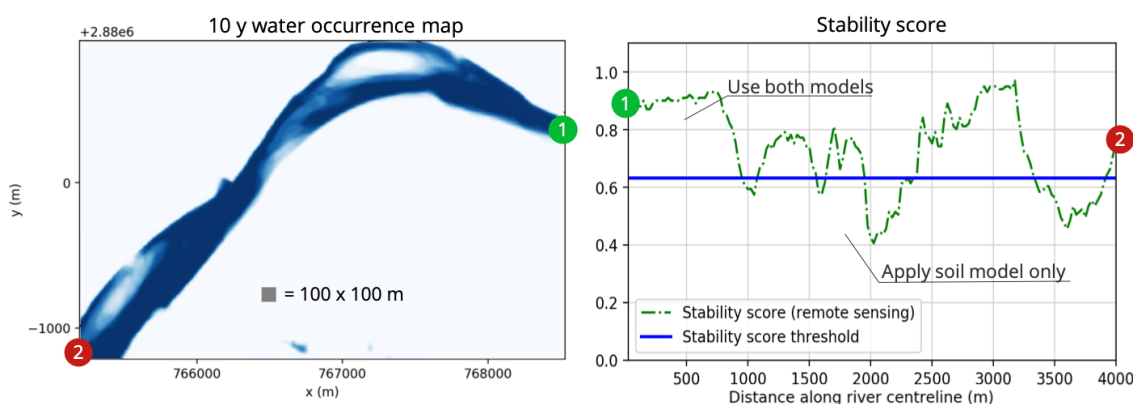


Figure 4.17: Left: 10 years of satellite images taken during march and april are combined to retrieve a *water occurrence* image (\$3.5). Right: calculation of the *stability score* along the investigated river stretch. An (arbitrary) threshold of 0.63 was used to determine where the axi-symmetric model may be applied.

Assume that a the user wishes to use the channel stability score (from remote sensing) as the indicator of where to use the axi-symmetric model and where not. Moreover assume that a threshold of 0.63 for the channel stability score is picked by this user. In Figure 4.17 (left) the 10 y low-water water occurrence map is displayed. Based on this map, the stability score is calculated per cross-section. This information is plotted along the centreline together with the threshold of 0.63 in Figure 4.17 (right).

Whenever the channel stability score is above the threshold of 0.63, the axi-symmetric solution may be applied. This is illustrated in Figure 4.18 (left). The soil-model can always be applied everywhere. In Figure 4.18 (right) the combined result of the soil-model and the axi-symmetric model is illustrated. The thin inner blue line represents the navigable area estimate of the soil-model, this model is applied everywhere. The bigger green areas represent the navigable area estimate of the axi-symmetric model, only applied for the areas of the river that are considered stable enough.

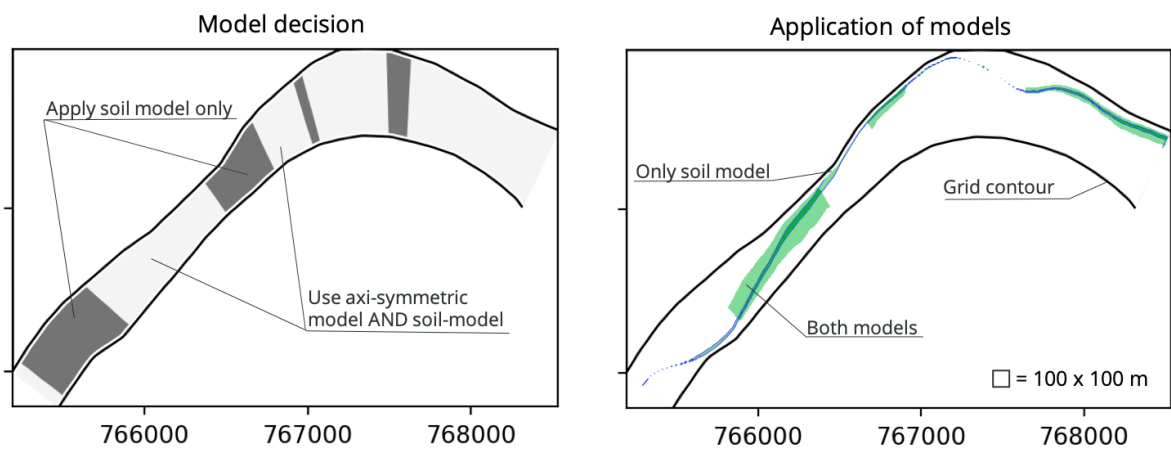


Figure 4.18: The left figure shows the locations where the axi-symmetric model may be applied, these are the cross-sections where the stability score is higher than 0.63. The right figure shows the combined result of both models. The blue line represents the navigable area as calculated by the soil-model. The green area the navigable area as estimated by the axi-symmetric model

5

Discussion

This chapter covers the interpretation of the results found in Chapter 4. The chapter starts with an analysis of how the results from this research agree or contrast with previous studies. This is followed by a section acknowledging the limitations to the study.

5.1. Related studies

Beltman [2016] investigated usage of the D-RATIN tool to indicate areas where dredging was necessary. The D-RATIN tool and the axi-symmetric model in this thesis share many similarities: both use the axi-symmetric solution and are meant for data scarce environments. The results of Beltman [2016] were not too promising. The study found that the method was too coarse to effectively indicate areas where dredging was necessary. The findings are in contrast with the results of this thesis: application of the axi-symmetric model yields promising results. The difference in results can presumably be explained from two differences in the research question/approach:

1. Beltman [2016] aimed to estimate areas where navigation *is not* possible (where dredging was necessary). This research does the opposite and aimed to estimate areas where navigation *is* possible. The latter approach boasts the advantage that certain measures can be taken that make the models more robust.
2. The method used by Beltman [2016] calculates the river bathymetry first and interpolates with available measurements later. The axi-symmetric model in this thesis uses the available measurements as the basis of the model. Both Zervakis and Beltman find that a accuracy of a bathymetry constructed with the D-RATIN tool is highly dependant on the hydrographical parameters. However, even when the hydrographical parameters can be calibrated from the validation data, they find that errors within study cases can be significant. This research on the other hand fits the axi-symmetric solution through the measured data. This is a much more data driven approach where it is as if the axi-symmetric model is calibrated for every cross-section. This might not be a good idea when the main goal is to approximate the real bathymetry as good as possible. But in the case an estimate of the navigable area is the requirement, this approach seems to yield better results.

A possible explanation for the surprisingly good results of the axi-symmetric model could lie in the fact that the model is rather conservative; Based on the literature a choice was made to include the presence of the river banks, sand dunes and transverse slope in the model in a reasoned, but conservative way. As a result the axi-symmetric solution works decently for some areas that do not follow the archetypal axi-symmetric cross-section shape. These results suggest that the axi-symmetric model, through (conservative) inclusion of physical processes accounted for, corrects for physical processes unaccounted for. On one hand one could argue that that is not a valid scientific approach. On the other hand the results suggest that apparently the most important morphological processes are indeed accounted for. This is especially observed in the model estimate of the (generally) more shallow inner banks compared to the outer ones. Moreover lies the power of the model in its simplicity: by using some basic formulae and hydrographical parameters a decent result

can be retrieved. This limits computational time and opens the door for large scale implementation. In addition to this, when the research question is considered, one could state that it shouldn't necessarily be the aim of this thesis to include every physical process as extensive as possible. Proper inclusion of some of the dominant processes seems to suffice.

Application range of the axi-symmetric solution

Crosato [2008] states that the axi-symmetric solution can be applied for mildly curved ($\gamma \approx 0.1$), meandering, alluvial rivers with an infinitely long bends. Zervakis [2015] found evidence to suggest that the axi-symmetric solution can be applied on a wider range of rivers. His suggestions are supported in this research: none of the study cases (fully) complied with the requirements from Crosato, yet the axi-symmetric model results are promising (for parts of the river).

Assumptions of the soil-model

Koloski et al. [1989] states that the slope for sand grains is at maximum around 30 degrees. The results from the soil-model, that uses this 30 degrees slope, support this. However, the soil-model is so robust that the suggestion is raised that the 30 degrees slope is too conservative. This is in line with consultation with Dr. ir. C. Sloff, who stated that a 30 degree slope is normally only reached near eroding banks.

5.2. Study limitations

This section discusses certain aspects of how this study was conducted that can lead to differences between the results from this study compared to application to a real case.

Coarseness of the validation data

In order to validate the soil-model and the axi-symmetric model, single beam echo sounder data was used. However, the (unstructured) measurements are quite coarse (approx. 80x30 m). The available data catches the large scale features of the morphology, but smaller scale features unfortunately not. It is not likely that the results of the soil-model would be affected much by finer validation data: the model seems so conservative/stable that it likely suffices anyhow. For the axi-symmetric model it is suggested that the model is not affected much as long as areas are investigated where primary flow and helical flow play a dominant role. It is suggested that for areas where the water depth is close to critical for navigation, validation with finer data could somewhat differ from the current results.

Time of validation data collection

Much of the available echo sounder data was collected during the monsoon period. During the monsoon, there is no benefit in using the soil or the axi-symmetric model since ships can simply sail everywhere. Therefore the water levels were artificially lowered. However, the measured echo sounder data is still from the monsoon bathymetry, which can be significantly different from the bathymetry that is encountered during low water. This is likely to affect the results in two ways:

- The bathymetry during the low water is generally more flat and the water depths are likely to be smaller [Pfeiffer et al., 2019]. The calculated channel widths are a function of the water depth. Therefore the calculated channel widths (the benefit of this study for navigation) will presumably be smaller for both the soil-model and the axi-symmetric model when applied to a real low-water case. A (very rough) back of the envelop calculation suggests that, in the case that the water depth is 50 cm more than the depth required for navigation, the axi-symmetric model calculates a navigable width in the order of 30-40 meters, still a significant improvement. The added benefit of using the conservative soil-model with such depths is negligible.
- An important parameter of the axi-symmetric model is the channel curvature. The channel curvature is calculated from the curvature of the grid. The grid was constructed based on the bank full (top view) alignment of the river. During the monsoon the curvature of the flow generally follows the curvature of the grid. When river discharges drop, the river no longer covers the same (top view) extent as the monsoon river. In some situations the curvature of the low-water flow significantly starts to deviate from the curvature of the bank full river (imagine a straight channel with alternating sand bars). This can jeopardise the reliability of the axi-symmetric model. As a positive note however, it is suggested that at the areas where such effects take place, the channel stability score (remote sensing) will also be lower. Hence, if a stability score threshold is applied, the axi-symmetric solution will not be applied for those areas.

6

Conclusions & Recommendations

6.1. Conclusions

This section commences with the conclusions about the sub research questions, followed by the main research question.

1. ***What are the challenges for navigable area estimates when using CoVadem ship track data?***

This question has been addressed in §2.1. In summary four challenges can be identified that need to be addressed in order to change CoVadem under keel clearance (UKC) data into reliable information about the navigable area around the data:

- I Transforming UKC measurements into water depth data
- II Estimating/forecasting water levels
- III Morphodynamics
- IV Spatial data scarcity

The uncertainties from challenge (I) and (II) can be minimised through calibration and hydrodynamic modelling. Morphodynamics (III) are currently not included by CoVadem nor by this research. The uncertainty due to morphodynamics depends on sediment transport and elapsed time. For the Chindwin pilot project, spatial data scarcity (IV) is important, especially in the direction perpendicular to the flow. This challenge can be overcome with additional knowledge/information about the morphology and formed the main challenge for this research.

2.a) ***How can a physics-based model provide more information about navigable areas?***

Knowledge about river physics can be used in a physics-based model to estimate navigable areas. Two analytical models have been developed that can estimate a navigable area around CoVadem data:

- The first model, the soil-model (§2.2.1, 3.6), calculates a conservative estimate of a navigable area around CoVadem data by assuming that the bed material is known and by assuming presence of the maximum (unfavourable) slope around measured data.
- The second model, the axi-symmetric model (§3.1, 3.7), combines CoVadem ship track data, the axi-symmetric solution (§2.2.2) and assumptions about river banks and sand dunes (A.2) to estimate a navigable area.

2.b) ***How can remote sensing provide more information about navigable areas?***

Alternative ways to use remote sensing to provide information about navigable areas have been explored in §2.3. A method was developed where remote sensing *indirectly* provides more information about navigable areas. Indirectly in the sense that remote sensing is used to improve the reliability of the axi-symmetric model. A measure for the local channel stability (the *stability score*) was developed, making use of 10 years of remote sensing imagery and a curvilinear grid (§3.5.4). If the axi-symmetric

model is only applied to areas of the river where a (user-defined) minimum stability score is present, the overall reliability of the axi-symmetric model goes up (§4.2).

3.a) ***How can the performance of a navigable area estimate be measured objectively?***

The performance of a navigable area estimate is determined by the size as well as the reliability of the estimate. To evaluate the size and the reliability of the estimate, two dimensionless performance indicators have been developed (§3.8.1). The first, the *channel coverage score*, is related to the width of the estimated navigable area. The second, the *safety score*, is related to the reliability of the estimate.

No real CoVadem data from the pilot project area was available for this thesis. Instead, synthetic CoVadem ship tracks were extracted from another dataset (§3.4.3). The alignment of the synthetic CoVadem tracks is arbitrary. The performance indicators are, however, calculated based on this subjective alignment. This is problematic for objective performance measuring. A method has therefore been developed that diminishes this problem by calculating the performance indicators over *every* possible location of a single synthetic CoVadem ship track (§3.8.2)

For the axi-symmetric model, the values of the performance indicators also depend on reasoned yet subjective model parameter decisions. To limit the subjectivity, the axi-symmetric model was calibrated for its most uncertain parameter (calibration coefficient a , §B.5). Moreover was the axi-symmetric model subjected to a sensitivity analysis (§C.4).

3.b) ***What is the performance of the proposed method in terms of answering the main research question?***

The *proposed method* (discussed in §3.1) consists of roughly of two parts. Part one are the physics-based models (soil-model and axi-symmetric model). Part two are the indicators for axi-symmetric model reliability (stability score and curvature). The proposed method has been tested on for study cases, located along the Chindwin, following the objective performance measuring approached discussed above. First the conclusions about the two models are listed, followed by the conclusions about the reliability indicators.

The soil-model (§2.2.1, 3.14) is very robust but has a limited added value for navigation. The average calculated channel width calculated from one CoVadem track is around 12 m (§4.3). The estimated channel width increases linearly with the water depth (§2.2.1). For areas where the water depth is close to the depth required for navigation, the benefit of the model is negligible. There is potential room for model improvement, this is discussed in §6.2.2.

The axi-symmetric model is less robust but has a much higher added value for navigation. An average channel width of around 96 m was calculated. On average 98% of the estimated navigable area was calculated correctly. However, the values for channel width and reliability depend on the model calibration (§B.5). A critical analysis of the locations where the model fails found that a combination of the following three causes were present: braids, low curvature and/or forcing from hard structures (§4.1, 4.2).

About the reliability indicators can be concluded that the results support both the hypotheses that channel curvature and/or channel stability are able to improve the reliability of the axi-symmetric model. The reliability of the axi-symmetric model can be significantly improved when it is combined with either a curvature or channel stability threshold. The channel stability appears to be the most precise indicator for axi-symmetric model failure, except when this failure is due to scour from forcing by hard structures. Using the curvature ratio as an indicator appears to be a more robust method (is able to capture more locations with model failure) but at a larger expense of the applicability.

Finally, the main research question is discussed:

"How can additional knowledge of river morphology improve the navigable area estimate around CoVadem ship track data in scarce data environments?"

In conclusion the answer to the research question lies in application of the two physics based models (§3.1, utilised in §4.4) in combination with the two reliability indicators (§3.5). The first model, the soil-model, using the maximum theoretical slope in the bed (§2.2.1, 3.6) is very robust but only has a limited added value

for the size of the navigable area estimate. The second model, the axi-symmetric model, is promising. An average navigable width estimate in the order of 100 m (based on a single measurement per cross-section) was found (§4.3).

It can also be concluded that the axi-symmetric model is not 100% reliable. For some areas it fails. Axi-symmetric model failure is observed for areas where braiding plays a role; where the observed curvature in the data is very different from the curvature that the model uses; and where forcing by hard structures influences the morphology significantly (§4.1, 4.3).

Two reliability indicators were developed that can successfully improve the reliability of the axi-symmetric model: the channel stability score (§3.5) and channel curvature ratio (§3.5.5). The indicators work by only applying the axi-symmetric model to areas where some threshold value for the reliability indicator is met.

The channel stability score, calculated from historic low-water satellite imagery (§2.3, 3.5, 4.1) can indicate most areas where the axi-symmetric model fails, except when failure is related to forcing by hard structures. The curvature ratio is a more robust reliability indicator for the axi-symmetric model. However, the curvature ratio is not a very precise indicator.

In general can be concluded that the navigable area estimate around CoVadem data can be improved by application of the proposed method from this research.

6.2. Recommendations

6.2.1. Recommendations for model use

A number of recommendations for use of the model for different users are listed.

For a tool developer that wishes to integrate the physics-based models into an interface, it is recommended to make a difference (e.g., with colours) between which model estimated which area of the river as navigable. In order of decreasing reliability:

1. (CoVadem) measured grid cells
2. Soil-model navigable area estimate
3. Axi-symmetric model navigable area estimate

The axi-symmetric model estimate should be treated as a 'highly probable' navigable area.

For a captain sailing the Chindwin based on the information provided by the models, the safest advice is to follow previous CoVadem tracks or the soil-model estimate whenever possible. The axi-symmetric model estimate can be used whenever e.g., passing with other ships is necessary as a reliable alternative.

For a developer that wishes to implement the axi-symmetric model but prefers a higher reliability of the model: the axi-symmetric model can be made more robust. Robustness can be improved by assuming higher/steeper banks, assuming larger sand dunes and/or a steeper transverse slope (calibration coefficient a) in the model. Note that increasing the transverse slope only is not the answer to all failure types observed with the axi-symmetric model. The transverse slope only affects the navigable areas estimate of the inner bend in the model. Also, more conservative parameters will negatively affect the estimated navigable width.

When it comes to a selection of a axi-symmetric model reliability indicator it would be the authors' recommendation to use both the stability score and the curvature ratio. However, it is suggested to use them in a such a way that only one of the two thresholds has to be met in a cross-section before the axi-symmetric model is applied there. A subjective recommendation would be to use around 0.2 - 0.3 as a threshold for the curvature ratio and around 0.6 - 0.7 for the stability score threshold (based on the graphs in Appendix C.3). This is under the assumption that some model improvements will be made regarding dealing with areas with scour (discussed in the following section).

6.2.2. Recommendations for model improvement/implementation

Investigate the use of a less conservative slope for the soil-model

In the discussion the very conservative results of the soil-model were discussed. It is recommended to investigate using a slope lower than 30 degrees. Since steeper slopes can be expected mainly to occur near eroding banks, a simple solution can be to keep the 30 degrees slope for the outer grid cells while decreasing it for the central grid cells.

Investigate scour detection from the CoVadem signal

For the study case of Htamanthi an area is found where the axi-symmetric model fails (partly) due to the presence of a very deep scour hole. Because of the scour, the axi-symmetric model calculates a very wide navigation channel while this is not observed in reality. The CoVadem data is collected roughly along flow, therefore it should be possible to detect such scour holes from the along track signal. Methods can be applied to correct for scour holes (e.g., signal smoothing or outlier detection). In Figure 6.1 a potential solution with rolling window smoothing solution is depicted. The graph shows the along track bathymetry from some CoVadem ship, the signal after smoothing and after application of a MAX function on the original and smoothed signal. The MAX function is applied to make sure that very shallow areas are not treated as deeper by the model. The 'corrected' signal presumably gives more reliable navigable area estimates with the axi-symmetric model.

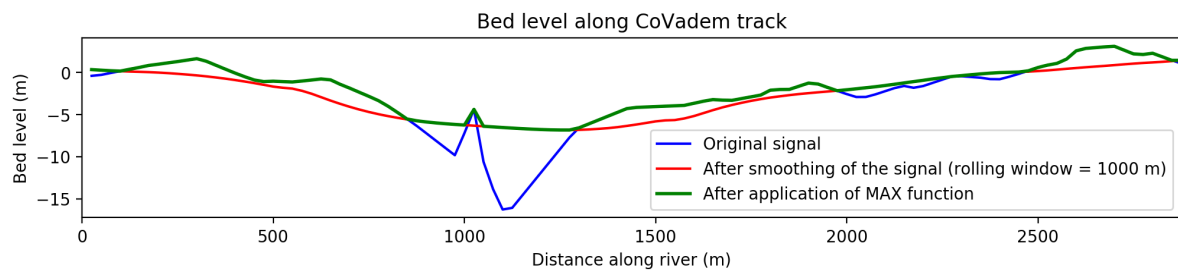


Figure 6.1: One of the cases where the axi-symmetric model fails, part of the failure is attributed to a large scour hole (for more info, see §4.1.1). Areas where scour is present can be detected and removed from the along track CoVadem signal. In this figure the effect of using rolling window smoothing with a window of 1000 m is plotted.

Compare the axi-symmetric model with remote sensing images to determine where the model is evidently wrong

Sometimes the estimated navigable area of the axi-symmetric model is not slightly wrong, but frankly way off. The Htamanthi scour hole is again a good example. For some axi-symmetric model runs the calculated navigation channel covers areas that are not only too shallow for navigation, but as a matter of fact not even covered by water at all. Dry-lying areas can be detected with remote sensing. This information can be combined with the calculated navigation channel. In case dry areas coincide with the calculated navigation channel, a decision can be made to not use the axi-symmetric model for that area.

Manual insertion of locations where the axi-symmetric model fails

The channel stability is a rather good indicator for axi-symmetric model performance for certain types of failure. When failure is related with forcing from hard structures, this is generally not indicated with a low channel stability. However, hard structures are always at the same location. A possible solution could be to manually include the locations where such failure occurs. However, the information that the model fails somewhere should come from e.g., grounded ships. Hence it is a rather reactive measure.

Investigate the possibilities of a dynamic grid

Sometimes axi-symmetric model failure happened because the model calculated the transverse slope opposite to the one observed in the data. This problem has been addressed in the results and discussion. A potential solution can lie in application of a dynamic grid. Such a grid can be based on the most recent river extent (from remote sensing) and updated regularly from more recent satellite imagery. A dynamic grid is likely to more accurately follow the real curvature of the flow and therewith the calculation of the transverse slope. Construction of a dynamic grid requires addressing a number of challenges (e.g., discretising the grid near river braids). Focus is here only on the possible consequences a dynamic grid has to application of the soil and axi-symmetric model. For application of the soil-model on a dynamic grid no problems are expected. For application of the axi-symmetric solution to a dynamic grid, two subjects require attention:

1. The current axi-symmetric model assumes that the outer grid cells have a bed level equal to the bank full water level. The bed level from the outer grid cells is used to determine the steepness of the river banks (a higher bed level leads to more conservative results). When a dynamic grid is used, the grid no longer covers the bank full extent of the river and therefore the bed level for the outer grid cells should be lower. It is recommended to set the bed level of the outer grid cells equal to the water level present during the moment the satellite image, used to construct the grid, was taken.
2. It is recommended to investigate how a dynamic grid influences the ability of the stability score to serve as an indicator for reliability of the axi-symmetric model. A dynamic grid requires recalculation of the stability scores every time a new grid is constructed. Two affairs require specific attention:
 - The pixel scale of the remote sensing images ranges from 10 m (*Sentinel-2*) to 30 m (*Landsat 7 & 8*). The Chindwin reduces to about 200 m in width at some critical sections. When *Sentinel-2* is used, this results in approximately 20 pixels of satellite data per cross-section to determine the stability score. However, *Sentinel-2* is only available from 2015 onward. For the older images the number of pixels per cross-section can be as low as 7.
 - The alignment of the low water channel within the larger channel can change over time. This affects the locally calculated stability score. An example is given in Figure 6.2 where the contours of two fictional low water channels are drawn on top of a *water occurrence* map. The calculated stability scores will deviate between the two. It should be investigated in what way this affects the ability of the stability score to serve as an indicator for axi-symmetric model reliability.

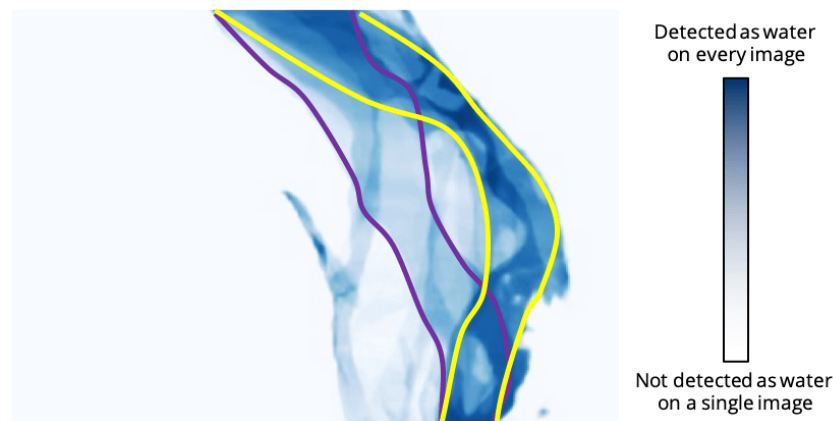


Figure 6.2: The 10 y *water occurrence* map near Monywa. Two hypothetical low-water channels are drawn. If a dynamic grid is used that changes with the low water channel, so do the calculated stability scores. How does this affect the ability of the stability score to indicate areas where the axi-symmetric model might fail?

Further investigate the use of two reliability indicators at the same time

For this research, the two reliability indicators are used separately to improve the axi-symmetric model performance. They can also be combined, which might yield better results (higher safety score and applicability) compared to a single threshold. See Appendix C.3 for some further information and a possible approach to use combined thresholds.

6.2.3. Recommendations for future work

Investigate the usage of a Computational Fluid Dynamics (CFD) model

In this study, two relatively simple models have been used. However, some areas were observed where a simple axi-symmetric solution does not suffice (e.g., areas with scour/braiding). A CFD model (such as *DELFT3D*) includes many more physical processes and can therefore potentially be used as a more sophisticated method to estimate navigable areas. It is recommended to investigate the application of a CFD model (and to compare the approach and results with this thesis).

Additional study cases

It is recommended to test the models for additional study cases. This way a better overview of the applicability

range of the developed models can be achieved. Both more braided and more meandering rivers could give a good idea of the full applicability. It is also interesting to investigate is how generic the applicability of the reliability indicators is. Moreover can this add to a stronger basis for the selected reliability indicator thresholds.

Bibliography

- ADB (2016). Myanmar transport sector policy note - River Transport. Technical report, Asian Development Bank.
- Allaby, M. (2008). *A dictionary of earth sciences*. Oxford University Press.
- Allen, G. H. and Pavelsky, T. M. (2018). Global extent of rivers and streams. *Science (New York, N.Y.)*, 361(6402):585–588.
- Attema, Y. and Hendriks, H. (2014). Delft3D model of the Ayeyarwady delta Myanmar. Technical report, Delft University of Technology.
- Aung, A. N. (2019). A study on private sector services in inland water cargo transport (Case Study: Yangon-Mandalay Cargo Transport). *Diss. Yangon University of Economics*.
- Beltman, M. (2016). Exploring the D-RATIN tool Studying inland navigation potential using a rapid assessment tool (internship report). Technical report, University of Twente.
- Birkett, C. M. and Beckley, B. (2010). Investigating the Performance of the Jason-2/OSTM Radar Altimeter over Lakes and Reservoirs. *Marine Geodesy*, 33(sup1):204–238.
- Bosboom, J. and Stive, M. J. (2013). *Coastal Dynamics I*. Delft Academic Press.
- Campbell, J. B. and Wynne., R. H. (2011). *Introduction to Remote Sensing FIFTH EDITION*.
- Casasent, D., Casasent, and D. (1978). *Optical data processing: Applications*, volume 23. Springer-Verlag, Berlin and New York.
- Chen, W. and Mied, R. P. (2013). River velocities from sequential multispectral remote sensing images. *Water Resources Research*, 49(6):3093–3103.
- Chew, P. L. (1989). Constrained delaunay triangulations. *Algorithmica*, 4(1-4):97–108.
- Crosato, A. (2008). *Analysis and modelling of river meandering*. PhD thesis, Delft University of Technology.
- de Vriend, H., Havinga, H., van Prooijen, B., Visser, P., and Wang, Z. (2011). River Engineering. *Collegedictaat CIE4345*.
- Deltares (2019). *QUICKIN User Manual*.
- Donchyts, G., Schellekens, J., Winsemius, H., Eisemann, E., and van de Giesen, N. (2016). A 30 m Resolution Surface Water Mask Including Estimation of Positional and Thematic Differences Using Landsat 8, SRTM and OpenStreetMap: A Case Study in the Murray-Darling Basin, Australia. *Remote Sensing*, 8(5):386.
- Donchyts, G., Verlaan, M., Baart, F., Santinelli, G., and Rogers, C. (2019). Automated extraction and fusion of the intertidal and subtidal bathymetry from the Landsat and Sentinel satellite data. *EGU General Assembly*, 21:16541.
- Dooren, M. (2019). Combining microwave and optical remote sensing to monitor rivers in monsoon affected regions (MSc thesis). *Delft University of Technology*.
- Durand, M., Fu, L.-L., Lettenmaier, D. P., Alsdorf, D. E., Rodriguez, E., and Esteban-Fernandez, D. (2010). The Surface Water and Ocean Topography Mission: Observing Terrestrial Surface Water and Oceanic Submesoscale Eddies. *Proceedings of the IEEE*, 98(5):766–779.
- DWIR (2014). Directorate of Water Resources and Improvement of River Systems - Vision.

- Engelund, F. and Hansen, E. (1967). A monograph on sediment transport in alluvial streams. *Monografia*.
- Feyisa, G., Meilby, H., Fensholt, R., and Proud, S. (2014). Automated Water Extraction Index: A new technique for surface water mapping using Landsat imagery. *Remote Sensing of Environment*, 140:23–35.
- Gao, B.-c. (1996). NDWI—A normalized difference water index for remote sensing of vegetation liquid water from space. *Remote Sensing of Environment*, 58(3):257–266.
- Ghazavi, M., Hosseini, M., and Mollanouri, M. (2008). A comparison between angle of repose and friction angle of sand. In *The 12th International Conference for International Association for Computer Methods and Advances in Geomechanics (IACMAG)*.
- Gorelick, N., Hancher, M., Dixon, M., Ilyushchenko, S., Thau, D., and Moore, R. (2017). Google Earth Engine: Planetary-scale geospatial analysis for everyone. *Remote Sensing of Environment*.
- Gucma, L., Bilewski, M., Artyszuk, J., and Drwiega, K. (2017). System for Determining Dynamic Under Keel Clearance of Vessels Entering the Port of Swinoujscie (DRWPS). *the International Journal on Marine Navigation and Safety of Sea Transportation*, 11(3):1–7.
- Holland, P. G. (2006). Chézy formula. In *Hydrology and Lakes*, pages 121–121. Kluwer Academic Publishers.
- Huang, C., Chen, Y., Zhang, S., and Wu, J. (2018). Detecting, Extracting, and Monitoring Surface Water From Space Using Optical Sensors: A Review. *Reviews of Geophysics*, 56(2):333–360.
- Jansen, P., Van Bendegom, L., Van den Berg, J., De Vries, M., and Zanen, A. (1994). *Principles of river engineering: The non-tidal alluvial river*. Delftse Uitgevers Maatschappij.
- Julien, P. Y. and Klaassen, G. J. (1995). Sand-Dune Geometry of Large Rivers during Floods. *Journal of Hydraulic Engineering*, 121(9):657–663.
- Kater, E., Makaske, B., and Maas, G. (2012). Morfodynamiek langs de grote rivieren : inventarisatie van processen en evaluatie van maatregelen. Technical report.
- Khan, S. I., Hong, Y., Wang, J., Yilmaz, K., Gourley, J., Adler, R., Brakenridge, G., Policelli, F., Habib, S., and Irwin, D. (2011). Satellite remote sensing and hydrologic modeling for flood inundation mapping in lake victoria basin: Implications for hydrologic prediction in ungauged basins. In *IEEE Transactions on Geoscience and Remote Sensing*, volume 49, pages 85–95.
- Kibele, J. and Shears, N. T. (2016). Nonparametric Empirical Depth Regression for Bathymetric Mapping in Coastal Waters. *IEEE Journal of Selected Topics in Applied Earth Observations and Remote Sensing*, 9(11):5130–5138.
- Kleinhans, M. (2010). Sorting out river channel patterns. *Progress in Physical Geography: Earth and Environment*, 34(3):287–326.
- Kleinhans, M. and van den Berg, J. (2011). River channel and bar patterns explained and predicted by an empirical and a physics-based method. *Earth Surface Processes and Landforms*, 36(6):721–738.
- Koloski, J. W., Schwarz, S., D., and Tubbs, D. W. (1989). Geotechnical Properties of Geologic Materials. *Engineering Geology in Washington*, 1.
- Kuo, C.-Y. and Kao, H.-C. (2011). Retracked Jason-2 Altimetry over Small Water Bodies: Case Study of Bajhang River, Taiwan. *Marine Geodesy*, 34(3-4):382–392.
- KWHRO (2011). Stop damming the Chindwin. *Kuki Women's Human Rights Organization*.
- Léger, J. C. (1999). Menger curvature and rectifiability. *Annals of Mathematics*.
- Lighthart, D. (2017). *The physical processes influencing morphodynamics in braided rivers: A case study on the Ayeyarwady River (MSc thesis)*. Delft University of Technology.
- Lyzenga, D. R. (1978). Passive remote sensing techniques for mapping water depth and bottom features. *Applied Optics*, 17(3):379.

- Mason, D. C., Davenport, I. J., Robinson, G. J., Flather, R. A., and McCartney, B. S. (1995). Construction of an inter-tidal digital elevation model by the 'Water-Line' Method. *Geophysical Research Letters*, 22(23):3187–3190.
- Mason, D. C., Scott, T. R., and Dance, S. L. (2010). Remote sensing of intertidal morphological change in Morecambe Bay, U.K., between 1991 and 2007. *Estuarine, Coastal and Shelf Science*, 87(3):487–496.
- McFeeters, S. K. (1996). The use of the Normalized Difference Water Index (NDWI) in the delineation of open water features. *International Journal of Remote Sensing*, 17(7):1425–1432.
- Mersel, M., Smith, L., Andreadis, K., and Durand, M. (2013). Estimation of river depth from remotely sensed hydraulic relationships. *Water Resources Research*, 49(6):3165–3179.
- Miall, A. D. (1996). *The Geology of Stratigraphic Sequences*. Springer-Verlag Berlin Heidelberg.
- Mosselman, E. (1991). *Modelling of river morphology with non-orthogonal horizontal curvilinear coordinates*. Faculty of Civil Engineering Delft University of Technology.
- Murray, N., Phinn, S., Clemens, R., Roelfsema, C., and Fuller, R. (2012). Continental Scale Mapping of Tidal Flats across East Asia Using the Landsat Archive. *Remote Sensing*, 4(11):3417–3426.
- Nam, K. and Win, E. (2014). Competitiveness between road and inland water transport: The case of Myanmar. *Transport Problems*, 9(4):49–61.
- Olsen, N. R. B. (2003). Three-Dimensional CFD Modeling of Self-Forming Meandering Channel. *Journal of Hydraulic Engineering*, 129(5):366–372.
- Pacheco, A., Horta, J., Loureiro, C., and Ferreira, O. (2015). Retrieval of nearshore bathymetry from Landsat 8 images: A tool for coastal monitoring in shallow waters. *Remote Sensing of Environment*, 159:102–116.
- Patel, A. and Singh, S. (2013). *Remote Sensing: Principles and Applications*. Scientific Publishers.
- Pavelsky, T. M. and Smith, L. C. (2008). RivWidth: A Software Tool for the Calculation of River Widths From Remotely Sensed Imagery. *IEEE Geoscience and Remote Sensing Letters*, 5(1):70–73.
- Peters, R., Hugo, L., and Martijn, M. (2015). Results CoVadem project - How many tracks do we need? Technical report, Delft University of Technology.
- Pfeiffer, A. M., Collins, B. D., Anderson, S. W., Montgomery, D. R., and Istanbuluoglu, E. (2019). River Bed Elevation Variability Reflects Sediment Supply, Rather Than Peak Flows, in the Uplands of Washington State. *Water Resources Research*, 55(8):6795–6810.
- Pipitone, C., Maltese, A., Dardanelli, G., Brutto, M. L., and Loggia, G. L. (2018). Monitoring water surface and level of a reservoir using different remote sensing approaches and comparison with dam displacements evaluated via GNSS. *Remote Sensing*, 10(1):71.
- Project description (2019). Pilot Project Navigation with Nature: a CoVadem application for the Chindwin River, Myanmar. Accessed on April 8 2020 at <https://www.tkideltatechnologie.nl/project/del002-11203221-pilot-project-navigation-with-nature-a-covadem-application-for-the-chindwin-river-myanmar/>.
- QUICKIN (2020). QUICKIN User Manual. Accessed on May 2 2020 at https://content.oss.deltares.nl/delft3d/manuals/QUICKIN_User_Manual.pdf.
- Sagar, S., Roberts, D., Bala, B., and Lymburner, L. (2017). Extracting the intertidal extent and topography of the Australian coastline from a 28 year time series of Landsat observations. *Remote Sensing of Environment*, 195:153–169.
- Schuurman, E., Marra, W., and Kleinhans, M. (2013). Physics-based modeling of large braided sand-bed rivers: Bar pattern formation, dynamics, and sensitivity. *Journal of Geophysical Research: Earth Surface*, 118(4):2509–2527.
- Shields, A. (1936). Application of similarity principles and turbulence research to bed-load movement. *Mitteilungen der Preussischen Versuchsanstalt für Wasserbau und Schiffbau*.

- Shilpi, Singh, R. M., and Maurya, S. P. (2014). River network identification using Remote Sensing and GIS. In *2014 Students Conference on Engineering and Systems*, pages 1–6. IEEE.
- Smith, L. C., Isacks, B. L., Forster, R. R., Bloom, A. L., and Preuss, I. (1995). Estimation of Discharge From Braided Glacial Rivers Using ERS 1 Synthetic Aperture Radar: First Results. *Water Resources Research*, 31(5):1325–1329.
- Smith, L. C. and Pavelsky, T. M. (2008). Estimation of river discharge, propagation speed, and hydraulic geometry from space: Lena River, Siberia. *Water Resources Research*, 44(3).
- Talmon, A., Struiksma, N., and van Mierlo, M. (1995). Laboratory measurements of the direction of sediment transport on transverse alluvial-bed slopes. *Journal of Hydraulic Research*, 33(4):495–517.
- Terzaghi, K. (1934). Large retaining-wall tests. I. Pressure of dry sand. *Engineering News-Record*.
- Thissen, J. (2019). *Automating surface water detection for rivers - The estimation of the geometry of rivers based on optical earth observation sensors (MSc thesis)*. University of Twente.
- Tsang, L., Kong, J. A., and Shin, R. T. (1985). Theory of microwave remote sensing. *Wiley Series in Remote Sensing and Image Processing*.
- van der Mark, C. E., Vijververg, T., and Ottevanger, W. (2015). Paper 114 – Validation of Actual Depth Measurements by Inland Vessels. In *Smart Rivers 2015*.
- van der Velden, J. (2015). Understanding river dynamics of the Ayeyarwady River, Myanmar How dynamic behaviour contributes to adapting the river morphology for navigational purposes (MSc thesis). *Universiteit Utrecht*.
- van Duijn, E. (2018). The effects of vegetation on riverbank stability in the Ayeyarwady River: The use of the Normalised Difference Vegetation Index as indicator for stabilising effects of vegetation by measuring bank retreat rates (MSc thesis). *Delft University of Technology*.
- van Rijn, L. C. (1984a). Sediment Transport, Part I: Bed Load Transport. *Journal of Hydraulic Engineering*, 110(10):1431–1456.
- van Rijn, L. C. (1984b). Sediment transport, part III: Bed forms and alluvial roughness. *Journal of Hydraulic Engineering*, 110(12):1733–1754.
- van Rijn, L. C. (1993). Simple General Formulae for Sand Transport in Rivers, Estuaries and Coastal Waters. *Www.Leovanrijn-Sediment.Com*.
- Vellinga, T. (2019). Navigation with Nature - A pilot on the Chindwin river in Myanmar. In *PIANC Smart Rivers Conference Lyon*.
- Wirdum van, M., Audenaerdt, R., and Verheij, H. (2015). Pilot water depth measurements by the commercial fleet. *PIANC word congress 2014*.
- Xu, H. (2006). Modification of normalised difference water index (NDWI) to enhance open water features in remotely sensed imagery. *International Journal of Remote Sensing*, 27(14):3025–3033.
- Yoon, Y., Durand, M., Merry, C. J., Clark, E. A., Andreadis, K. M., and Alsdorf, D. E. (2012). Estimating river bathymetry from data assimilation of synthetic SWOT measurements. *Journal of Hydrology*.
- Zervakis, D. (2015). *Combining a Physics-based Model and Spatial Interpolation of Scarce Bed Topography Data in Meandering Alluvial Rivers (MSc thesis)*. Delft University of Technology.
- Zhu, Z. and Woodcock, C. E. (2012). Object-based cloud and cloud shadow detection in Landsat imagery. *Remote Sensing of Environment*, 118:83–94.
- Zhu, Z. and Woodcock, C. E. (2014). Automated cloud, cloud shadow, and snow detection in multitemporal Landsat data: An algorithm designed specifically for monitoring land cover change. *Remote Sensing of Environment*, 152:217–234.
- Zimmerman, C. and Kennedy, J. F. (1978). Transverse bed slopes in curved alluvial streams. *Journal of the Hydraulics Division*, 104(HY1).

A

Appendix Background Research

A.1. Remote sensing

Remote sensing sensors can be roughly subdivided in two major groups: active and passive sensors [Tsang et al., 1985]. Within the same type of satellites also a lot of variation occurs in features such as spatial and temporal resolution, type and number of sensed spectral bands and (temporal) data availability. To distinguish between river and non-river parts, a remote sensing method beneficial to this thesis should initially be able to detect surface water.

Electro-optical sensors vs Synthetic Aperture Radar

Two types of remote sensing, *Synthetic Aperture Radar* (SAR) and *Electro-Optical* (EO) seem probable for detection of surface water. SAR systems are different from EO sensors in that they actively transmit microwaves and collect the reflected signals. EO sensors merely sense radiance reflected by the earth's surface. Microwave signals are not influenced by the time of the day and/or the weather conditions which makes SAR highly reliable. The advantage of EO over SAR is the ease of interpretation. EO sensors generally capture many bands of the electromagnetic spectrum, including visible light. This makes interpretation easy because images look similar to how our eyes observe the world.

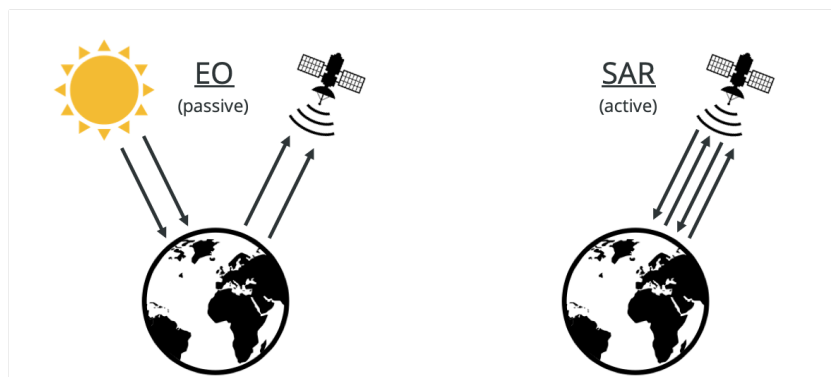


Figure A.1: Principles of passive Electro-Optical (EO) remote sensing (Sentinel-2) and Synthetic Aperture Radar (SAR) remote sensing (Sentinel-1)

An overview of the characteristics of EO and SAR is given in Table A.1. Based on the ease of analysis it was chosen to continue solely with passive EO sensing.

Available EO missions

Within the Electro-Optical sensing a range of different satellite missions exist. Huang et al. [2018] summarised the most commonly used datasets for surface water detection. The missions (see Table A.2) have been classified in three groups based on the pixel scale at which the sensors observe the earth: coarse, medium and high resolution.

Table A.1: Comparison between characteristics of Electro-Optical sensing (EO) and Synthetic Aperture Radar (SAR)

	Electro-Optical (EO)	Synthetic Aperture Radar (SAR)
Sensors	Optical (passive)	Microwave (active)
Elevation measurements	Limited	Yes
Weather conditions	Limited	All
Data interpretation	Direct	Processing required

Table A.2: Overview of commonly used satellites/sensors for surface water detection. This thesis makes use of the Sentinel-2 MSI and Landsat missions. (modified from Huang et al. [2018])

Scale	Satellite/Sensor	Number of Bands	Spatial Resolution (m)	Temporal Resolution (days)	Data Availability
Coarse > 200 m	NOAA/AVHRR	5	1100	0.5	1978 -
	MODIS	36	250 - 1000	0.5	1999 -
	Suomi NPP-VIIRS	22	375 - 750	0.5	2012 -
	MERIS	15	300	3	2002 - 2012
	Sentinel-3 OLCI	21	300	2	2016 -
Medium 5 - 200 m	Landsat	4 - 9	15 - 80	16	1972 -
	SPOT	4 - 5	2.5 - 20	26	1986 -
	Aster	14	15 - 90	16	1999 -
	Sentinel-2 MSI	13	10 - 60	5	2015 -
High < 5 m	IKONOS	5	1 - 4	1.5 - 3	1999 -
	QuickBird	5	0.61 - 2.24	2.7	2001 -
	WorldView	4-17	0.31 - 2.40	1 - 4	2007 -
	RapidEye	5	5	1 - 5.5	2008 -
	ZY-3	4	2.1 - 5.8	5	2012 -
	GF-1/GF-2	5	1 - 16	4 - 5	2013 -

A higher resolution is generally to be preferred over a lower resolution. However, most of the high resolution data is not open access. Other assets that play an important role are (temporal) data availability and temporal resolution (flyover frequency). Finally, surface water is best detected from certain wavelengths and therefore these wave lengths should be covered by the spectral bands of the satellite (see §2.3.1).

The coarse resolution group, with a resolution larger than 200 x 200 m is used primarily for large scale assessment of land and/or ocean properties. Since this large pixel scale is in the same order as the river width, it is not suitable for river bathymetry estimates. The high resolution sensors can potentially be very beneficial for river assessment but are not available free of charge and can therefore not be used.

For this thesis the medium resolution data from the *Landsat* and *Sentinel-2* missions is used. This decision was primarily based on the accessibility of the datasets in combination with an acceptable (10 - 30 m) resolution. For Sentinel-2 the pixel resolution of the relevant bands for water detection ranges from 10 to 20 m. Landsat consists of multiple missions, but primarily Landsat 8 was used. The relevant bands from Landsat 8 are sensed at 15 to 30 m pixel scale. The larger scale pixels are subsequently re-sampled to 10 m scale and can accordingly be analysed on a higher resolution. However, this inevitably causes lower precision of the data.



Figure A.2: Rugplot of obstructed (red) and unobstructed (green) images near Sagain from Landsat 8 and Sentinel 2 in 2018. A total 106 images was taken during this period from which 78 were considered clear enough to be used. (modified from [Dooren, 2019])

Figure A.2 shows the availability of data in 2018 for an area of the Ayeyarwady. The results are also exemplary for the Chindwin, because the Chindwin and the Ayeyarwady share a similar climate. The rug plot shows that

clouds obstruct many of the images during the monsoon period, causing those images to be discarded (red stripes). Navigability issues mostly play a role outside the monsoon period, during this period the biggest part of the images is considered usable (green stripes).

Elevation measurements with SAR

In §2.3 the importance of retrieving 3D bathymetry data was stressed. SAR boasts a big advantage over EO in that it can directly measure surface elevation and by doing so provide 3D information. The elevation is calculated from the elapsed time between transmission and reception of a microwave signal. This *radar altimetry* (= measuring surface height) was originally designed for ocean applications and therefore it has some constraints whenever inland use is desired (e.g., corrections, re-tracking, geographical effects) [Pipitone et al., 2018]. The typical spatial scale for (open access) radar altimetry data starts from the order of a hundred to a few hundred meters [Birkett and Beckley, 2010, Kuo and Kao, 2011]). This scale doesn't quite capture the small scale deviations in elevation in water surface and river banks. For this reason usage of radar altimetry was not further considered.

In 2021 the *Surface Water and Ocean Topography* (SWOT) mission is scheduled for launch [NASA]. This mission will provide global coverage of surface water elevation with an unprecedented resolution [e.g., Durand et al., 2010, Mersel et al., 2013, Yoon et al., 2012]. It is recommended to further investigate possibilities of radar altimetry for river application when the data from this mission becomes available.

Inverse-depth estimated from multispectral optical satellite imagery

Another investigated option was to deduct 3D information from 2D data is inverse-depth estimation. This method works based on the variation in reflectance from different spectral bands for different water depths. It is best explained by visualising shallow and deep water. The shallow water is generally lighter and will reflect more in particular spectral bands compared to whereas the deeper water will absorb more. The theory, first introduced by Lyzenga [1978], has been applied at many locations around the world with good results [e.g., Kibele and Shears, 2016, Pacheco et al., 2015, Sagar et al., 2017]. An initial assessment was made to see if this theory could also be helpful for the Chindwin. Unfortunately, for it to work properly, clear water is necessary. The high levels of turbidity present at the Chindwin in combination with the turbidity fluctuations throughout the year, made it impossible to draw up useful relationships between water reflectance and water depth. Therefore this option was not deemed promising enough to be further investigated.

Bathymetry from combined water masks (*water occurrence*)

Two options have been investigated to link 2D imagery with 3D bathymetry: *inverse-depth estimation* and the use of *water occurrence*. The first option, introduced by Lyzenga [1978], uses the variation in water reflectance between shallow and deep water to estimate water depth. Applications can be found in e.g. Pacheco et al. [2015] and Kibele and Shears [2016]. The option was found unsatisfactory for the Chindwin because of the high (and fluctuating) turbidity levels. The high turbidity levels prevented a stable and usable relation between water reflectance and depth. The second option links the fraction of the time an area is covered by water (*water occurrence*) to the bed elevation. This option and its limitations are further explained in the remainder of this section.

As mentioned before, one of the downsides of (passive) multispectral imagery is that no elevation data is transmitted. Analysing the (2D) river contour is therefore relatively simple, but finding the river bathymetry (3D) is not. This section discusses the theory behind establishing the link between water occurrence and bathymetry.

A.2. Classification of bed forms

The axi-symmetric solution can provide information about the cross-section scale shape of a river given that certain criteria are met. On a smaller scale, the uncertainty of the bed level can be estimated based on the types and dimensions of the bed-forms present. The van Rijn classification is used for determination of (1) the type of bed-forms and (2) the bed-form dimensions. The dimensions found are a rough estimate of reality.

A method for the classification of bed-forms and the prediction of bed-form dimensions was presented by van Rijn [1984a] after defining a dimensionless particle diameter d_* and a transport-stage parameter T as follows [Julien and Klaassen, 1995]:

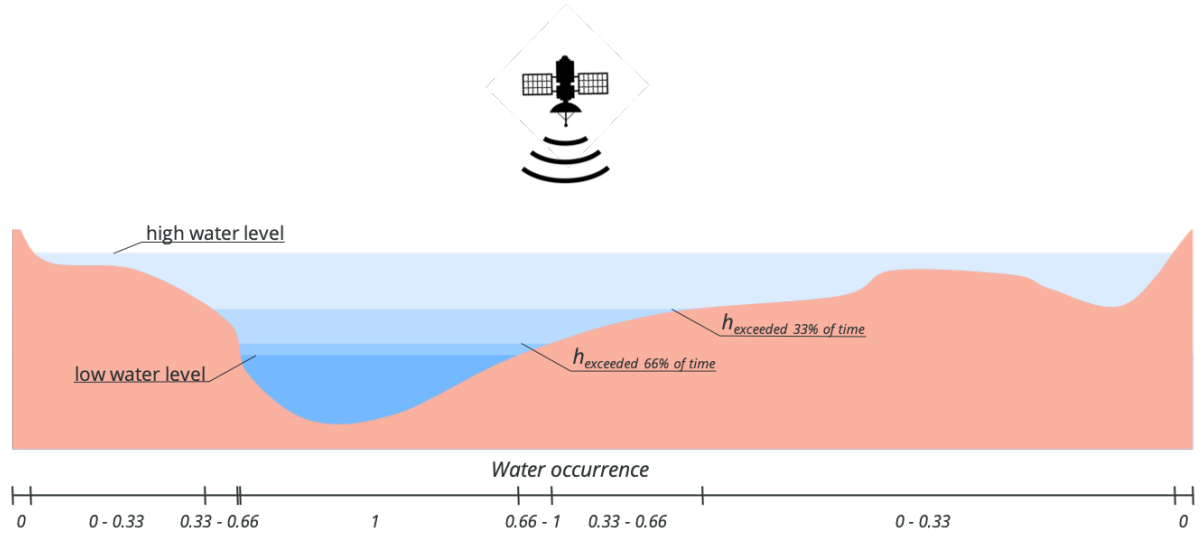


Figure A.3: Bathymetry estimate based on water occurrence. A lower water occurrence means a higher position of the bed. The link between water occurrence and bottom elevation can be established through CoVadem measurements.

$$d_* = d_{50} \left(\frac{\Delta g}{\nu^2} \right)^{1/3} \quad (\text{A.1})$$

$$T = \frac{(u'_*)^2 - (u_{*c})^2}{(u_{*c})^2} \quad (\text{A.2})$$

Where:

d_{50}	= median bed particle (50% passing by weight)	[m]
Δ	= relative density of sediment	[-]
ν	= kinematic viscosity	[m ² /s]
u_{*c}	= critical grain shear velocity	[m/s]
u'_*	= $\bar{u}\sqrt{g}/C$, grain shear velocity	[m/s]
\bar{u}	= mean flow velocity	[m/s]

Bed-form dimensions in terms of height and steepness were analysed by van Rijn [1984b] after selecting data according to (1) dune bed forms; (2) width-depth ratio larger than 3; (3) flow depth larger than 0.1 m; and (4) transport-stage parameter T smaller than 25. Van Rijn proposed the bed-form classification diagram in which ripples are found $d_* < 10$ and $T < 3$. Dunes occur when $T < 15$, with washed-out dunes at $15 < T < 25$, and upper regime plane bed as $T > 25$.

The critical grain shear velocity u_{*c} in (A.2) is equal to $\sqrt{\tau_{cr}/\rho}$ where $\tau_{cr} = \theta_{cr}(\rho_s - \rho_w)gd_{50}$. Unknown value in this equation is the critical Shields parameter θ_{cr} which is calculated with (A.3). Insertion of $d_{50} \approx 400\mu\text{m}$ (value based on expert consultation), relative density $\Delta = 1.65$, and kinematic viscosity $\nu = 1.004 \cdot 10^{-6}$ into (A.1) yields $d_* = 10.01$. A value of 0.032 for the critical Shields parameter θ_{cr} is found when computing (A.3) [van Rijn, 1993]. The corresponding critical grain shear velocity u_{*c} consecutively becomes 0.012 m/s.

$$\theta_{cr} = \frac{0.04}{d_*^{0.1}} \quad \text{for} \quad 10 < d_* < 20 \quad (\text{A.3})$$

Julien and Klaassen [1995]: 'The best agreement obtained by regression analysis for the dune height δ and dune length λ as a function of the average flow depth h , bed particle diameter d_{50} and transport-stage parameter T is respectively given by':

$$\frac{\delta}{h} = 0.11 \left(\frac{d_{50}}{h} \right)^{0.3} (1 - e^{-0.5T})(25 - T) \quad (\text{A.4})$$

$$\frac{\delta}{\lambda} = 0.015 \left(\frac{d_{50}}{h} \right)^{0.3} (1 - e^{-0.5T})(25 - T) \quad (\text{A.5})$$

Table A.3: Assessment of the bed-form classification for 5 sites with flow velocity and water depth data availability. *washed-out dunes are expected for Htamanthi according to van Rijn, however this is disputed by others e.g. [Julien and Klaassen, 1995]

		Khamtee	Htamanthi	Kalewa	Monywa
data acquired (around)	2016	Jun-28	Sep-4	Sep-21	Nov-21
mean velocity, \bar{u}	[m/s]	1.4	1.9	1.3	1.2
mean water depth, h	[m]	7.0	10.0	14.0	3.5
dimensionless diameter, d_*	[-]	10.09	10.09	10.09	10.09
transport stage parameter, T	[-]	13.11	19.86	9.29	9.93
van Rijn classification		dunes	washed-out dunes	dunes	dunes
dune height, δ	[m]	0.49	0.34*	0.82	0.38
dune length, λ	[m]	51	103*	73	26

Conclusion bed-forms

Based on the hydrographical data that is available from 4 sites along the Chindwin, a general feeling of the bed-forms present is achieved. Larger, and higher dunes can be expected during the monsoon period (June - October). When flow velocity and water level drop the amplitude and length of the dunes significantly decreases.

The calculations presented above are largely based on empirical tests and based on dubious measurements. It is therefore perhaps unwise to use the output as the governing dimensions for dunes: either unacceptable uncertainties or a very large additional safety factor are present. The dune height and steepness can most likely also be estimated from the along-flow CoVadem signal. This is achieved by relating the along-flow dune properties to the transverse flow ones. It is beyond the scope of this research to extract dune properties from CoVadem data, but it is recommended to thoroughly investigate doing this in the future.

B

Appendix Methodology

B.1. River discretisation

The river is discretised by creating a river polygon first and a curvilinear grid after.

River polygon

The river polygon was created with the Deltares QUICKIN tool [QUICKIN, 2020]. For every study case, the available data was plotted in this tool. Consecutively a *land boundary file* was drawn by hand carefully following the outer contours of the measured data. The *land boundary file* is carefully drawn by hand just inside the extent of the measured data. The polygon had to be within the extent of the grid because in a later phase, the measured data points are projected on the grid. To have an interpolated value for all grid points, they must all be within the *triangulation* extent of the measured data. The river polygon is exported in either *shapefile* (.shp) or *land boundary file* (.ldb) format. This thesis used a land boundary file.

Curvilinear grid

Curvilinear grid construction was carried out with the Deltares - Rapid Assessment Tool for Inland Navigation (D-RATIN). This tool automates grid construction, the following input is required:

- **Number of cells (half width)**

For a curvilinear grid, the local cell width depends on the local river width and the amount of cells. For the D-RATIN tool the number of cells per half width must be specified. With 100 transverse cells, the cell widths for the investigated study cases range from 3 to around 11 meter (on average 6 m). This is in the same order of the CoVadem ship widths.

- **Polygon smoothing**

The initial boundary file can be too detailed and can consist of sharp edges that can cause errors in the model computations. Therefore the polygon is smoothed. The D-RATIN smoothing tool uses a series of buffering and de-buffering methods, effectively expanding and contracting the size of the polygon resulting in a removal of minor distortions. The effect of smoothing is shown in Figure B.1. The smoothing factor used for this thesis is 20. There did not seem to be much of a difference for varying smoothing factors. This is probably because the polygons were drawn by hand and therefore did not consist of any sharp edges in the polygon where smoothing was necessary. Sharp edges are more likely to occur in the case that the river polygon is e.g., derived automatically from satellite imagery [Thissen, 2019, e.g.]. Visual observation shows that a smoothing factor of 20 results in sufficient removal of disturbances.

- **Along flow cell length**

Grid sizing is very important. Grid sizing is based on approximate ship dimensions. The D-RATIN tool requires a cell length along the centreline. A length of 25 m was picked based on some images of typical ships (see Figure B.2).

- **Shortening of the grid**

The way the grid is calculated results in a weird looking grid at the beginning and the end of the grid.

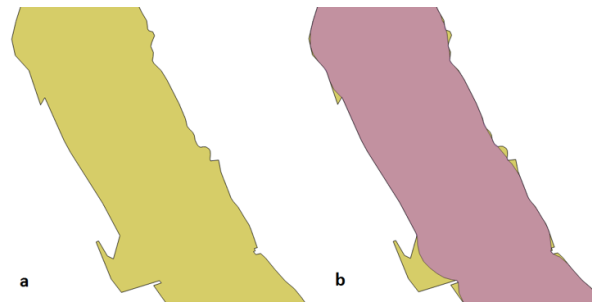


Figure B.1: Visualisation of how smoothing works for a polygon in the Danube river (not among the study cases) [Zervakis, 2015]



Figure B.2: A ship somewhere on the Chindwin. Courtesy CDR International

The *shortening* parameter determines the number of cross-sections at the beginning and end of the grid that are removed. The amount of applied shortening was iteratively determined based on visual observation. Generally a more dense grid required more shortening.

Curvilinear grid in Python

Most of the calculations and visualisations were carried out with *Python*. The discretised river (previous section) is at this point contained in a *.grd* file that can be read by e.g., DELFT-3D. To perform calculations on the grid primarily two *DataFrames* from the *Pandas* software library were used. A *DataFrame* can be seen as a large table in Python on which a wide range of operations can be applied.

The first of the two primary *DataFrames* is called simply *df* in the python scripts. This *DataFrame* contains information per grid node. The *.grd* file was imported in python and a *DataFrame* with $m \times n$ rows and 4 columns was created. The columns are: 'm', 'n', 'x', 'y'. Many additional columns were added later. The second *DataFrame* is called *dfextra*, it contains information per cross-section. Information such as the cross-section width, cell width, curvature along the centreline etc is stored here.

B.2. Data formatting, cleaning and georeferencing

The local measurements were extracted from *AutoCad* drawings provided by *DWIR*. The measurements were initially loaded in *ArcGis* and exported to a Comma Separated Value (*.csv*) file. In this file three columns (x, y, z) are present, showing the coordinates of the measured points. The structure of the *.csv* files is as follows:

| X (m, local CRS) | Y(m, local CRS) | Z (m + local reference level) |

The measured bed levels (z column) did not show any unrealistic outliers so no additional cleaning was applied on the data. The coordinate reference system (CRS) for all sites is *EPSG:23946*. After comparison with satellite imagery it was found that some of the study case measurements had a significant spatial offset. Therefore the data was *georeferenced* (i.e., aligned with satellite images).

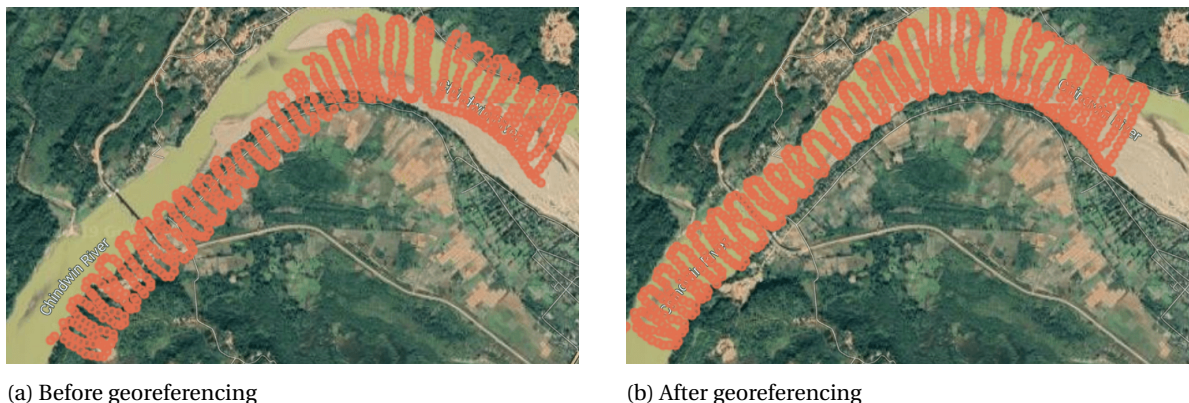


Figure B.3: Example of .xyz data before and after georeferencing near Khamtee

Table B.1: Spatial transformation applied on the measurements from the different study cases

		Khamtee	Htamanthi	Kalewa	Monywa
Adjustment x	[m]	-335	50	0	-310
Adjustment y	[m]	65	0	0	100

The selected procedure for *georeferencing* is as follows:

- The xyz , stored in a .csv file is imported in Python as a *Pandas GeoDataFrame*.
- A (user defined) transformation is applied to all points in the *DataFrame*
- The data is reprojected from the EPSG:23946 to the WGS84 coordinate reference system, and exported as a *shapefile*
- The *shapefile* is imported in *Google Earth Engine* and visually compared with satellite images close to the measurement date
- The procedure is iteratively repeated
- When a good visual match is found, the data is exported as a (transformed) xyz .csv file.

An example of the data before and after referencing is shown in Figure B.3.

B.3. Data interpolation

If one wishes to estimate the bed elevation in a grid node where no measurement is located, interpolation is necessary. There are many ways in which the data can be interpolated, for practical reasons this thesis uses the QUICKIN triangulation tool. The tool is created for "Generation and manipulation of grid-related parameters such as bathymetry, initial conditions and roughness" [Deltares, 2019].

The available sample data for the study case of Htamanthi are shown in Figure B.4a. The curvilinear grid in Figure B.4b. First the points are triangulated with Delaunay triangulation [Chew, 1989]. Based on the triangulated surface, the bed levels in the grid points are calculated with Linear Barycentric Interpolation (Figure B.3). The projected measurements on the grid are shown in Figure B.4c.

B.4. Water occurrence time-window

This thesis uses many low water images to estimate how stable a cross-section is. The length of this time window is however rather arbitrary. Here the influence of the selected time window is discussed. Different time windows were applied for the Monywa study case. This case was selected because it has both stable and unstable areas.

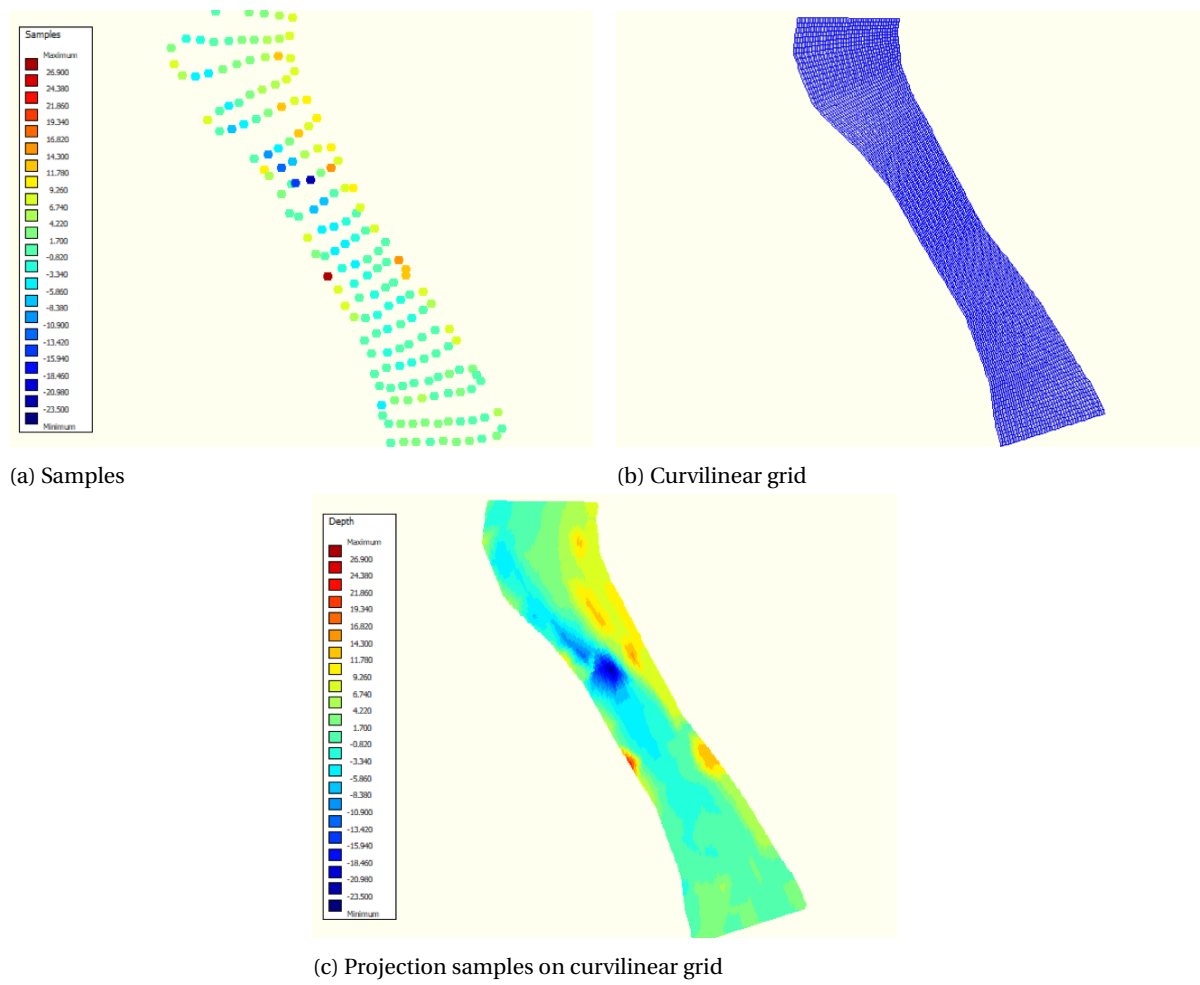
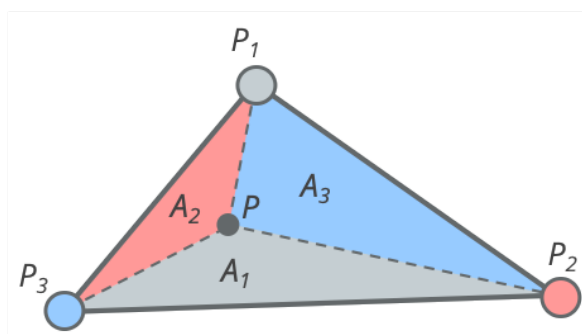


Figure B.4: Projection of unstructured data on the curvilinear grid for the Htamanthi study case



$$P = \frac{A_1 P_1 + A_2 P_2 + A_3 P_3}{A_{tot}}$$

Figure B.5: Linear Barycentric Interpolation. Method to calculate the value of P , lying in between three sampled points. The three points are weighted based on the area of the triangle on their respective opposite sides.

Water occurrence maps and *stability scores* have been calculated according to the method described in 3.5. Only the time windows were changed to 2, 5, 10 and 20 years. The result for the different time windows are shown in Figure B.7.

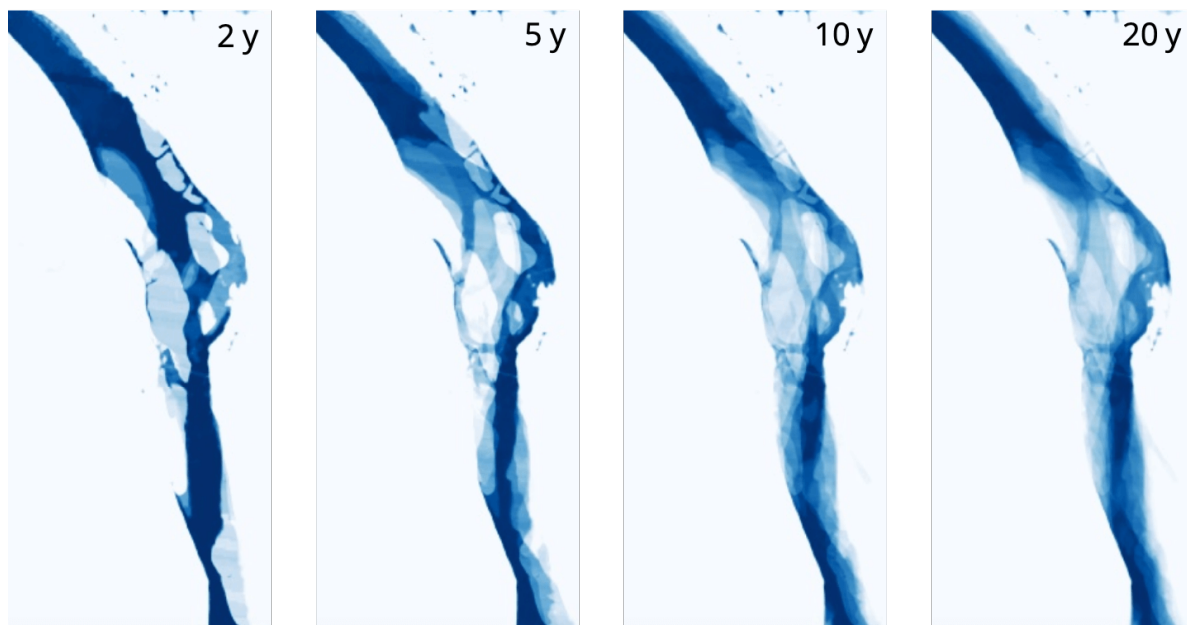


Figure B.6: *Water occurrence* maps near Monywa based on a 2, 5, 10 and 20 year window (ending in 2016).

Based on the water occurrence the stability scores per cross-section were calculated. The applied bins to distinguish between stable dry, unstable and stable wet were water occurrence values of 0 - 0.15 (stable dry), 0.15 to 0.85 (unstable) and 0.85 to 1 (stable wet) respectively.

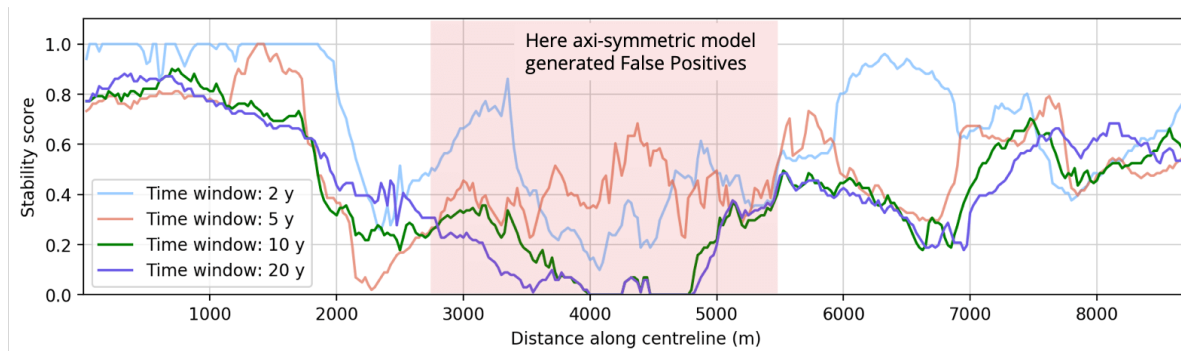


Figure B.7: Stability score for different time windows. The red area shows the location where the axi-symmetric model failed. Preferably a bad performance of the axi-symmetric model is indicated by a low channel stability score. The longer time windows perform better here. Note how the 10 y and 20 y scores are not so different from each other

Stability score technical part

The curvilinear grids used for all study cases have for every grid node an x and y coordinate in coordinate reference system (CRS) EPSG:23946. Earth Engine, used to calculate the *water occurrence* maps, preferably uses the world EPSG:4326 system (Genna Donchyts, personal communication, not tested by the author). Therefore the grid points were reprojected into EPSG:4326 and exported as a *shapefile*. The *shapefile* is consecutively imported as an *asset* in Earth Engine. The water occurrence values were extracted in the grid nodes. The grid and the *water occurrence* values were exported as a .csv file and imported and added to the existing 'dfextra' *Pandas DataFrame*.

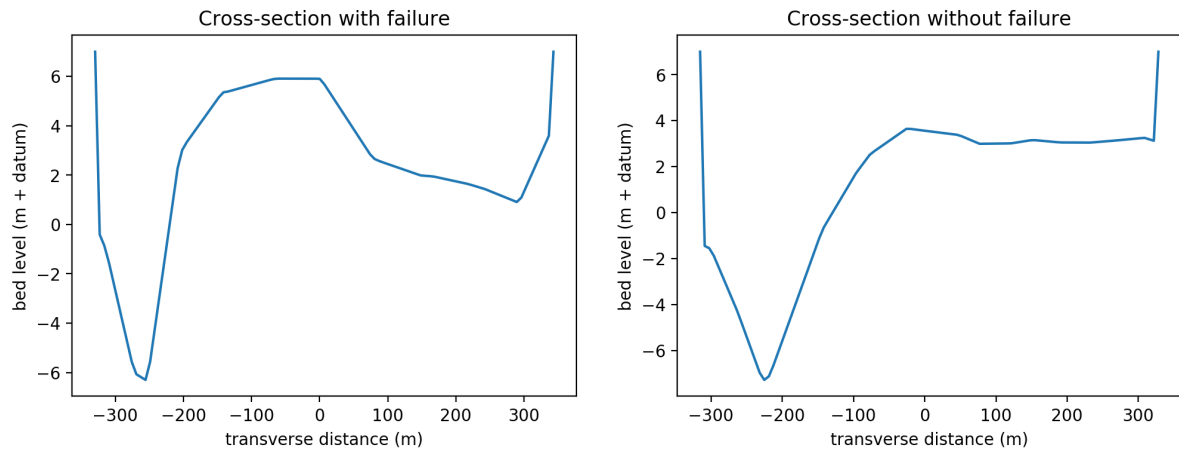


Figure B.8: Two cross-sections from the Kalewa study case. The left figure shows a cross-section where the axi-symmetric model fails, the right figure shows a cross-section where the axi-symmetric model works fine.

B.5. Calibrating the axi-symmetric model

The axi-symmetric model was calibrated for its most uncertain model parameter, the coefficient for the influence of helical flow, a . The model calibration took place by applying different values of a and evaluating the model performance every time. Calibration took place for the study case of Kalewa, because the bathymetry for this study case showed the most similarities with the typical axi-symmetric solution bathymetry out of the available study cases.

Figure B.9 shows the effect of different calibration coefficients a on the performance indicators. In the top graph the safety score, the measure for the axi-symmetric model reliability, is plotted against the along flow distance. In the bottom graph, the *channel coverage score*, a measure for the size of the navigable area estimate is plotted. The Figure shows that with increasing calibration coefficients a , the safety score increases while the channel coverage decreases and vice versa. In other words, the model becomes more conservative with increasing values of a .

Based on Figure B.9 a value of 5 for the calibration coefficient a was selected (blue striped line). However, it is noted that the selection for a value of a is depends on what is preferred by the end user: reliability vs size of the estimate. With this coefficient the model fails at one location only. In Figure B.8 (left) a cross-section is depicted where the axi-symmetric model fails. The water level during the time of measurements was approximately 7.1 (m + datum). The axi-symmetric solution is not designed for such cross-sections and calibrating it based on such cross-sections would not be just: the model would be calibrated to take into account morphological artefacts that seem to have nothing to do with the processes accounted for by the axi-symmetric model.

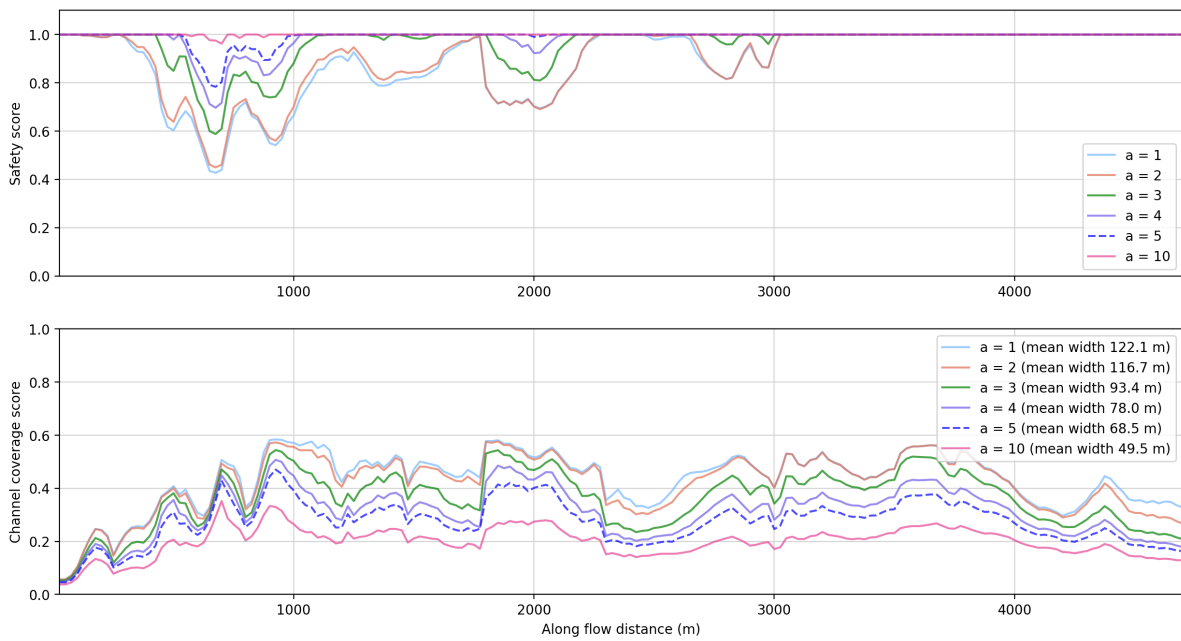


Figure B.9: The safety score (above) and channel coverage score (below) calculated along the centreline of the Kalewa study case

C

Appendix Results

C.1. Results Khamtee

The study case of Khamtee is positioned the most upstream out of the four study cases. The available data was collected in a bend close to the town of Khamtee. In Figure C.1 and overview is given of the site, including the bathymetry for the part of the river where measurements were available.

Data of an example (synthetic) CoVadem ship track is shown in Figure C.2 (upper left). The lower figures display the navigable area estimate based on this data with the soil-model (lower left) and axi-symmetric model (lower right). Consecutively, in Figure C.3 (right), the channel stability score is plotted graphically along the centreline. In Figure C.4 the reliability of the axi-symmetric model, the stability score and the curvature ratio of the river are plotted in a single graph.

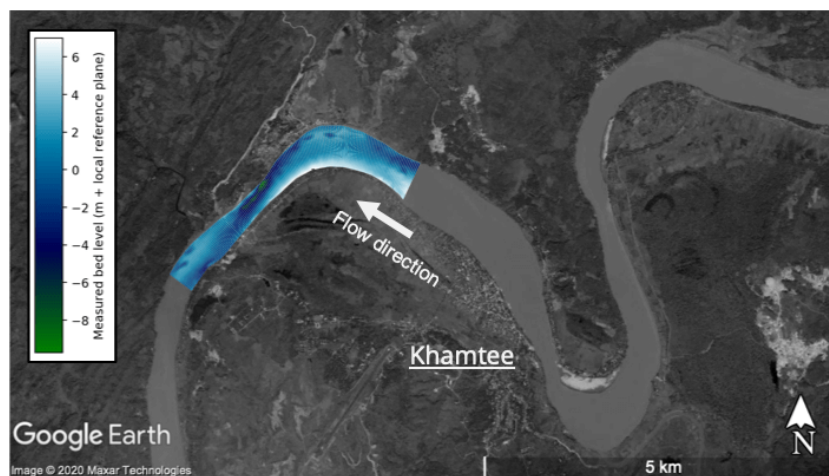


Figure C.1: Overview of the Chindwin river near Khamtee, including the bathymetry

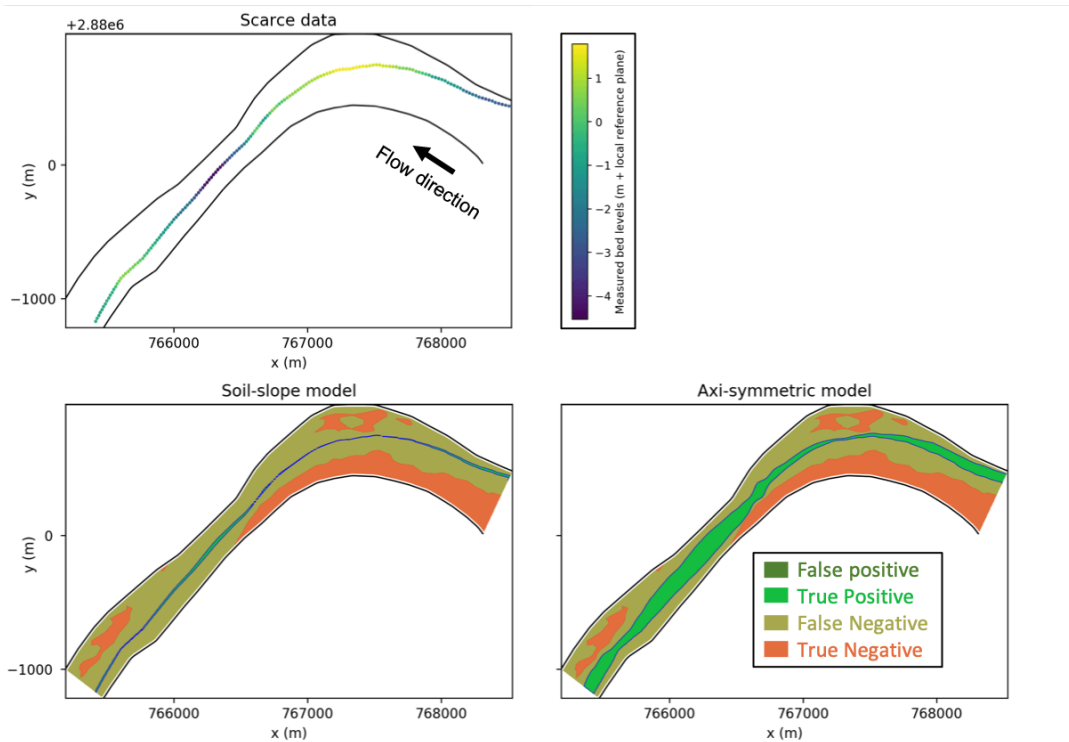


Figure C.2: The navigation channels calculated from a scarce dataset (above). The lower left image displays the navigable area estimate for the soil-model, the lower right image for the axi-symmetric model. On the background the ground truth navigation channel is plotted for comparison

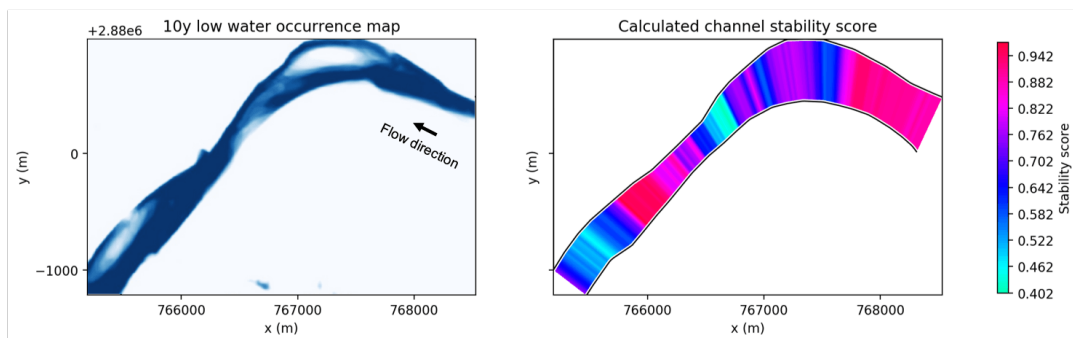


Figure C.3: Left: the 10 year low-water water occurrence map. Right: the calculated stability score, measure for how stable the channel is locally (Khamtee study case)

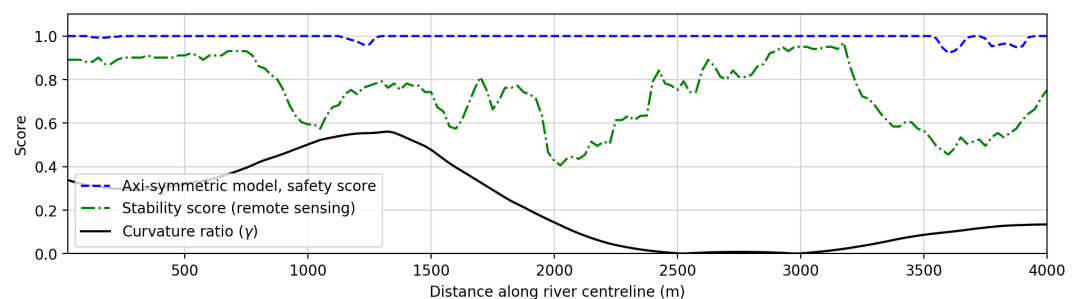


Figure C.4: The safety score of the axi-symmetric model, measure for the reliability of the model, along the centreline of the Htamanthi study case. Moreover the channel stability score (remote sensing) and the curvature ratio are plotted

C.2. Performance indicators all study cases

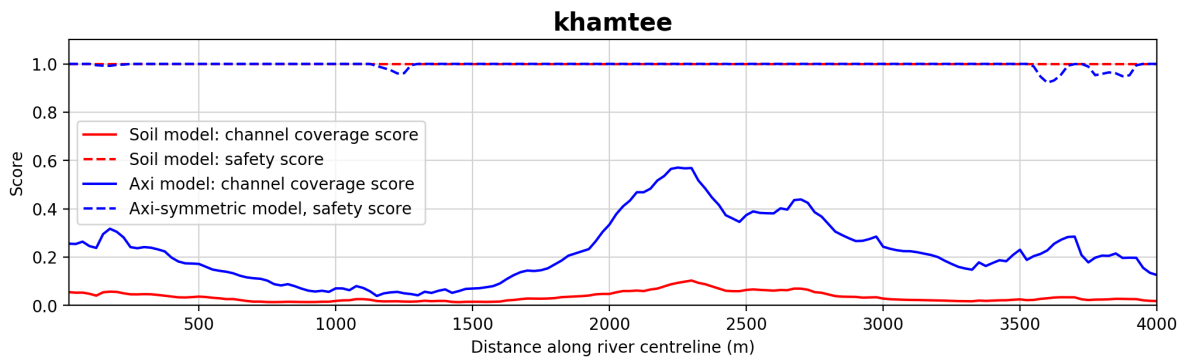


Figure C.5: The calculated channel coverage scores and safety scores for the soil-model and axi-symmetric model

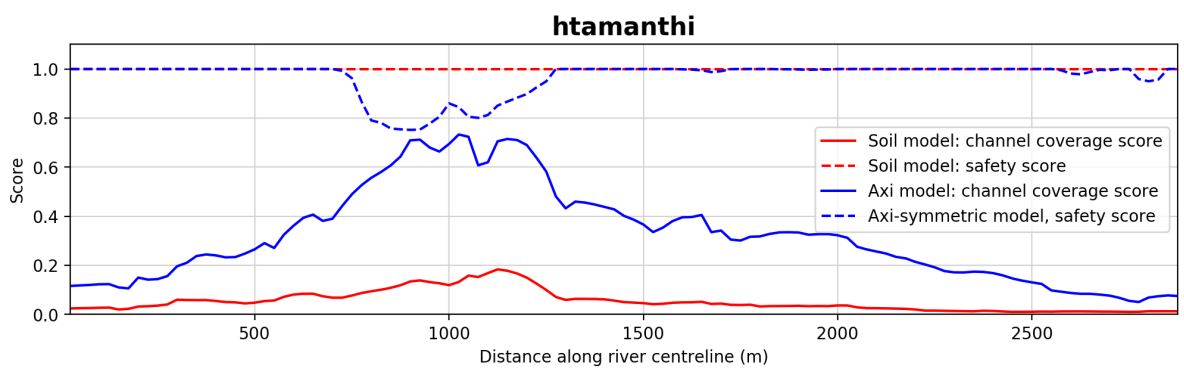


Figure C.6: The calculated channel coverage scores and safety scores for the soil-model and axi-symmetric model

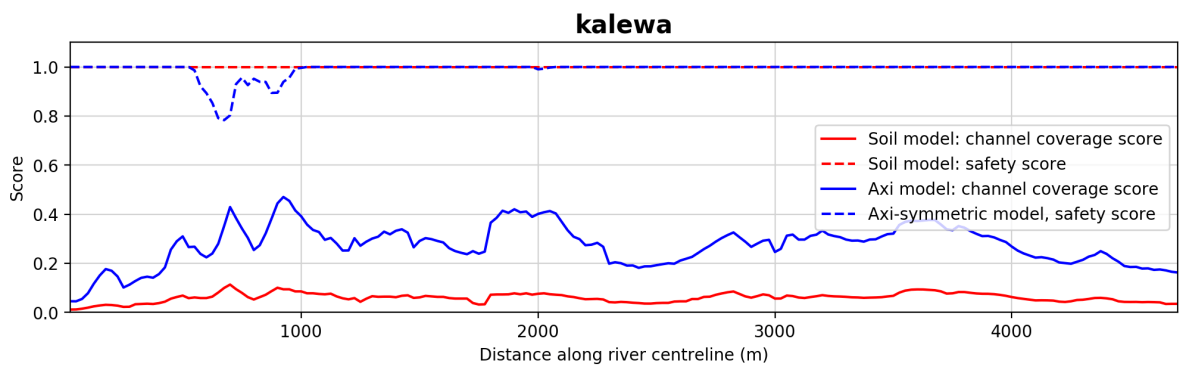


Figure C.7: The calculated channel coverage scores and safety scores for the soil-model and axi-symmetric model

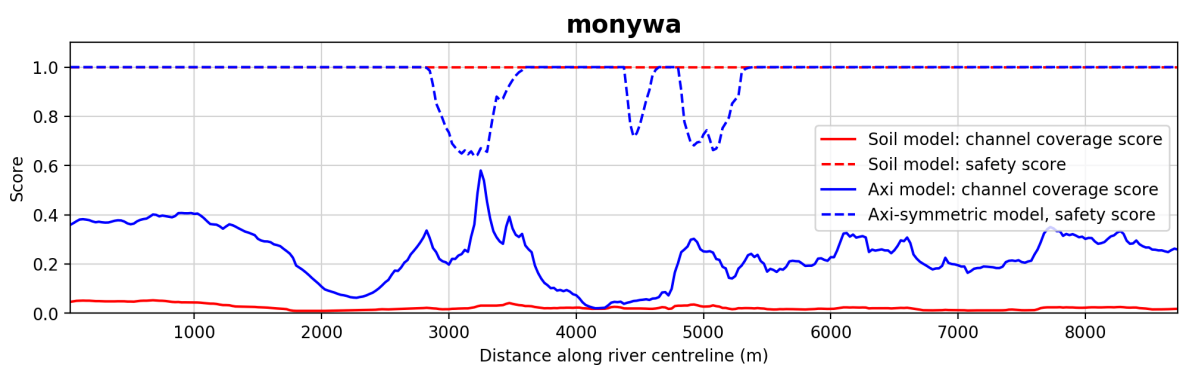


Figure C.8: The calculated channel coverage scores and safety scores for the soil-model and axi-symmetric model

C.3. Simultaneous application of two reliability thresholds

In the results section (§4.2 the reliability indicators (stability score and curvature ratio) were used separately from each other. Some additional exploration was carried where the two reliability indicators were used at the same time. This was carried out as follows: the axi-symmetric model was applied for all cross-sections where at least one of the thresholds (curvature and/or stability) was met. In Figure C.9, 10,000 different combinations of thresholds have been evaluated for the safety score and applicability. The two graphs display the same data, however, the upper graph shows the values of the stability score thresholds while the lower graph displays the values of the curvature threshold. The yellow and the red lines are the lines in Figure 4.14: They represent the case where only one of the thresholds is used.

Some areas occur where the dots (representing combinations of thresholds) are above the solid lines. For the study cases that means that a combination of two thresholds outperforms usage of a single threshold there.

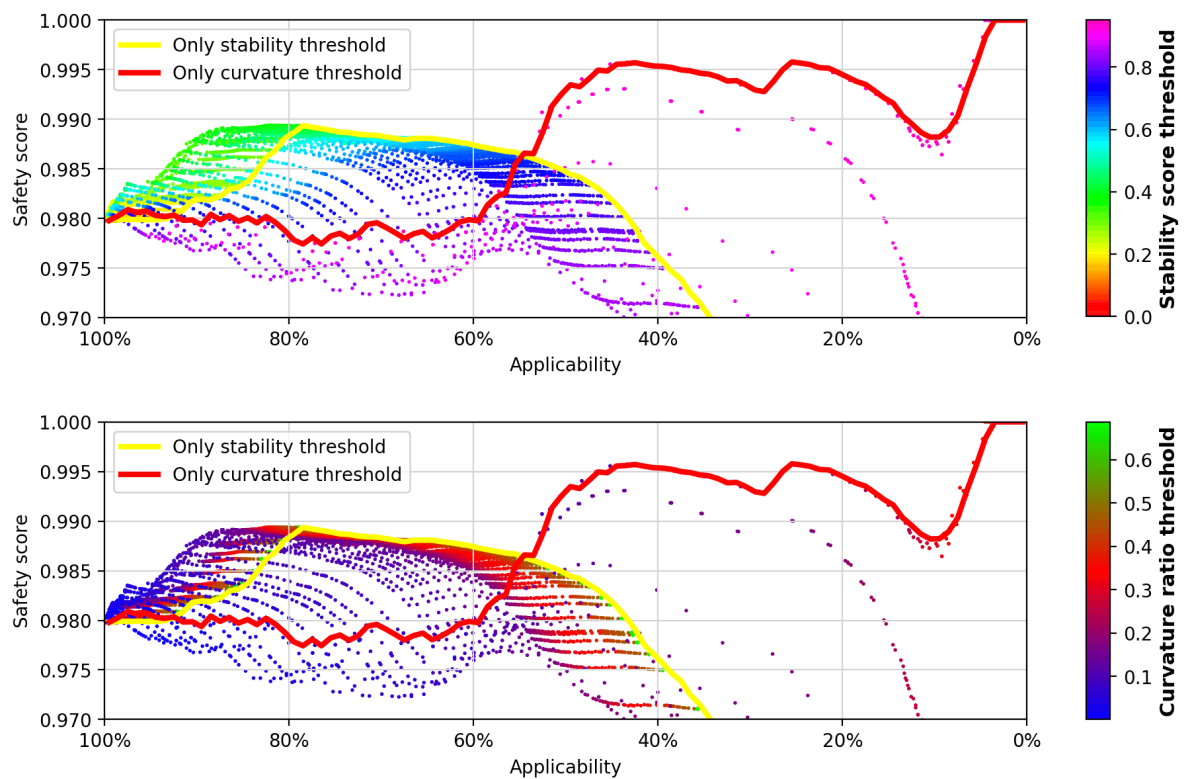


Figure C.9: This figure shows the effect that 10,000 different combinations of thresholds have on the safety score and the applicability for all study cases combined. The solid lines show usage of only a single threshold.

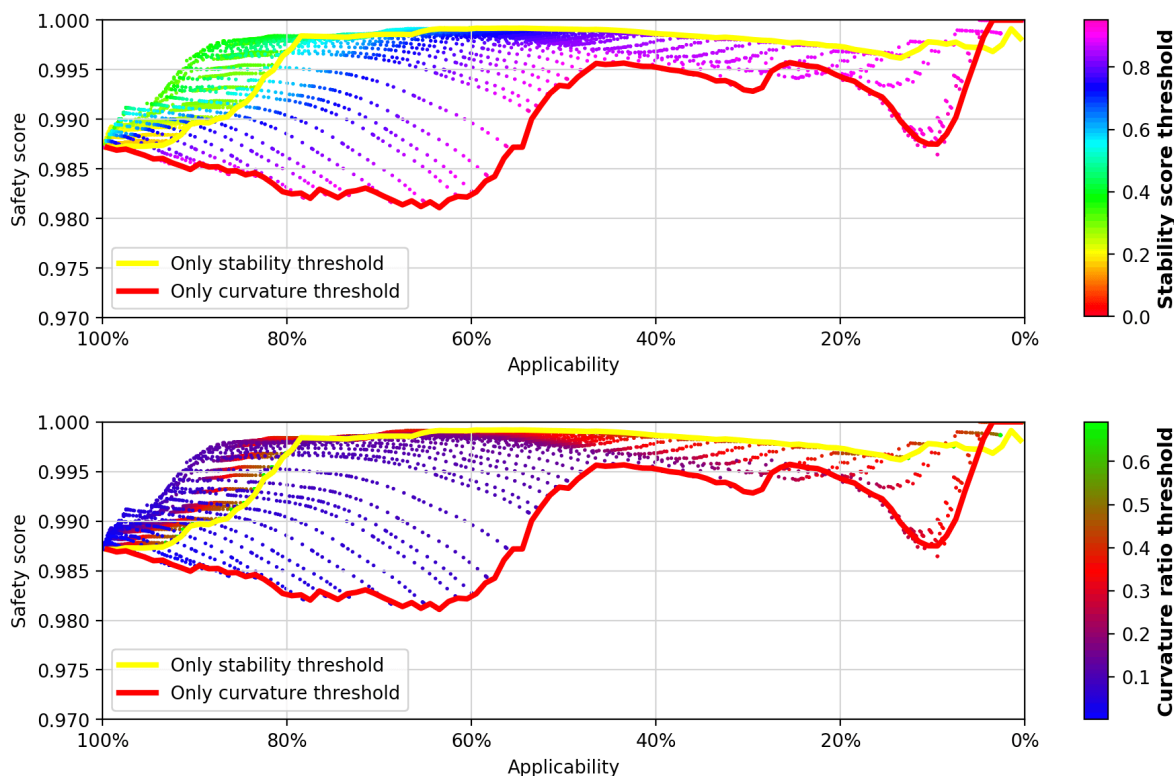


Figure C.10: This figure shows the effect that 10,000 different combinations of thresholds have on the safety score and the applicability for all study cases combined. The solid lines show usage of only a single threshold. **These are the results when one area with scour is remove from the data**

C.4. Sensitivity analysis

This section investigates how the performance of the axi-symmetric model is influenced by the decision for the highly uncertain calibration coefficient for the influence of helical flow a .

In Table C.1 the performance indicators for the axi-symmetric solution are displayed for varying calibration coefficients a . The calibration coefficient a determines partly the transverse slope in the axi-symmetric model. With increasing values of a , the transverse slope becomes steeper. Hence with increasing values of a , the axi-symmetric model calculates a more conservative slope and the calculated channel coverage score and calculated width decrease.

The safety score is the fraction of the total navigable area estimate that is correct (see §3.8). In Table C.1 initially the safety score goes up with increasing values of a and then it stagnates. This suggests that raising a to really high values does not necessarily make the model more robust. The calibration coefficient however is only used to determine the inside slope around the CoVadem data. It is suggested that a higher calibration coefficient a *does* have a positive influence on the robustness of the axi-symmetric model for the inner slope.

Table C.1: Performance of the axi-symmetric model calculated for all study cases combined, for varying values of the calibration coefficient a

Axi-symmetric model		$a = 0$	$a = 3$	$a = 5$	$a = 7$
Safety score	[–]	0.963	0.976	0.981	0.981
Channel coverage score	[–]	0.326	0.304	0.287	0.273
Average channel width	[m]	118.07	102.81	96.25	87.42